First mTRD Performance Studies in the mCBM 2020 Campaign

Masterarbeit im Studiengang Physik

Axel Puntke

Erster Gutachter: Prof. Dr. Anton Andronic
Zweiter Gutachter: Prof. Dr. Christian Klein-Bösing

31.08.2021

Westfälische Wilhelms-Universität Münster

Contents

1 Introduction

In the upcoming Compressed Baryonic Matter (CBM) experiment at the Facility for Antiproton and Ion Research (FAIR) it is possible to create matter at such high baryonic densities which naturally exists only within very dense objects, i.e. neutron stars, in the depths of the universe. At such conditions, a state of matter called Quark Gluon Plasma (QGP) is suspected, which is baryonic matter at such high density and temperature that the confinement of quarks is lifted. Besides within neutron stars, which could contain QGP matter at comparatively low temperatures and high densities, there was also a QGP at high temperatures and comparatively low densities present in the first microsecond of the early universe after quarks and anti-quarks were formed. Similar conditions are reached again in these times at collisions with the well-known LHC accelerator in Geneva. The aim of FAIR and in particular the CBM experiment is, to in contrast investigate QCD matter at high net-baryon densities and lower temperatures at the freeze-out from the plasma phase, using a newly build accelerator – the SIS100 – which is able to collide heavy nuclei with a fixed target at very high rates. The beam will enable very high interaction rates at the target, orders of magnitude above existing experiments, which is necessary to investigate the hadronized products of the QGP with enough statistics and require a novel detector readout concept. Unlike other experiments, CBM does not apply an external trigger to record an event but records self-triggered. Incoming data are directly reconstructed and analyzed to perform online event selection, to identify relevant reactions from the raw data stream, which will exceed 1 TByte/s.
To develop and test different aspects of the novel readout concept, the FAIR Phase-0 program is conducted, of which the mCBM fixed-target experiment at the SIS18 accelerator is a part. It consists of representative versions of the different subdetectors the final experiment will be built of, among them the Transition Radiation Detector (TRD). The TRD and its readout electronics are developed by groups located in Frankfurt, Münster, Bucharest and Heidelberg and its main task is to separate electrons from pions at high momenta by measuring their transition radiation as well as supporting the tracking of charged particles within CBM. Another important contribution is the identification of heavy fragments in hypernuclei measurements. This thesis is about first performance studies of the 2020 mTRD setup, the TRD representation in the mCBM experiment. For reference, the Time Of Flight subsystem mTOF is used, which reconstruction framework is already able to provide tracks of particles which are registered in the mTOF. Temporal and spatial correlations with the TOF hits and tracks are done to verify the functionality of the mTRD. During the analysis it was found that the TRD raw data is time-shifted against the mTOF reference detector and the shift is not constant, but varies over time, while still following specific patterns. Therefore, a correction routine had to be developed, implemented and applied first to enable further data analysis. The steps to analyze the data are described in this thesis and the results are presented and discussed. A matching algorithm for TOF tracks with TRD hits is developed and the effect of its configuration parameters

is analyzed. The matched tracks are used to determine the spatial distribution of the coincidence level of mTOF and mTRD and to finally investigate the rate-dependence of the coincidence level within single accelerator spills. Last, features of the readout electronics are checked.

2 Theoretical and Experimental Background

For developing, operating or merely understanding a particle detector it is essential to have theoretical knowledge on the interaction of particles with matter, in particular on the specific energy deposition processes in the detector, enabling it to register the traversing particles. This chapter will describe the relevant processes in gaseous detectors, and spotlight transition radiation detectors.

2.1 Interaction of Photons with Matter

2.1.1 Absorption of Photons

When photons traverse a material, they do not loose their energy continuously, but rather interact with the atoms in single processes. The mean distance of a photon traveling through a material without interaction is called the mean free path λ, which is the inverse of the material- and energy-dependent absorption coefficient μ_γ:

$$\mu_\gamma = \frac{1}{\lambda} = n\sigma \tag{2.1}$$

The absorption coefficient can also be expressed as the product of the particle density n in the material and the photon energy- and material-specific cross section σ. Furthermore it is a measure for the probability for a photon to get absorbed within the distance dx in a material. That means for N_γ incoming photons there will be in average a number of

$$dN_\gamma = -\mu_\gamma N_\gamma dx \tag{2.2}$$

photons which get absorbed per distance dx. Integrating this relation leads to an exponential decrease of photons when traversing a material:

$$N_\gamma(x) = N_{\gamma,0} \cdot e^{-\mu_\gamma x} \tag{2.3}$$

2.1.2 Absorption Processes and Their Energy Range

When a photon interacts with matter it can be absorbed by different physical processes. These processes each obey energy-dependent cross sections, while all summing up to the total cross section σ_{tot}. An overview on this behavior for carbon and lead is given in Figure 2.1. The three main processes for photon absorption are:

1. **Photoelectric Effect**
   By the photoelectric effect a photon with energy $E_\gamma > E_B$ can be fully absorbed by an atom by transferring its whole energy to a shell electron with binding energy E_B and thereby ejecting

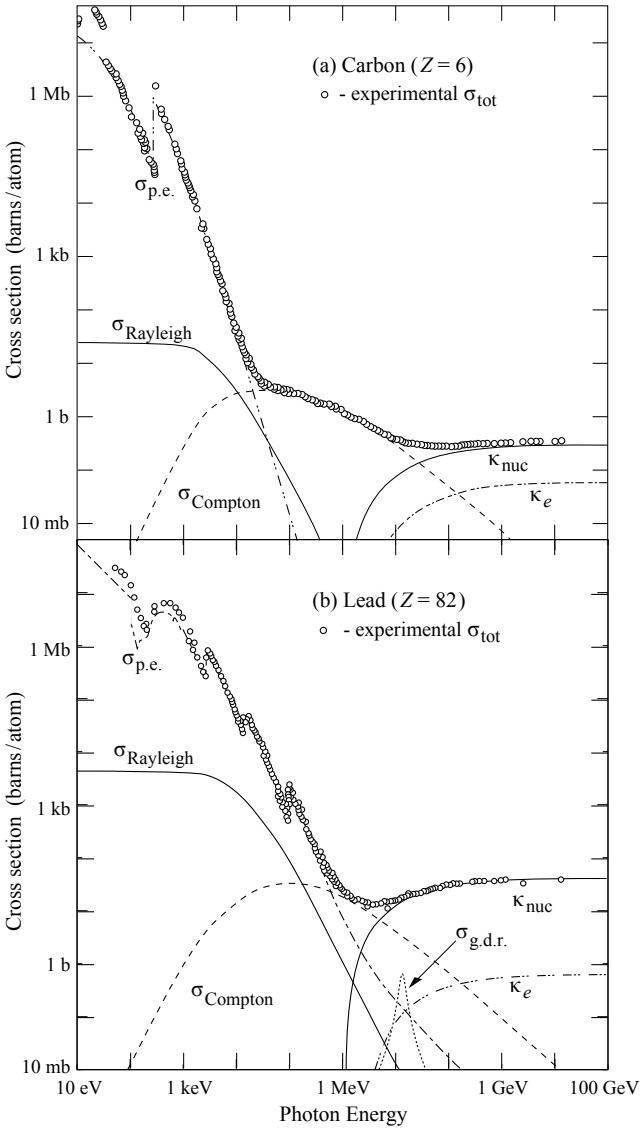

Figure 2.1: Photon total cross sections for (a) carbon and (b) lead, showing the contributions of the photoelectric effect $\sigma_{\text{p.e.}}$, Rayleigh scattering σ_{Rayleigh}, the Compton effect σ_{Compton}, pair production in nuclear field κ_{nuc} and electron field κ_{e}, and for lead also the contribution of photonuclear interactions $\sigma_{\text{g.d.r.}}$ (most notably the Giant Dipole Resonance). [PDG18]

it out of the atom:

$$\gamma + \text{Atom} \rightarrow (\text{Atom})^{+} + e^{-} \tag{2.4}$$

The ionized electron is found to carry the excess energy as kinetic energy. Because of the huge mass of the nucleus in comparison to the electron, the kinetic recoil energy which the nucleus gains is typically be neglected. Due to the higher density of electrons in the inner shells a photon has a higher probability to interact with them, while also the required energy is larger due to the larger electron binding in the inner shells. This leads to absorption edges for different shells, for example in Figure 2.1 there is visible the K-edge for lead and for carbon the M-, L- and K-shell (from low to high energy) can be seen.

2. **Compton Effect**
   The Compton effect describes the scattering of a photon with a free or lightly bound ($E_\gamma \gg E_B$) electron. This enlarges the wavelength of the photon and decreases its energy to [KW16]

$$E'_\gamma = \frac{E_\gamma}{1 + \frac{E_\gamma}{m_e c^2}(1 - \cos\theta_\gamma)} \tag{2.5}$$

   where m_e is the electron mass, c is the speed of light and θ_γ is the angle between the initial and the scattered photon direction. The electron gets the remaining energy $T = E_\gamma - E'_\gamma$ as kinetic energy and can be measured by a detector.

3. **Pair Production**
   A photon with at least the energy $E_\gamma \gtrsim 2m_e$ is able to convert into an electron-positron pair in presence of a Coulomb field, which is needed to conserve the momentum of all involved particles by transferring a recoil to another particle. This particle is mainly the atomic nucleus except for very light elements. For them it is also possible that the electrons provide the electric field, but for this process a much higher threshold energy is required, because the momentum transfer to the electrons is not negligible anymore as it is the case for the much heavier nucleus [KW16].

The cross sections of these three processes are a function of the photon energy and also depend on the atomic number of the material. While the photoelectric effect is most likely at lower energies in the order of electron binding energies and high atomic numbers Z, the Compton effect is the preferred process for materials with lower Z and intermediate photon energies. For high photon energies pair production is the dominant process.
For non-ionizing photon energies there are also other possible processes like e. g. Rayleigh scattering, but as these are elastic processes they do not deposit energy in a detector and are therefore not discussed here.

2.2 Interaction of Charged Particles with Matter

Unlike photons, charged particles deposit their energy continuously and not in a single process when traveling throughout a material. Here again different processes need to be respected for different particle energies and masses.

2.2.1 Heavy Charged Particles

For heavy charged particles like protons and nuclei with a mass $M \gg m_e$ the average energy loss $\left\langle -\frac{dE}{dx} \right\rangle$ per path length — which is also called the mass stopping power — for intermediate energies is described by the quantum-mechanical and relativistic Bethe-Bloch equation [KW16]:

$$\left\langle -\frac{dE}{dx} \right\rangle = K\frac{Z}{A}\rho\frac{z^2}{\beta^2}\left[\frac{1}{2}\ln\frac{2m_e c^2\beta^2\gamma^2 T_{\max}}{I^2} - \beta^2 - \frac{\delta(\beta\gamma)}{2} - \frac{C(\beta\gamma, I)}{Z}\right] \tag{2.6}$$

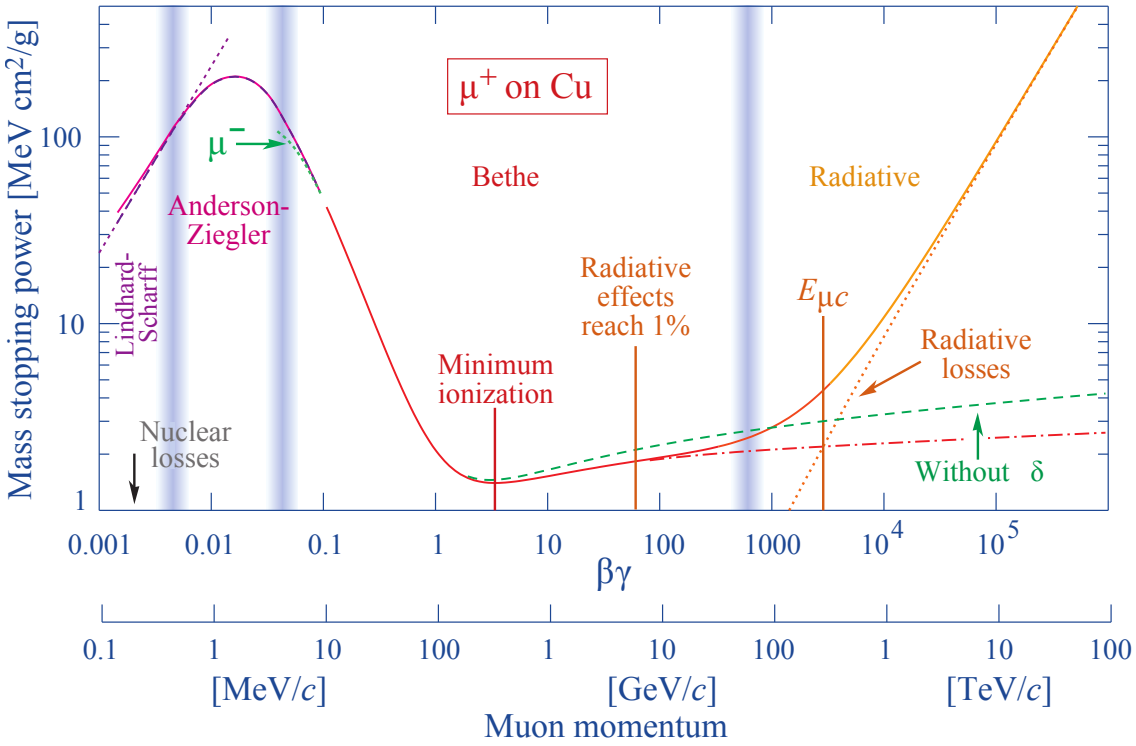

Figure 2.2: Mass stopping power for an anti-muon in copper. Solid curves indicate the total stopping power and vertical bands indicate boundaries between different approximations discussed in the text [PDG18]. In red, the results of the Bethe-Bloch equation are plotted.

where

K : material-independend coefficient $4\pi N_A r_e^2 m_e c^2 = 0.307\,\mathrm{MeV cm^2/mol}$

ρ : density of absorber

z : charge number of incident particle

Z : atomic number of absorber

A : atomic mass of absorber

β : ratio of particle velocity v to the speed of light c

γ : Lorentz factor

T_{max} : maximum energy transfer in a single collision

I : mean excitation energy

δ : density correction function for high energies

C : shell correction function for low energies

The maximum energy transfer T_{max} takes place when the incident particle centrally hits on an electron. According to relativistic kinematics this energy transfer is given by [KW16]

$$T_{\mathrm{max}} = \frac{2m_e c^2 \beta^2 \gamma^2}{1 + 2\gamma m_e/M + (m_e/M)^2} \overset{M \gg 2\gamma m_e}{=} 2m_e c^2 \beta^2 \gamma^2. \tag{2.7}$$

The approximation $M \gg 2\gamma m_e$, valid for low γ factors, shows that for intermediate energies the energy loss depends only on the velocity β of the incident particle and not on its mass.
The mean excitation energy is a material property and should be calculated out of measured data for best results, but as an approximation one can take [KW16]

$$I \approx 17.7\ Z^{0.85}\ \text{eV}. \tag{2.8}$$

The shell correction $C(\beta\gamma, I)$ is a correction term which is necessary for low particle energies for which the velocity approaches the orbital velocities of the outer atomic shells. In the calculation of the Bethe-Bloch equation the other charges are assumed as stationary which does not hold in this speed regime anymore. In the upper limit of the formula, Fermis density correction $\delta(\beta\gamma)$ is necessary to account for the effect that fast particles are able to polarize the traversed medium along their paths. This corresponds to a smaller energy loss, as the polarized atoms shield the electric field of the incident particle and reduce the interaction with charges more far away from the incident particles path.
Im Figure 2.2 the mass stopping power against $\beta\gamma$ is plotted for an anti-muon traveling through copper. The red curve shows the results of the Bethe-Bloch equation (excluding the shell corrections). For lower energies, where the formula is not satisfying anymore, the phenomenological approach of Anderson and Ziegler is shown, or for very low energies, the Lindhard-Scharff-Schiøtt Theory, respectively. At higher energies radiative losses rise to multiple orders above the losses by ionization and need to be added to the calculation. According to quantum electrodynamics, particles with energy E and mass m which experience an acceleration emit Bremsstrahlung with a radiation power E^2/m. This leads to the conclusion that for energies below 100 GeV/c Bremsstrahlung is of significance only for electrons and positrons [KW16]. As the top proton energy of the SIS100 accelerator which delivers the beam to the CBM experiment is 29 GeV per proton (or 15 AGeV for nuclei with $Z/A = 0.5$) [Sen20], Bremsstrahlung for heavy particles can be neglected here.

2.2.2 Light Particles

Light particles, which are positrons and electrons, easily gain energies which bring them into the relativistic regime ($E \gg mc^2$), resulting in significant energy losses by Bremsstrahlung. But also the loss by ionization needs to be considered for low energies (below few tens of MeV [Leo87]), as it is the case for heavy charged particles.

Energy Loss by Bremsstrahlung

To calculate the energy loss of a charged particle by Bremsstrahlung, the material-dependent radiation length X_0 is used. This parameter reflects the length a charged particle with initial energy E_0 needs to travel through a material until is has left only the energy E_0/e, meaning it radiated $1 - 1/e \approx 63\%$ of E_0 [KW16]. Using this parameter, the energy loss by Bremsstrahlung is

$$\left\langle -\frac{dE}{dx} \right\rangle_{\text{brems}} = \frac{E}{X_0}. \tag{2.9}$$

Energy Loss by Ionization

Below the critical energy E_c the energy losses due to ionization are dominant. An approximation of the critical energy, at which energy losses of Bremsstrahlung and ionization are at the same level, is given by Bethe and Heitler [Leo87]:

$$E_c \approx \frac{1600 m_e c^2}{Z} \tag{2.10}$$

To describe the energy loss by ionization, the Bethe-Bloch equation needs to be modified such that the deflection of the light particles are taken into account. In the special case of electrons, their indistinguishability from the shell electrons of the medium implies further modifications. Also the maximum energy transfer in a single collision changes to

$$T_{\max} = \frac{E_{\text{kin}}}{2}, \tag{2.11}$$

where E_{kin} is the kinetic energy of the incident particle. The mass stopping power finally becomes [Leo87]:

$$\left\langle -\frac{dE}{dx} \right\rangle = \frac{K}{2}\rho\frac{Z}{A}\frac{1}{\beta^2}\left[\ln\frac{\tau^2(\tau+2)}{2(I/m_e c^2)^2} + F(\tau) - \delta(\beta\gamma) - \frac{2C(\beta\gamma, I)}{Z}\right] \tag{2.12}$$

with $\tau = \frac{E_{\text{kin}}}{2}\frac{1}{m_e c^2}$ and

$$F(\tau) = \begin{cases} 1 - \beta^2 + \frac{\frac{\tau^2}{8} - (2r+1)\ln 2}{(\tau+1)^2}, & \text{for } e^- \\ 2\ln 2 - \frac{\beta^2}{12}\left(23 + \frac{14}{\tau+2} + \frac{10}{(\tau+2)^2} + \frac{4}{(\tau+2)^3}\right), & \text{for } e^+ \end{cases}$$

In Figure 2.3 the fractional energy loss per radiation length for different processes is shown. For low energies ionization is the dominant process, while for larger energies the energy loss by Bremsstrahlung outranges all other processes.

Other Processes

Additional energy losses for positrons and electrons are related to further processes. Large energy transfers to the shell electrons by incident electrons can be described by the Møller scattering, and for positrons the Bhabha scattering is possible respectively [PDG18]. Their contribution to the total energy loss is also plotted in Figure 2.3. Another possible process for incident positrons is the annihilation with the electrons of the medium. This particularly contributes to the energy loss at lower energies as can be seen in Figure 2.3.

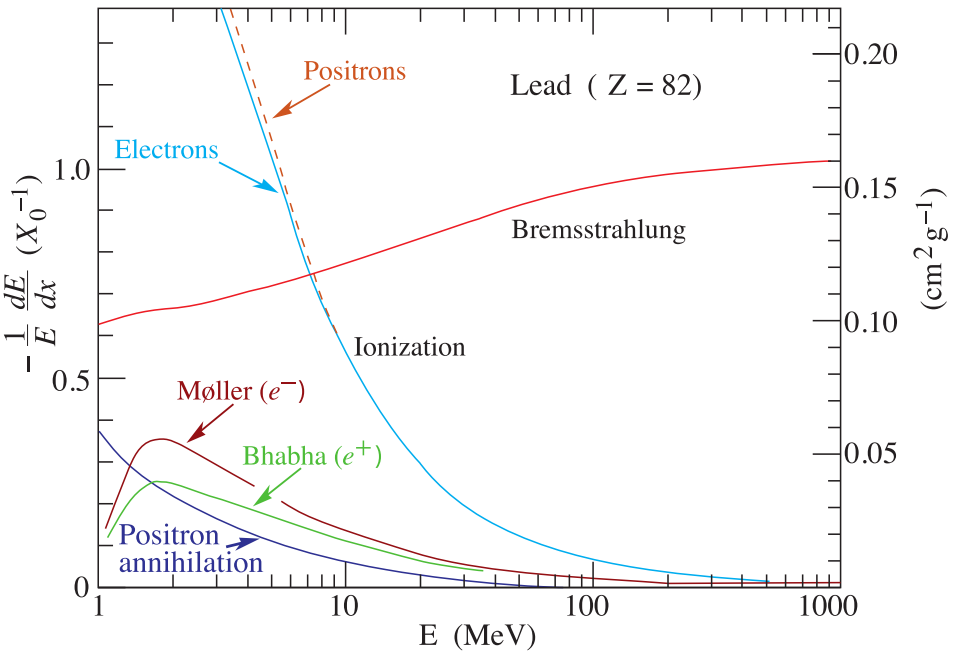

Figure 2.3: Fractional energy loss per radiation length in lead as a function of electron or positron energy. Electron (positron) scattering is considered as ionization when the energy loss per collision is below 0.255 MeV, and as Møller (Bhabha) scattering when it is above. [PDG18]

2.3 Transition Radiation

Another way for charged particles to deposit energy in the detector is the production of transition radiation. Transition radiation is produced by these particles each time they cross a boundary between two media with different dielectric constants ϵ_i. The different dielectric properties of the media force the electric field of the particle to change while crossing the border, as the Maxwell equations require the field to be continuous there. This leads to the emission of transition radiation (TR) photons. For highly relativistic particles ($\gamma \gtrapprox 1000$) [AW11] the energy of the emitted TR photons reaches the X-ray domain (range of keV). This attribute makes TR interesting for detection of highly relativistic particles where Cherenkov detectors get unattractive, because the variation of the Cherenkov angle $\Delta\theta_C$ is small in this γ domain [KW16]. Transition radiation in contrast is radiated symmetrically in a cone around the trajectory of the particle with $\theta_{\mathrm{mpv}} \approx 1/\gamma$ as the most probable value for the angle between the particle and the TR photon [KW16]. The distribution of energy W per solid angle $d\Omega$ and frequency slice $d\omega$ for a fixed emission angle $\theta \ll 1$ is given by [KW16]

$$\frac{d^2W}{d\Omega d\omega} \approx z^2 \frac{\hbar\alpha}{\pi}\theta^2 \left(\frac{1}{\gamma^{-2} + \xi_{p1}^2 + \theta^2} - \frac{1}{\gamma^{-2} + \xi_{p2}^2 + \theta^2} \right)^2 \tag{2.13}$$

for $\gamma \gg 1$ and $\omega \gg \omega_{p2} \gg \omega_{p1}$ with $\xi_{pi} = \omega_{pi}/\omega \ll 1$, z being the atomic charge, α being the fine-structure constant and w_{pi} being the electron plasma-frequency of the medium i. Integrating

Equation 2.13 over Ω and $\hbar\omega$ yields the total radiated energy for a single transition [KW16]:

$$W = z^2 \frac{\hbar\alpha}{3}\gamma \frac{(\omega_{p2} - \omega_{p1})^2}{\omega_{p2} + \omega_{p2}} \overset{\omega_{p2} \gg \omega_{p1}}{\approx} \frac{z^2\alpha}{3}\gamma\hbar\omega_{p2} \tag{2.14}$$

Therefore the radiated energy is proportional to γ and ω_{p2}, the plasma frequency of the medium with the higher plasma frequency. The number of emitted photons per transition is in the order of $\alpha = \frac{1}{137}$ [KW16], so it is necessary to have a few hundred transitions between media within a detector to produce a significant amount of TR photons. In modern detectors this high amount of interfaces is realized with foil stacks (regular radiators) or foam and fiber elements (irregular radiators). The distance between these interfaces cannot be arbitrarily short for TR production, because a minimum travel distance Z_i for the incident particles electric field is needed to readjust itself and separate from the TR photon field. This distance is called the formation zone and is given by [AW11]

$$Z_i = \frac{1}{\gamma^{-2} + \xi_i^2}\frac{2\beta c}{\omega}. \tag{2.15}$$

It depends on the incident particles γ factor as well as energy $\hbar\omega$, and typical values of Z_i are in the range of a few 10 to a few 100 µm ($Z_{\text{Polyethylene}} \approx 7\,\mu\text{m}$, $Z_{\text{Air}} \approx 700\,\mu\text{m}$ [KW16]).

3 Experimental Setup

This chapter gives an overview of the structure, the goals and the functionality of the CBM experiment and the associated particle detector. In addition, the mCBM experiment is described, which is carried out to test the prototypes of the individual subdetectors, to demonstrate the cooperation of all subsystems and to perform readout tests with the combined data acquisition chain. Special attention is paid to the TRD working principle and readout concept as well as the TRD setup used in mCBM 2020.

3.1 The CBM Experiment

The Compressed Baryonic Matter (CBM) experiment will be located at the Facility for Antiproton and Ion Research (FAIR) in Darmstadt and is one of the main experiments planned to operate at the SIS100 particle accelerator. Both, the accelerator and the experiment, are currently under construction. Its goal is to explore the QCD phase diagram at very high net baryon densities, a region, where still remain as well theoretically as experimentally many open questions. A conjectured sketch of the phase diagram is shown in Figure 3.1, but quantitative investigation and determination of the transitions between the phases has not been archived yet. Similar to phase diagrams used in thermodynamics (e.g. for water), where usually pressure is plotted against temperature and transitions between phases are sketched in, the same is done in Figure 3.1 for strongly interacting matter. Here, instead of pressure, the baryon chemical potential μ_B is used, a quantity which is a measure for the net baryon density ρ (number of baryons minus number of antibaryons per volume) [ESS05], as the pressure is not an independent parameter, but a function of T and μ [Fri+11]. Nonetheless an increase of μ_B corresponds to an increased pressure [Fri+11]. The vacuum state ($\mu_B = T = 0$) is located in the lower left corner. Ordinary nuclear matter still has on these scales almost negligible temperature and lives near the μ_B-axis at baryon chemical potential in the order of the nucleon mass (≈ 1 GeV) [Bay+18]. Following the μ_B-axis further at low T values to higher μ_B values, which is equivalent to increasing the pressure [Fri+11], leads to matter of densities equal to matter inside neutron stars and for even higher μ_B to a color superconducting phase, which also may naturally occur within neutron stars.

For moderate temperatures and densities, a mixture of baryons, anti-baryons and mesons called hadron gas is expected. The quarks and gluons are still confined here, while for even higher temperatures they are assumed to move freely in a so-called Quark Gluon Plasma (QGP). For vanishing baryon chemical potential and therefore an equal amount of particles and antiparticles like in the early universe, calculations on the lattice predict this transition into a QGP to happen at a temperature of $T \approx 160$ MeV [Ca16].

At moderate temperatures and densities (hadron gas phase), strong interacting particles do not

exhibit chiral symmetry, which means that their QCD Lagrangian is not invariant under vector and under axial-vector isospin transformations, caused by the non-vanishing quark masses and their corresponding mass terms (see [Koc97] for details). The symmetry is spontaneously broken in the vacuum state, leading to the observed very small pion mass compared to other hadrons [Koc97]. But in the QGP, phase theory predicts that chiral symmetry is restored and as a consequence the pions become as massive as all other hadrons (if confinement still allows them to exist at these high temperatures/densities) [Koc97], resulting in a new phase with different physical properties. In the phase diagram, the QGP and hadron gas regions must be separated by a closed boundary, which is of first order according to theory [Fri+11]. This border line ends in the critical point, which is of second order according to theory. Beyond this point, the QGP and hadron gas phases are no longer distinguishable [Fri+11].
For the CBM experiment the focus is on the search for the theoretically predicted phase transition between hadronic and partonic matter — the Quark Gluon Plasma — and the critical endpoint, which are expected to be found at finite baryon chemical potential and moderate temperatures, as well as the chiral phase transition [Fri+11]. Further objectives are to find the thermodynamic equation-of-state of baryonic matter at neutron star densities, to deeper understand the mechanism of chiral symmetry breaking by studying the properties of hadrons in dense matter and to observe exotic forms of QCD matter [Ca16].

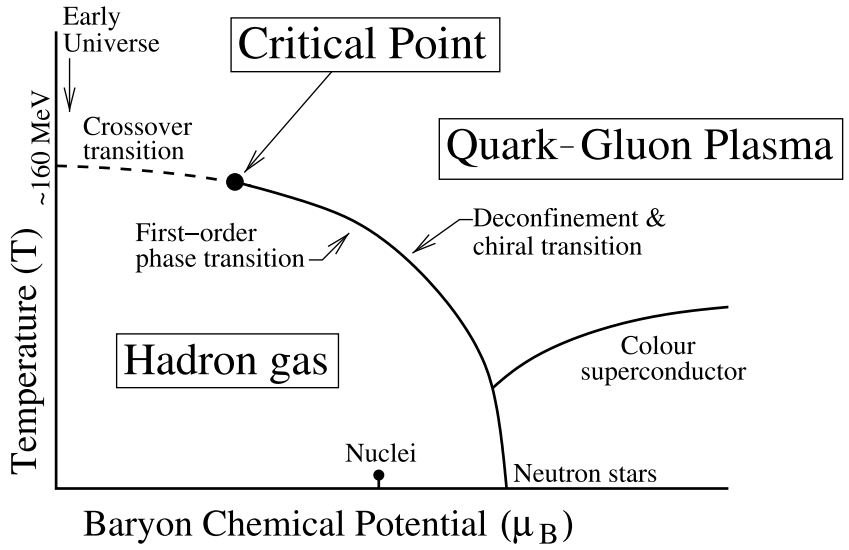

Figure 3.1: Sketch of the QCD phase diagram which is to be explored. [KM14]

3.1.1 Facility for Antiproton and Ion Research (FAIR)

While other well known accelerators as RHIC and LHC and their affiliated experiments explore the phase diagram towards higher temperatures and almost zero net-baryon densities, the CBM experiment is foreseen to expand the exploration into the regions with higher baryon chemical potential at moderate temperatures [SS11]. To produce matter at such high densities, which freeze-out products or its decay products, respectively, can be observed by a detector later on, the new

particle accelerator SIS100 at the Facility for Antiproton and Ion Research (FAIR) was planned and is currently under construction. A sketch of the planned accelerator complex is shown in Figure 3.2. The already existing SIS18 accelerator will serve as an injector for the SIS100, which will have a magnetic rigidity of 100 Tm and a circumference of 1100 m [Gut+06]. It will be able to accelerate protons, antiprotons and nuclei of all kinds up to uranium [SS11]. For protons, the SIS100 will reach a beam energy of up to 29 GeV [Gut+06] and for heavy nuclei the maximum beam energy is also in the range of a few GeV (e.g. 11 AGeV for Au [TDR18]). The interaction rates at the target are very high, e.g. the beam extracted to the CBM cave will reach up to 10^9 Au ions per second [TDR18]. Besides providing a very intense beam for the CBM experiment, the facility also supplys other experiments using a complex system of storage-cooler rings and experimental stations [Gut+06].

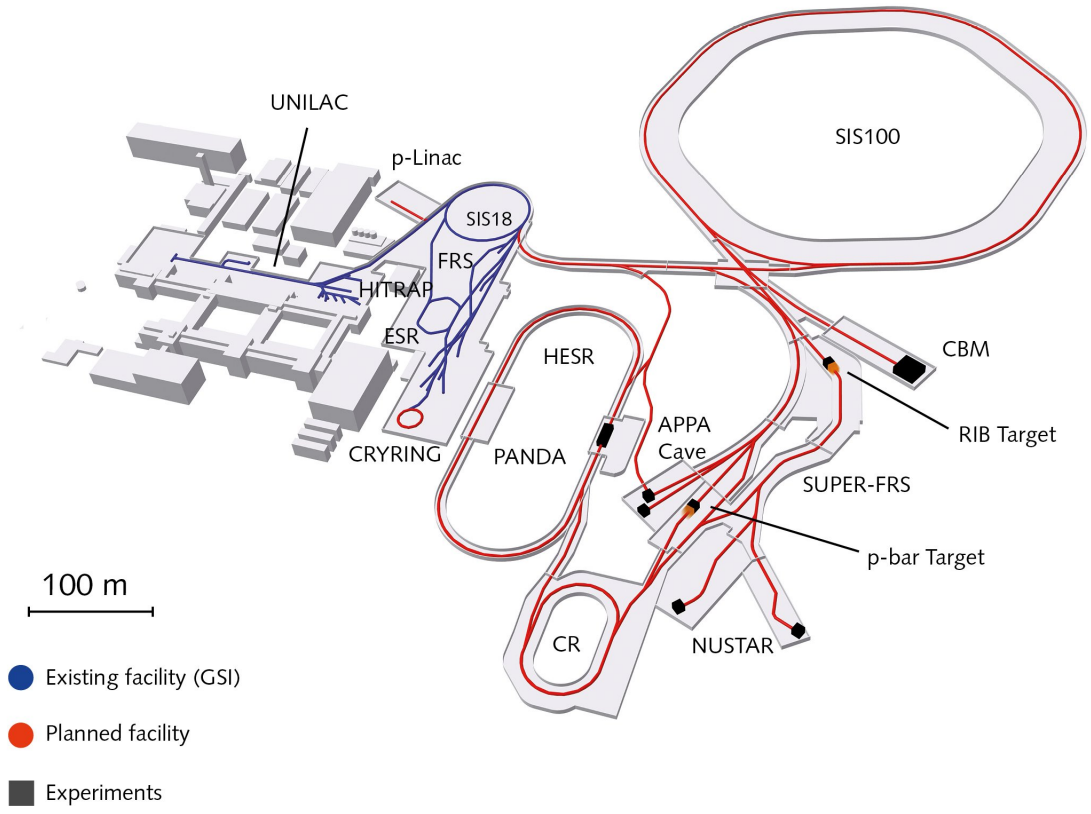

Figure 3.2: Sketch of the planned FAIR facility with the superconducting SIS100 synchrotron accelerator and its affiliated experiments. Also visible are the high energy antiproton storage ring (HESR) and the collector ring (CR). [FAI17]

3.1.2 CBM Detector

To achieve the high densities needed to explore the QCD phase diagram, heavy ions get accelerated with the SIS100 and subsequently collided with a fixed target in front of the CBM detector. At

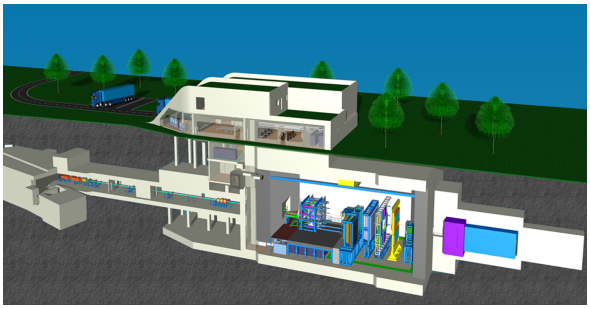

(a) Sectional view of the CBM experiment building [Cbm]

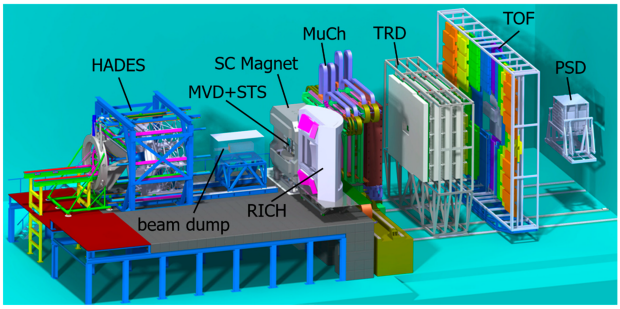

(b) Different subsystems of the CBM detector (HADES is another experiment) [Sen20]

Figure 3.3: Overview of the planned CBM experiment. The detector is located in an underground hall with a massive beam dump at the end. There are also underground rooms for beam diagnostics, gas preparation, high voltage and cooling supply. Overground are rooms for gas storage and computing as well as user and service areas. The experiment hall has a height of 17 m.

FAIR energies these collisions can produce a fireball of matter at neutron star densities for a short time span of about 5-10 fm/c [Sen20], which then produces up to 1000 new particles per collision in its hadronization process [Col13]. This high multiplicity combined with the high interaction rate of up to 10 MHz the CBM experiment aims at requires a novel readout and data processing scheme that can handle those high rates of particles emerging from the fireball. Therefore the CBM detector was designed to identify hadrons, electrons and muons in Au+Au collisions at beam energies from 2 to 11 AGeV at reaction rates up to 10 MHz [Sen20].
The CBM detector will be located in an underground cave with a direct connection to the SIS100. The detector hall and the corresponding infrastructure rooms are sketched in Figure 3.3a. The detector itself is sketched in Figure 3.3b and consists of 7 subsystems, whose main tasks are listed below. The fragments of the collision first pass the superconducting dipole magnet with a large aperture of $\pm 25°$ polar angle and a magnetic field integral of 1 Tm [TDR18]. Inside the magnet, the Micro Vertex Detector (MVD) and Silicon Tracking System (STS) are located. The MVD is a specialized detector within the open charm and hyperon program of the CBM (otherwise not in place) and identifies the decay vertices of particles with very short lifetimes such as charmed mesons. STS with its 1.8 million channels [Sen20] is foreseen to determine the trajectories and momenta of charged particles with very high precision in the general CBM setup. Next either the Ring-Imaging CHerenkov (RICH) detector or the Muon Chamber (MUCH) is placed into the measurement area, depending on the current detector setup. MUCHs main task is to filter out muons by absorbing other types of particles using a hadron absorber which is sliced by multiple gas detectors. The segmentation allows MUCH to track the muons and measure also muons of low momenta which would have been otherwise stopped by a single thick absorber[Col14]. It shares its place with the RICH detector, which can be exchanged with it and is responsible for identifying electrons and positrons via the measurement of their Cherenkov radiation at lower to intermediate momenta. For higher momenta this task is fulfilled by the Transition Radiation Detector (TRD), which also supports the tracking of the particles. After the TRD, the Time Of Flight (TOF) detector with an overall time resolution

of 80 ps is located, which identifies particles by their time of flight using Multi-Gap Resistive Plate Chambers (MRPCs). The last detector is the Projectile Spectator Detector (PSD), a segmented hadron calorimeter which is responsible for the event characterization. It measures the spectators and also particles close to beam rapidity to determine the centrality and reaction plane angle of the collision [Sen20].
As mentioned above, the high interaction rates required for measurement of particles with very small production crosssections of the CBM experiment require a novel readout concept to handle the huge amounts of generated data. In contrast to existing and under construction heavy ion experiments, which operate at rates up to 10 kHz at colliders and 50 kHz in fixed target mode [Sen20], the CBM detector has to measure at interaction rates up to 10 MHz. This requires a self-triggered readout concept for each subsystem and online event selection, implemented in software and hardware, to reject the background events which contain no signal by a factor of 100 or more in order to be able to store these events on disk [TDR18]. For this purpose, the CBM detector is directly connected to the GSI GreenIT cube, a computing farm with many-core CPU and GPU nodes which perform the online event reconstruction and selection.

3.1.3 Transition Radiation Detector

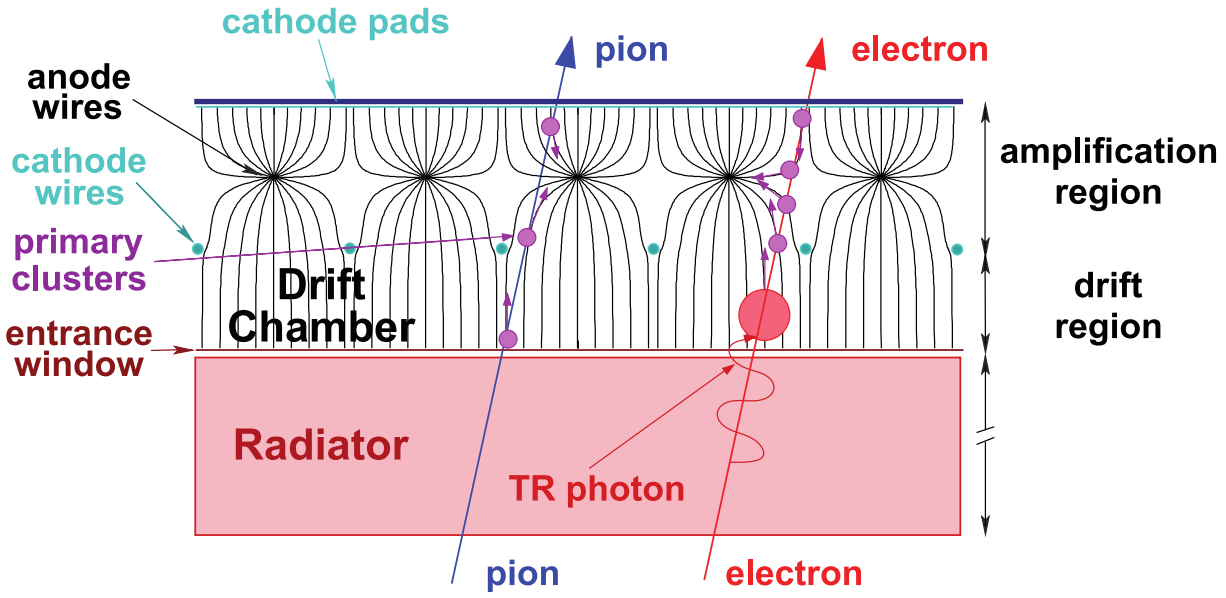

Figure 3.4: A schematic illustration of the working principle of the CBM-TRD [TDR18].

The main task of the TRD is to identify electrons at momenta $p > 1$ GeV/c with a pion suppression factor of $\frac{1}{\epsilon_\pi} = 20$ at an electron efficiency of $\epsilon_e = 90\%$ [TDR18]. The electron efficiency ϵ_e is defined as the fraction of electrons which were identified correctly while the pion efficiency ϵ_π is the fraction of pions which were misidentified as electrons. The pion suppresion factor $\frac{1}{\epsilon_\pi}$ is the inverse value of the pion efficiency [KB09].
Hadrons and pions in particular are produced in high amounts in nucleus-nucleus collisions and pions as the lightest hadrons are hard to distinguish from electrons [KB09]. The reason is that the other particle identifying detectors RICH and TOF are sensitive to the velocity v of the particle and

light particles very soon approach c, the speed of light, at moderate energies, making the velocity a bad measurand. However, using their different production yields of transition radiation is a way to separate them from each other nevertheless. The γ factor depends on the ratio of the kinetic energy E_{kin} of the particle to its rest mass E_0:

$$\gamma = \frac{1}{\sqrt{1 - \frac{v^2}{c^2}}} = \frac{E_{\text{kin}}}{E_0} + 1 \tag{3.1}$$

For the same given kinetic energy this leads to a lower γ for pions than for electrons, and therefore according to Equation 2.14 less production of TR photons. Actually, the TRD by its design, is producing close to no TR at all for pions [TDR18].
The TRD for the CBM detector will be build up of four layers which are composed of differently sized quadratically shaped modules. A module consists of two parts, a radiator and a read-out chamber. The working principle is illustrated in Figure 3.4. When a charged particle crosses the detector, it first passes the irregular radiator, where in the case of electrons, transition radiation is generated. The TR photons, whose energies are in the X-Ray region and are most likely emitted in a narrow cone arround the trajectory of the charged particle (see section 2.3), reach the read-out chamber, filled with a mixture of 85% Xenon and 15% CO_2. Xenon, although it is very expensive, is used as the main gas component in the counting gas because the maximum thickness of the whole detector is limited and Xenon has the shortest absorption length compared to other stable noble gases (Argon and Krypton) [TDR18]. For a typical TR photon with an energy below 10 keV the absorption length in Xenon is less than 10 mm [TDR18]. This leads to the absorption of the TR photons directly behind the entrance window of the read-out chamber, creating free electrons drifting along the homogenous electric field in the drift region. The field is generated by a positive voltage applied between the entrance window and the equally spaced cathode wires. The drift region ensures that most of the TR photons are absorbed and reduces the effect of bending of the entrance window by pressure changes to the electric field in the amplification region. After the drift region, the amplification region follows, where the anode wires each create a radial field due to the high positive voltage applied to them. When the electrons come near the anode wires, they gain enough energy to ionize the detector gas, leading to an avalanche effect and therefore a huge amount of electron-ion pairs. What is then finally measured is not the current which is induced into the anode wires, but the mirror charges which are induced by the ions drifting towards the cathode pads. These pads are then read out by the readout electronics.
Additionally to the electron-ion pairs created by the TR photons, a charged particle crossing the detector, whether its a pion or an electron, ionizes the detector gas along its path by the processes described in chapter 2, creating more electron-ion-pairs which can be measured by the detector. This gives the opportunity to support the particle identification by the measurement of the mass stopping power $\left\langle -\frac{dE}{dx} \right\rangle$ of the particle and also enables the detector to track particles which produce no TR.

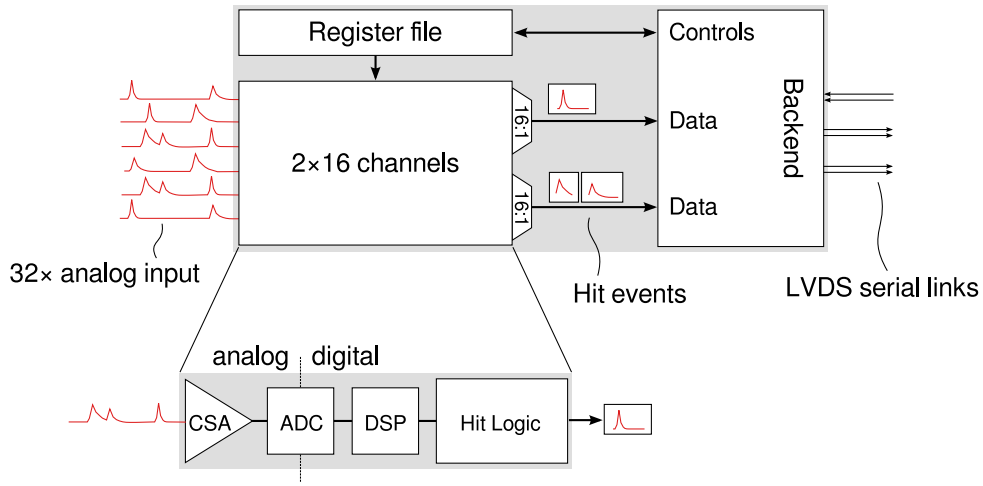

Figure 3.5: Conceptional block diagram of the SPADIC chip. [TDR18].

Readout Electronics

The backplate of the detector is segmented into rectangular cathode pads which are connected to the readout electronics. The readout is realised by a radiation-hard integrated circuit explicitly developed for the CBM-TRD, the SPADIC (Self-triggered Pulse Amplification and Digitization as IC) [Arm13], which is mounted on a Front-End Board (FEB). It has 32 analog input channels which are connected to the cathode pads of the TRD modules. The charge signals coming from the pads first pass the channels Charge Sensitive Amplifier (CSA), which converts the incoming current into a voltage pulse of the form

$$U(t) = A \cdot \frac{t}{\tau} \cdot \exp\left(-\frac{t}{\tau}\right) \tag{3.2}$$

using its preamplifier and subsequent shaper with a peaking time of $\tau = 120\,\text{ns}$. The amplitude A of this pulse is proportional to the total collected charge. The pulse is then digitized using an 9 bit Analog Digital Converter (ADC) running at 16 MHz, which corresponds to a length of 62.5 ns per sample. Upstream of the ADC, a Digital Signal Processor (DSP) is integrated in the chip, which is not described further here, as it is not used within the measurements covered in the course of this thesis. The CSA, ADC and DSP process data continously, but in the next step of the readout process the channels incoming data is filtered by the hit logic. The hit logic evaluates three consecutive samples and can be programmed by the user to trigger either when the samples overrun absolute or differential thresholds. When the trigger condition is fulfilled, the three trigger samples, the two previous samples and the next up to 27 samples (user-programmable) are used to build a so-called *hit message*. An additional feature of the SPADIC is to trigger the adjacent channels of a channel which fulfilled the trigger condition, called Forced Neighbor Readout (FNR), which is even possible beyond chip borders. This allows the usage of high thresholds for for full trigger efficiency even with moderate thresholds while simultaneously using the neighbor pads – which usually also see a charge – in the position reconstruction of the incident particle.
The hit messages produced by the SPADIC contain not only the up to 32 samples, but also additional metadata: The 4 bit channel id (0-15) within a half-SPADIC, the 8 bit timestamp, the 1 bit multihit

flag and the 2 bit hit type. The multihit flag is set to 1 when the trigger logic registered a new hit while the samples of the previous hit are still processed by the chip, leading to an abortion of the previous message. Since SPADIC 2.2, the user-programmable "retrigger-protection" defines a minimal hit message length, during which such a retrigger is suppressed. The choice of this protection time is done in the knowledge of the SPADIC pulse shape. The hit type indicates wether the hit was fully self-triggered, neighbor-triggered or both. For the timestamp, 8 bit is enough, because the SPADIC can in addition send other messages than hit messages including epoch messages which signalise a new temporal epoch for the timestamps of the hit messages. An epoch message is always sent when the 8 bit timestamp counter overflows. Other message types are mainly responsible for the reporting of errors and exceptions, e.g. buffer overflows.
Each channel has a First-In-First-Out (FIFO) buffer to store its messages, which is constantly merged with the other channels FIFOs to one time-ordered single data stream per 16 channel groups (half-SPADIC). The two uplink data streams per SPADIC are then transported out of the chip via two serial e-link interfaces using 8b10b-encoding to keep the cables potetial free. The maximum bandwith of each e-link is 320 Mbit/s. The data from both e-links is then send to the Readout Board (ROB), which multiplexes the data streams of up to 42 e-links using the CERN GBTx radiation-hard ASIC and outputs the data on a 4.8 Gbit/s optical-fibre GBT link. The data was then routed to a data processing board called AMC FMC Carrier Kintex (AFCK), which is equipped with a Xilinx Kintex-7 FPGA and preprocesses the data [Col17]. The messages of the SPADICs are packed into microslices, which are data containers of fixed time length (1280 µs in current setup), and it is also possible to use the high computing power of the FPGA for preprocessing the data, e.g. for clustering, filtering or other feature extraction. Another functionality of the AFCK is to send the circuit timing and configuration signals to the SPADICs in downstream direction, which are also routed through the ROBs. The preprocessed microslices generated by the AFCK are then sent upstream via a 10 Gbit/s optical link to the First Level Event Selector (FLES) computing nodes, located in the GreenIT cube in 700 m distance to the experiment. These nodes are equipped with PCIe FPGA boards, the FLES Interface Boards (FLIBs), which are able to input the custom optical data stream from multiple AFCKs to commercial of-the-shelf computing hardware. The FLES nodes combine the microclices from all input links to timeslices, which are larger data containers consisting of 10 consecutive microslices in the current setup and therefore cover a time period of 12.8 ms. The timeslices do not contain data from the TRD alone, but from all subsystems which are connected to the FLES node. Among other design updates (e.g. in the FPGA layer), the in total several hundred computing nodes of the future CBM experiment will be connected to each other to perform an online analysis of the timeslices and select the events which are eventually stored on hard drives. The total data rate the computing cluster has to process in the final experiment will exceed 1 TByte/s [HCL17]. The FLES computing cluster has to reduce this high amount of data by at least two orders of magnitude by reconstructing the raw data in real-time up to a stage where a decision by some physics trigger signature can be made to keep or discard it [Col17].

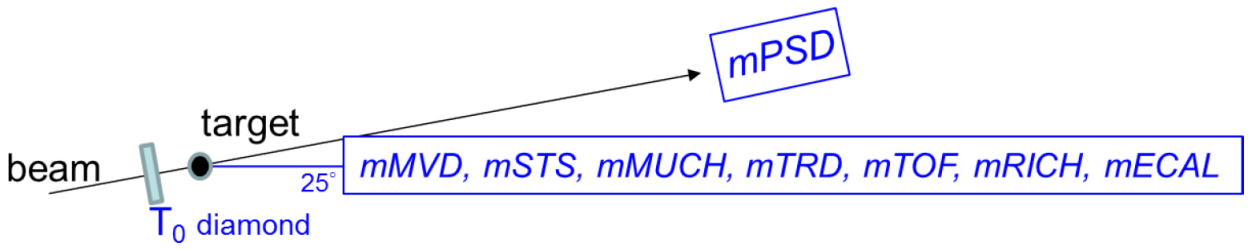

Figure 3.6: Concept sketch of the mCBM experiment located at the SIS18 accelerator. All detectors except mPSD are placed under a polar angle of 25° w. r. t. the primary beam. The total length of the setup is about 3 m. [Col17].

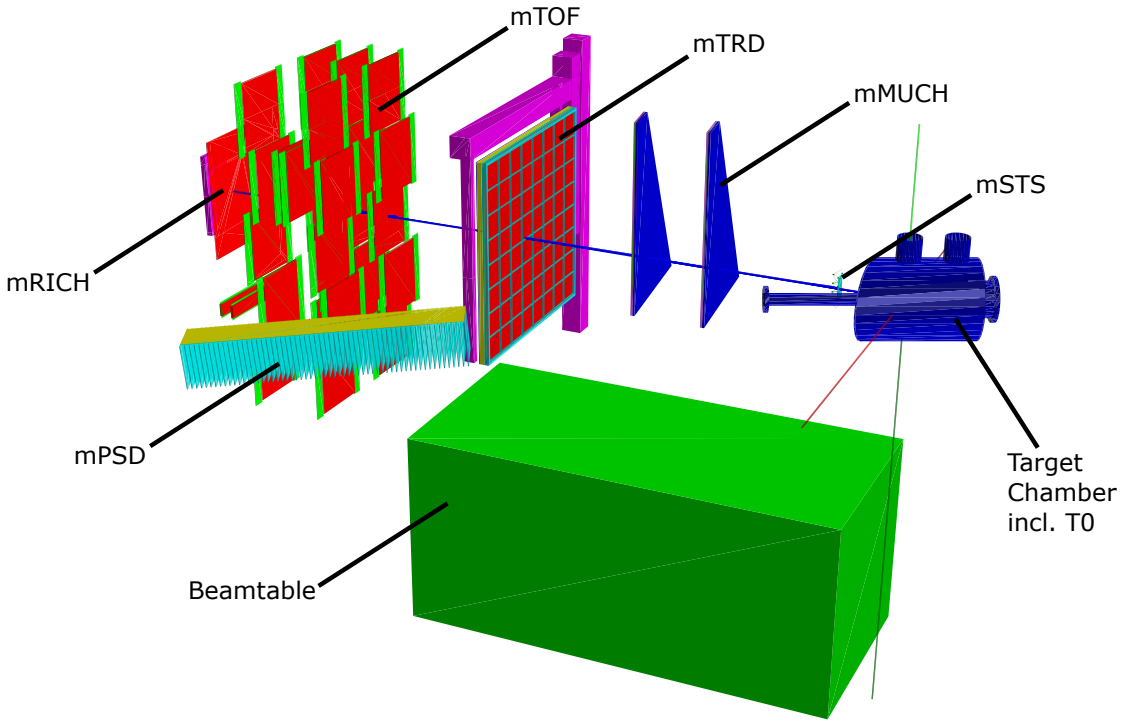

Figure 3.7: Annotated render of the geometry file (`mcbm_beam_2020_03.geo.root`) used in the hit reconstruction process for mCBM 2020.

3.2 The mCBM Experiment

The mCBM (mini-CBM) experiment is part of the FAIR Phase-0 program and is a full-system test setup for development of all CBM subdetectors. It is located at the existing SIS18 accelerator at the *GSI Helmholtzzentrum für Schwerionenforschung* and its primary goal is to test and optimize the complex interplay of all different subdetectors under realistic experiment conditions. Thus the whole CBM collaboration already works closely together and the commissioning time of the final CBM detector will be minimized. The main tasks are to test the free-streaming data aquisition chain described above from all subsystems to the GreenIT cube and the online track and event reconstruction and selection algorithms on the computing nodes. Also the detector control system can be tested here. By now, the main analysis of the collected data is performed offline. To come

close to realistic experiment conditions and to check the performance of the systems, the detectors are operated at comparatively high interaction rates in the final CBM regime [Col17], in order to gain knowledge of the full system behavior in a high-rate environment.
To demonstrate the capability of the detector to recognize signatures of rare observables online and select the corresponding data for storage when found, the Λ baryon production yield shall be measured. The Λ baryon is expected to have a very rare experimental production yield of 10^{-5} at SIS18 energies [Col17] and is therefore a good challenge to reconstruct. The yield can also be compared to existing published data, making the Λ reconstruction yield a good benchmark observable.
Like in the final CBM experiment, the beam is extracted out of the SIS18 accelerator and hits a fixed foil target in a vacuum chamber. A conceptual sketch of the setup can be seen in Figure 3.6 and Figure 3.7 shows a render of the geometry file used for mCBM 2020. All subdetectors used in mCBM also have the m-prefix. The spectator particles not participating in the collision are measured with a particle spectator detector, the mPSD. The other subsystems are placed under a polar angle of 25° with respect to the primary beam. The order does not match the final order of the CBM experiment. The setup also dispenses with a magnet in contrast to CBM. For the calibration and test phase of the mTOF detector, an additional T_0 detector with a resolution of 50 ps is installed in front of the foil target. It is constructed from an electronic grade polycrystalline diamond plate of 0.3 mm thickness and gives a reference time T_0 for the TOF detectors flight time measurements. For high multiplicity events, T_0 will be determined by software [Col17]. The T_0 detector is currently also used as a reference detector in the analysis of the mCBM beamtime data.

3.3 mTRD Setup 2020

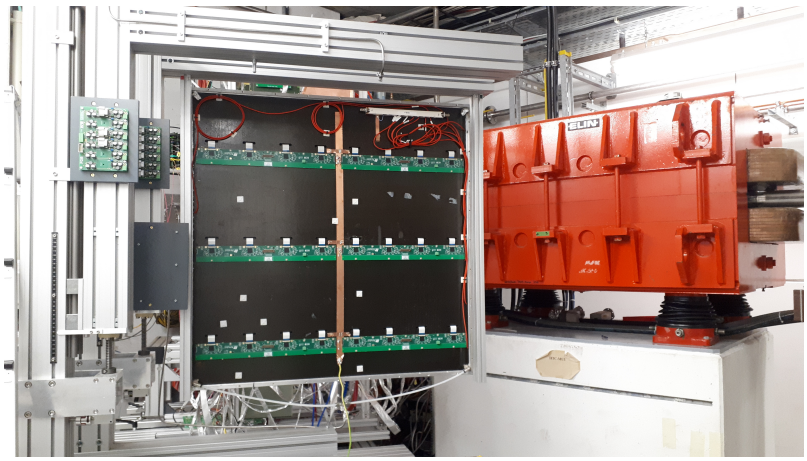

Figure 3.8: Image of the mTRD setup 2020 in the mCBM cave (rear view). The assembly is incomplete because some cables and gas connectors are missing. Six quad-FEBs are mounted on the backplate of the chamber with in total 24 SPADICs.

In the setup for the mCBM 2020 campaign, which is the origin of the data analyzed in this thesis, one TRD module was used. It has a size of 96 cm × 96 cm, corresponding to the general chamber design as foreseen for the outer modules of the future CBM-TRD. The modules padplane has in

total 768 readout channels, arranged in 6 rows with 128 channels each. For the first time the newly produced quad-FEBs were used, which each carry four SPADIC 2.2 ASICs on the same board. In Figure 3.8 the mTRD module with six of the new quad-FEBs is visible. Each SPADIC is connected to 32 pads, while due to link number limitations only 21 of the 24 SPADICs are connected to the data acquisition chain (DAQ) via the ROB visible on the left, so in total 672 of 768 channels are active. The pads each have a size of 0.72 × 15 cm^2 ($x \times y$). The read-out chambers were supplied with an Ar/CO_2 80:20 mixture by the TRD gas mixing station. Then anode voltage was 1750 V with a drift field of 100 V/mm. The detector system is equipped with multiple sensors to measure voltages and gas parameters, which are also constantly logged during operation.
Also due to travel restrictions caused by the COVID-19 pandemic, the TRD team operated the subsystem remotely after completing the on-site installations. When the mCBM testbeam took place in April/May 2020, the detector was fully controllable remotely, e.g. via SSH access to the detector and periphery controls.

3.3.1 Channel Mapping Correction

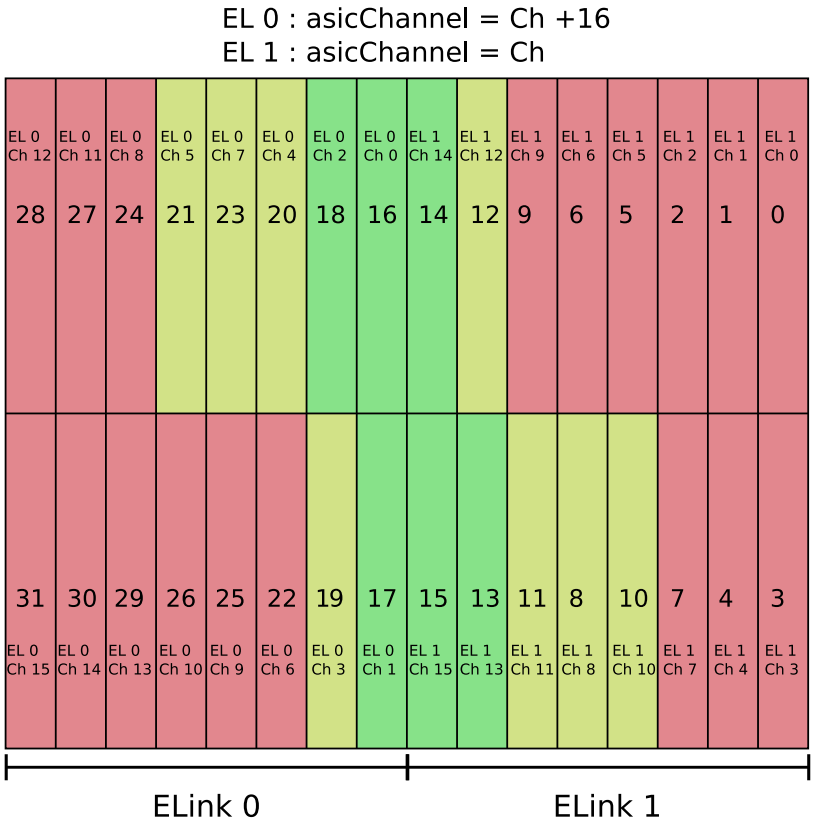

Figure 3.9: Sketch of the physical positions of the 32 channels of a SPADIC in the readout-segment of the padplane it is attached to. The big numbers on the pads indicate the ASIC/SPADIC-channel, Ch is the channel which is encoded in the SPADIC-messages and EL indicates which of the two e-links per SPADIC is connected to the pad. The colors correspond to the number of correctly configured neighbor-triggers (red: 0, yellow: 1, green: 2). Based on [KMA20] [edited].

First attempts to find spatial correlations in the recorded data showed unexpected results. It later became clear that at the time of data taking an incorrect channel mapping was used. The reason is a change in routing of the analog inputs from the padplane to the SPADIC due to a new board layout for the newly BGA-mounted SPADIC 2.2. This led to an incorrect assignment of the SPADIC messages to their physical channels on the padplane in the unpacking process of the recorded data, and therefore wrong physical positions of reconstructed hits. When this issue was noticed, a corrected channel mapping was derived from the front-end layout and confirmed using a source scan in the labratory in Münster [Kä20]. Thus the data taken in the mCBM 2020 campaign was still analyzable, but while the neighbor-readout (see subsubsection 3.1.3) partially assigned the wrong channels most channels which reached the trigger threshold did not trigger their real physical neighbor channels automatically. In Figure 3.9 an overview of the new channel mapping is visible. Additionally it is marked in color for each channel how many of its two neighboring channels were correctly assigned as neighbors in the FNR-matrix, which is called here "correct neighbor triggers". It can be seen that especially the outer channels have zero correct neighbor triggers, decreasing the resolution of the reconstructed hit positions of the message clusters recorded in these areas, unless the induced charge was high enough to exceed the self-triggering thresolds of the real neighbor channels. Fortunately in the middle of the readout segment there are six contiguous channels where both two neighbor triggers were configured correctly, which gives the opportunity to limit the analysis to the corresponding region when full position resolution of the reconstructed hits is required.

3.4 Collected Data and Eventbuilding

For the offline data analysis, which is done in this thesis, several types of data are available. They are represented by different C++ classes in the CbmRoot framework which is used to evaluate the data. It is developed by the collaboration to process the huge amount of data recorded by the detectors in a common way, based on CERNs ROOT library. The first step is always to unpack the raw data saved in timeslice archives (TSAs) which were generated by the FLES. For this task, each subsystem provides an unpacker class, e.g. `CbmMcbm2018UnpackerTaskTrdR` for TRD, which is used to process the timeslices in the TSA which contain data of the specific subsystem. They are able to interpret the bitstreams generated by their frontend electronics and convert them to basic digi classes following the naming `Cbm***Digi`, where `***` is replaced by the acronym for the specific subsystem, so that in case of TRD, the classname is `CbmTrdDigi`. The digis usually describe a trigger in the detector and contain information to unambiguously identify the origin readout element and time of the event as well as additional detector-specific information like charge and trigger type for TRD. The information contained in digis is already stripped compared to the whole output of the frontend electronics. In case of TRD, the ADC values of the recorded samples per trigger are not saved in the digi, but instead reduced to the charge derived from the signal shape (more specifically the maximum ADC value, as this is currently the best indicator for the total collected charge). To work with the real charge signals anyway, the TRD unpacker offers the option to additionally generate objects of the class `CbmTrdRawMessageSpadic`, which saves the single ADC values and other information which was discarded in the digis.

Figure 3.10 shows a schematic overview of the unpacking and reconstruction process for the data recorded by the FLES. The digis (and raw messages) are saved in a root file containing a `TTree` with an entry per timeslice. The entries contain meta information about the timeslice in form of a `TimesliceMetaData` object and `std::vector`s of digis (and raw messages if enabled) of the subsystems. This root file is then used for further reconstruction of the data. For mCBM 2020 it is the case that the data acquisition was split onto multiple FLES processing nodes, so that multiple TSAs covering the same time period are generated. They can be read in and processed at once by the unpacking macro, producing one single root file for all processing nodes, but it is also possible to seperately reconstruct them when timeslice-overlapping correlations are not required, because the splitting is done timeslice-wise. This would be an opportunity to easily split the unpacking and reconstruction process on multiple CPU cores when the degree of parallelization shall be increased. As in the analysis of the 2020 data it turned out that there are problems with the correct sorting of the TRD raw messages into the timeslices, it was dispensed to make use of this separate reconstruction in this analysis and already merge the TSA files of different processing nodes in the unpacking task instead, which is shown in Figure 3.10.

3.4.1 Eventbuilding

As a first step to reduce noise triggers in the data, an eventbuilding procedure is applied to the data. In the eventbuilding process, digis of all subsystems within a timeslice are grouped into events using an eventbuilding algorithm. The procedure is included in the reconstruction macro and happens before the hit producer algorithms are executed. In this analysis the `CbmMcbm2018EventBuilder` is used in maximum time gap mode, which means that the maximum time distance between digis grouped in the same event is limited to a maximum time length. The maximum length is set to 100 ns, a rather high value which was selected because the time reconstruction of TRD is not yet fully developed and its accuracy is in this range. The maximum time gap mode only limits the distance of consecutive digis but does not apply an upper limit for the event length. The eventbuilding process is sketched in Figure 3.11. To filter noise, it is also possible to discard events which do not contain the minimum amount of digis, which can be defined seperately for each subsystem. In this analysis each event is required to consist of 10 TOF and 3 RICH digis, otherwise it is immediately discarded. References to the digis which were assigned to the same event are stored in objects of the class `CbmEvent`, which are also saved to the output root file and can be used in the further reconstruction and analysis. The upstream TOF hit producer uses only the TOF hits which belong to an event to construct the hits, which means that when in this thesis a correlation with TOF hits is done these hits belong to a valid event consisting of coincident TOF and RICH signals.

3.4.2 Reconstructed Hits

Correlations accross multiple detectors require the reconstruction of physical hits from the digis. This is done by detector-specific hit producers which group digis belonging to the same physical particle and create hit objects which are represented by subsystem-specific classes usually (except for MUCH) inheriting from the base class `CbmPixelHit`, e. g. `CbmTrdHit`. For the subsystems TRD, MUCH, MVD, and STS there are also classes inheriting from `CbmCluster` to save references to the

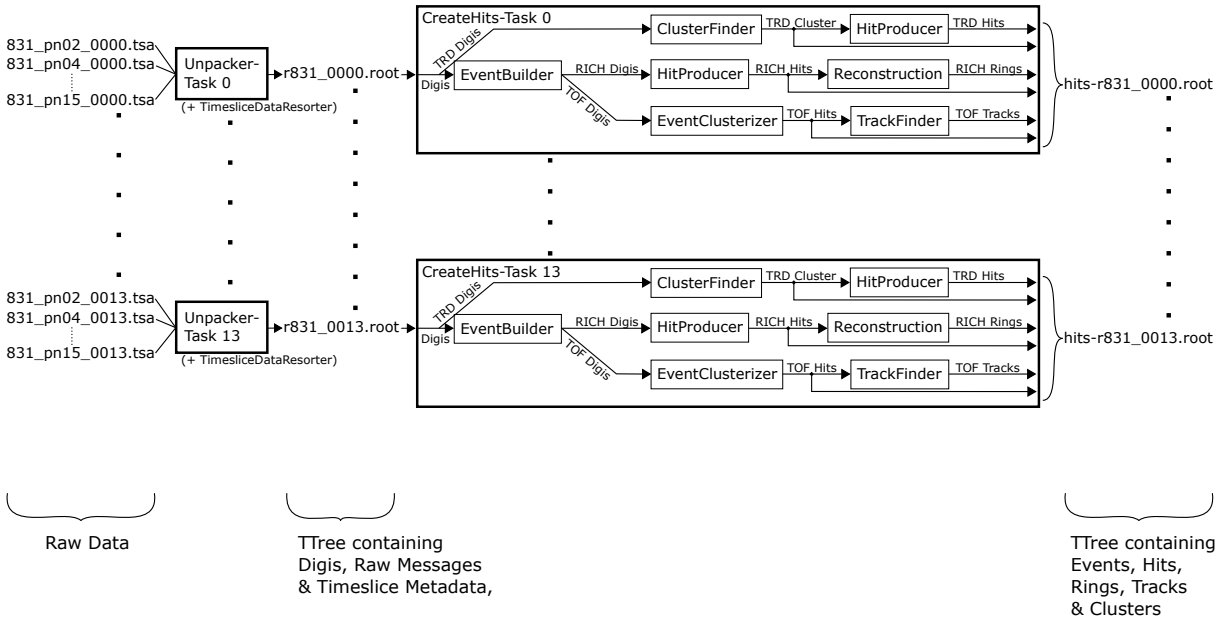

Figure 3.10: Sketch of the unpacking and reconstruction process for the timeslice archives coming from the FLES. Each processing node writes TSA files with an ending number (0000 - 0013) which is incremented when a specific amount of data is exceeded (a new TSA file is begun then). The TSAs from multiple (10) processing nodes are already merged in the unpacker task and – if a time jump correction (see below) is applied to the TRD raw messages – the TRD raw messages get resorted into their correct timeslices using the TimesliceDataResorter, which rewrites the resulting `TTree`-file (e. g. `r831_0000.root`). This `TTree`-file then contains the digis of TRD, TOF and RICH as well as the TRD raw messages. In the next step this files are given as input to the CreateHits-Task, which runs the eventbuilder on the digis and the specific reconstruction tasks for the different subsystems. The TRD cluster finder does not check if digis are grouped into events, while TOF and RICH only process digis which were assigned to valid events before. The output for the reconstruction tasks mainly relevant for the analysis in this thesis are the TRD hits and the TOF hits and tracks. They are stored in root files containing a `TTree` of the reconstructed objects, which are then merged into a single root file, ready to be entered in the custom analysis for this thesis.

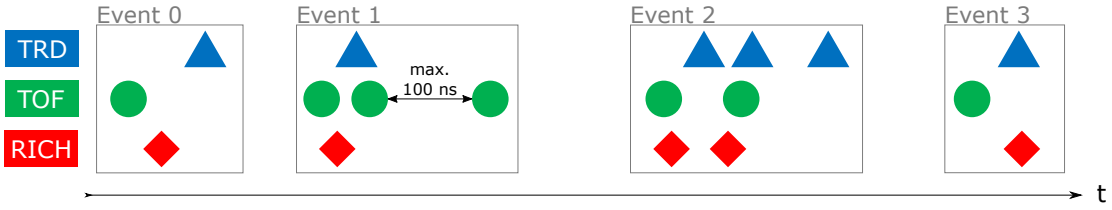

Figure 3.11: Illustration of the eventbuilding algorithm using the maximum time gap mode with digis from three subsystems, represented by different colors. The stream of digis is split into events with the condition that no digi inside an event can have a temporal distance of more than 100 ns to other digis in the same event.

digis the hits were constructed of. In case of TRD, the `CbmTrdHit` class also saves a reference to the corresponding `CbmTrdCluster` class, allowing to easily access the associated digis in the analysis. The main properties the hits provide are the position (x, y, and z) in the CBM coordinate system

as well as the time when the hit occured. Also uncertainties are provided for these measurands. In addition the classes can save subsystem-specific properties, e.g. the energy loss for TRD.
The already well advanced analysis framework of the TOF detector is also able to build tracks from the TOF hits using the `CbmTofFindTracks` track finder. TOF tracks are built by searching coincident TOF hits which lie on straight lines (as there is no magnetic field in mCBM), including the hits generated from the T0 diamond detector which are assumed to have been occured in the target spot at $x = y = z = 0$. For a given z-position, e.g. the height of the TRD module, it is then possible to calculate the x and y-positions as well as the intersection time of the track at this z-position, allowing to correlate the data with the TOF detector in this way.
All reconstructed objects are saved to an output root file corresponding to the input root file of the reconstruction macro where all generated objects are stored in one entry per timeslice, except that `TClonesArray` data containers are used instead `std::vector` at this level. It is also common to directly run the analysis inside the reconstruction macro, but as the reconstruction is the most processing time consuming part and the analysis has to be rerun constantly in the development process, the analysis is done using a separate independent C++ program here.

4 Timejump Correction of TRD Data

First attempts to analyze the data after the corrected channel mapping was applied showed little to none correlation to the TOF detector. However, analyzing only a limited amount of timeslices from the beginning of mCBM run 831, which was selected as a reference run for all subsystems, showed stronger correlations in time and space. This led to the discovery that there is a time shift for the TRD digis which changes its offset over the run time. Such a behavior was first observed on May 4, 2020, when analyzing run 760. Temporal correlations to the T_0 detector were only visible when the TRD digi times were incremented by 1280 µs. In this chapter the nature of the phenomenon and a correction procedure is described, which allows to use the the corrected data for further analyses.

4.1 Detection and Description of the Phenomenon

To prove the hypothesis that there are time shifts in the data coming from the TRD detector, a program which correlates the TRD hits with the TOF hits was developed. The software iterates over the reconstructed hit file and always keeps the hits of three TRD and three TOF timeslices at the same time in memory. It then correlates each of these TRD timeslices with each of the three TOF timeslices to ensure the detection of correlations which have a temporal distance in the order of a timeslice length with enough statistics. The results of these correlations are stored in a histogram with a bin width of 1 µs, an example is given in Figure 4.2. Whenever for a TOF hit occurring at time t a TRD hit is found in the time interval $\left[t+\tau-\frac{1}{2}\mu s,\, t+\tau+\frac{1}{2}\mu s\right)$ which depends on the TRD time shift τ, the bin corresponding to τ in the histogram is incremented. To retrace the temporal behavior of this correlation, for every time interval with a center time of $t_c = \frac{t_A+t_B}{2}$ of the run such a histogram is generated which contains the correlation pairs which have a TOF hit time within $[t_A, t_B]$. The width of this time interval is always $t_B - t_A = 3$ s. The example correlation histogram in Figure 4.2 covers the run period from $t_A = 320$ s to $t_B = 323$ s. The peaking bin is located at $\tau = 7680$ µs, which is exactly the length of six microslices. The program generates in total 655 of those histograms for run 831, starting from $t_A = 0$ s, which is incremented by 1 s for every histogram, so that the whole run time is covered and the temporal evolution of the coincidence can be analyzed. The resulting histograms are then merged into a 2D histogram which is shown in Figure 4.5, having the elapsed seconds $t = t_c$ since run start on the x-axis, the applied TRD time shift τ on the y-axis and the level of coincidence on the z-axis. The level of coincidence is defined as the contents of the 1D source histograms subtracted by a fourth grade polynomial baseline fit plotted in Figure 4.2, which gives a better peak visibility. The peaks in Figure 4.2 are always located at time shifts being integral multiples of 1280 µs, which is the length of a microslice. Figure 4.3 shows a zoomed in version of the plot where the peaking bin is visible very well. It is assumed that the peaks cannot occur on positions deviant from this scheme as this was never observed in the data. The time jumps

have always an absolute value of $\Delta\tau = 1280\,\mu s$ and can occur in both positive and negative direction. The zoomed peak in Figure 4.3 also shows an underlying broad distribution, with its average centered at slightly smaller values of τ (registered later in TOF than in TRD). The offset to the sharp peak varies for different e-links (always a few ten µs), but is in any case at lower values of τ than the main peak located at multiples of 1280 µs. In a separate analysis, briefly outlined in Figure 4.4, where TOF tracks were used instead of TOF hits as the correlation partner to the TRD hits, the relative height of the broad underlying distribution to the main peak could be decreased by limiting the x-distance of the TRD hit to the TOF track. This is a hint that the broad peak is not produced by tracks which are real correlation partners of the TRD hits. A further investigation by comparing the signal shapes of TRD hits contributing to the broad peak with the ones contributing to the sharp peak did not lead to conclusions so far. Further analysis could exclude activation of materials near the TOF system, or a behavior of the correlation routines with the given SIS18 spill structure and/or typical detector noise.

Figure 4.5 also shows that for most of the run time – visible very well in the first 200 seconds – multiple peaks are present simultaneously, which is a hint that the time shifts do not occur simultaneously for the whole detector. The smallest segment of the readout electronics which can potentially exhibit an own clock is a an e-link (half-SPADIC), and therefore the analysis is done again for each e-link separately. The e-link a TRD hit belongs to is determined by the hit position. The assignment is done according to the subdivision of the padplane shown in Figure 4.1 which was created by analyzing the position distribution of the reconstructed TRD hits and dividing the area where hits occur into the necessary amount of e-links. This approach may result in inaccurate assignments near the borders of two e-links, but as this only concerns a small fraction of the hits this can be neglected.

The results for different e-links are shown in Figure 4.6, Figure 4.7 and Figure 4.8. The plots now show no more simultaneously present peaks, which leads to the conclusion that the time shifts occur for each e-link individually. Towards higher values of $\tau \gtrapprox 13\,500\,\mu s$ there is a uniformly high level of coincidence, because the polynomial baseline fit is not sufficient in this region anymore, but, as the real peaks are still visible, a more sophisticated baseline fitting method was not used. Also for other time shifts, mainly around $\tau = 0$, higher levels of coincidence are visible due to the simple baseline fit, but also here peaks are always clearly visible.

Most e-links time shifts follow the same pattern, which can be used to group the e-links by that property. In Table 4.1 the time shift patterns are grouped and characterized. E-link 0 shows only very smeared out correlations which can be explained by the fact that only one of the two contact wires of the 8b10b connection was connected due to layout mistakes, leading to very unreliable data transmission. E-links 1 to 5 were not active in run 831 and are therefore not analyzed. For e-links 6-13 and 20-27 the same shift pattern `Pattern 1` is visible. Also e-links 18 and 19 follow `Pattern 1`, except small deviations. For e-links 14 and 15, `Pattern 1` is also visible, but shifted in negative τ-direction by 1280 µs. E-links 16 and 17 both show different, unique patterns, which have common parts with `Pattern 1`, but exhibit clearly visible differences.

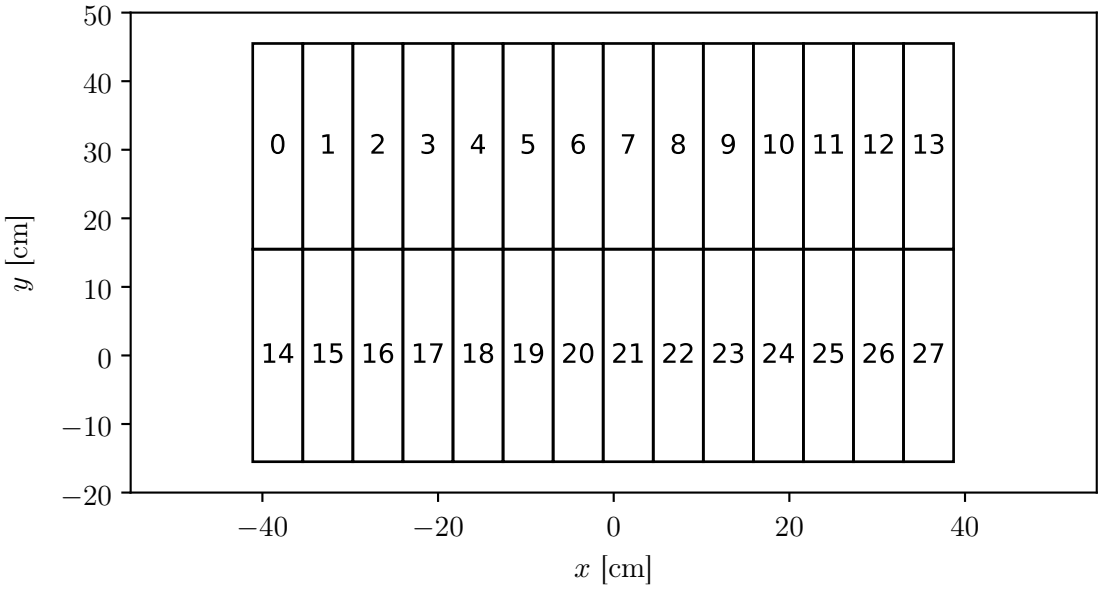

Figure 4.1: Overview of the spatial locations of the different e-links on the TRD padplane which were used to assign the correct e-link id to a TRD hit, as the hit objects do not have a member field for the e-link id nor a reference to the TRD raw messages they were built from (which have such a member field). This assignment was cross-checked with a computationally costly backsearch of TRD raw messages.

Table 4.1: Characterisation of the correlations per e-link.

E-Link	**Characterisation**
0	Strongly smeared out, not connected properly, data is not reliable
1....5	No data
6....13	`Pattern 1`
14	Mainly `Pattern 1`, but τ-shifted by 1280 µs
15	Mainly `Pattern 1`, but τ-shifted by 1280 µs
16	`Pattern 2`
17	`Pattern 3`
18	Mainly `Pattern 1`
19	Mainly `Pattern 1`
20...27	`Pattern 1`

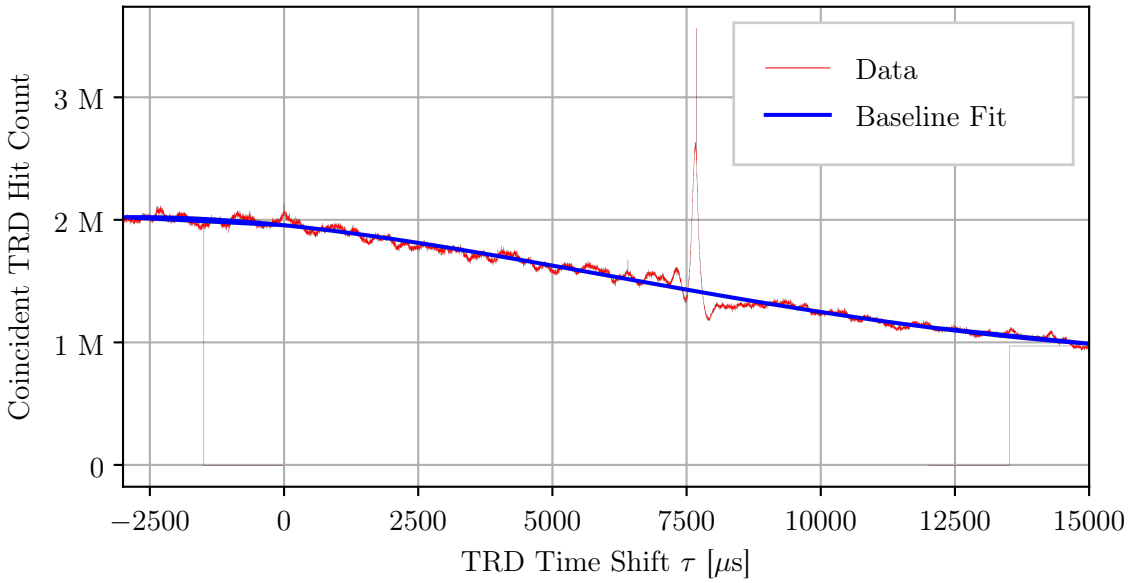

Figure 4.2: Example temporal correlation of TRD and TOF hits over multiple timslices for all e-links of run 831 from time $t_A = 320$ s to $t_B = 323$ s with a bin width of 1 µs, see text (section 4.1) for definition of the coincidence level. The peak is located at $\tau = 7680$ µs. In blue, a fourth order polynomial fit for the baseline is plotted.

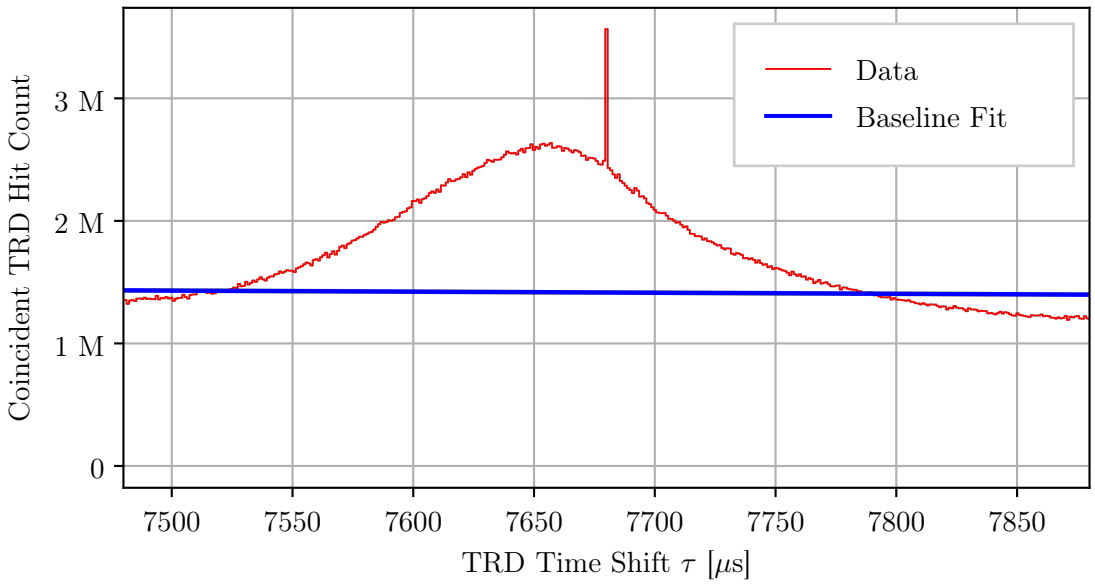

Figure 4.3: Zoom of Figure 4.2 to the correlation peak at $\tau = 7680$ µs. An underlying broad distribution is also visible and still under investigation.

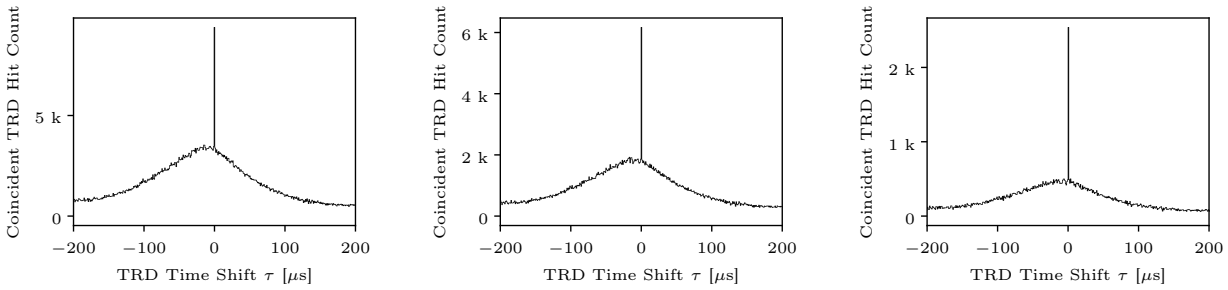

(a) for no maximum distance (b) for 2.0 cm maximum distance (c) for 0.5 cm maximum distance

Figure 4.4: Temporal correlations of TOF tracks (instead of hits) with TRD hits (x-offset corrected) for e-link 21 in run 831 (interval 35 s to 50 s). The main peak is located at $\tau = 0$, as the correction procedure described below was already applied to the data. By using tracks, their intersection point with the TRD plane can be calculated and the x-distance between the track and hit is then limited to different values (no limit, 2.0 cm and 0.5 cm). The relative height of the broad underlying peak to the main peak decreases with a more strict limitation of the distance, which is a hint that its origin are not tracks which are real correlation partners to the hits.

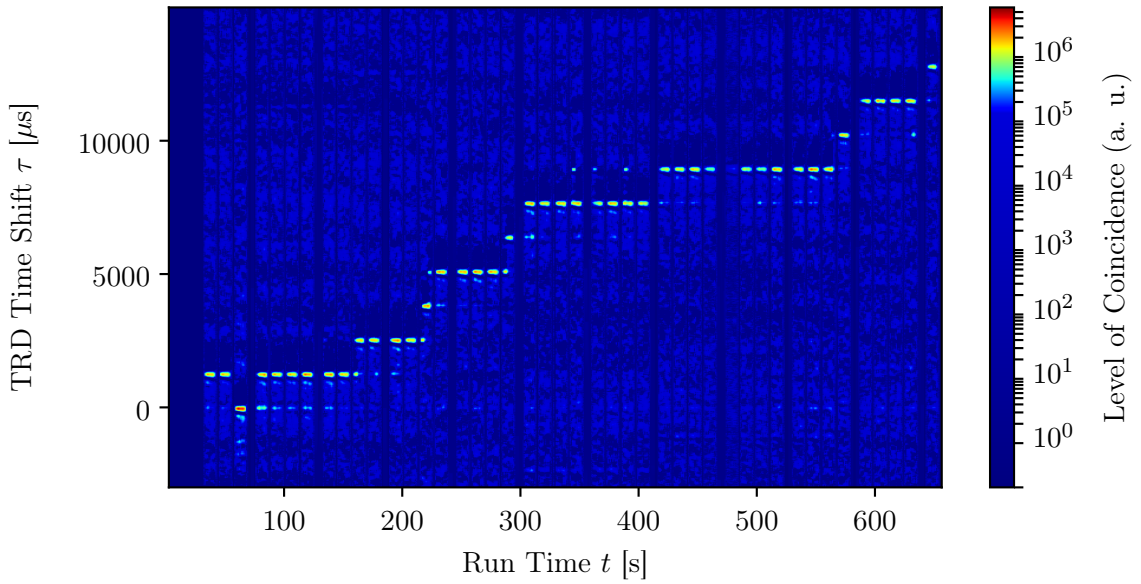

Figure 4.5: Temporal evolution within run 831 of the hit correlation plotted in Figure 4.2. The level of coincidence is the coincident hit count subtracted by the baseline fit (see section 4.1).

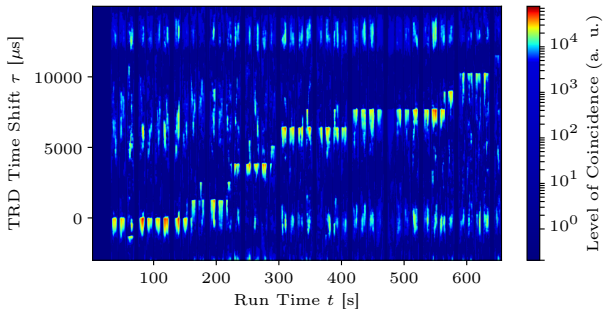

(a) E-link 0

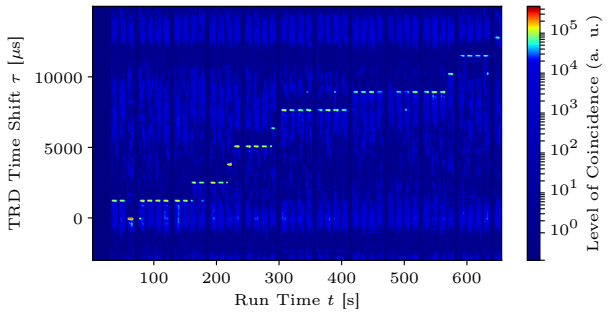

(b) E-link 6

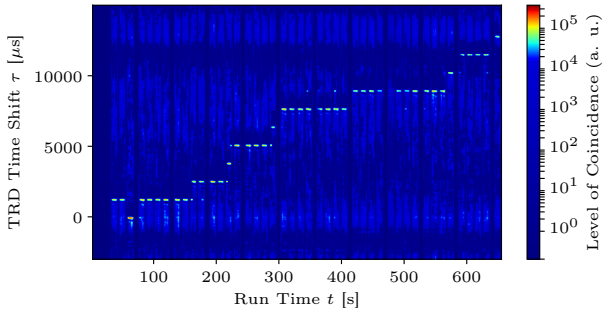

(c) E-link 7

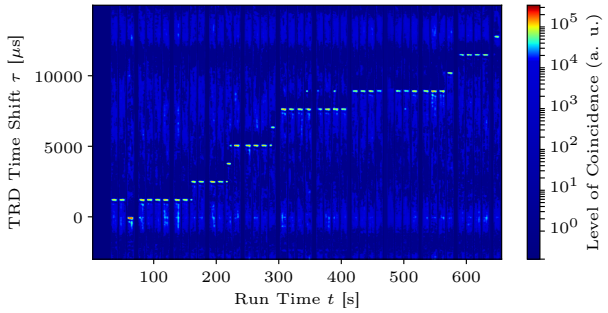

(d) E-link 8

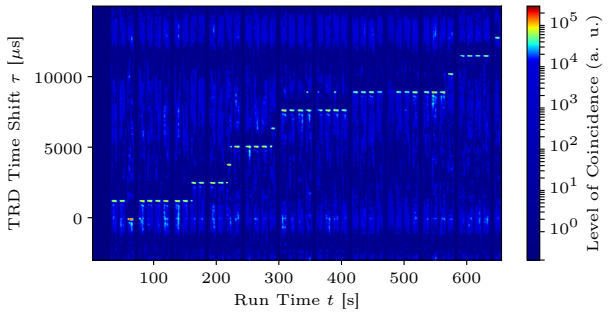

(e) E-link 9

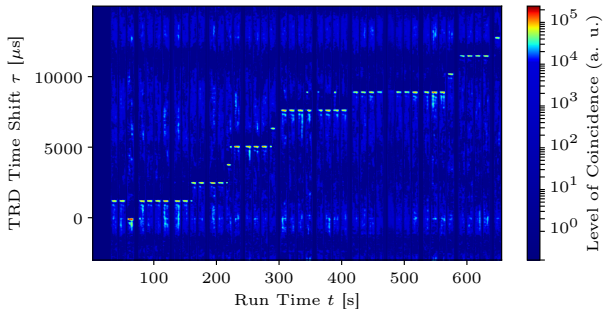

(f) E-link 10

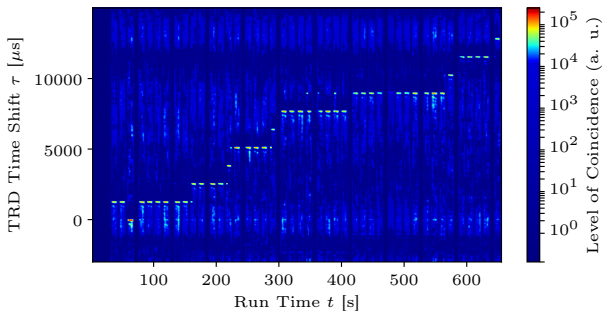

(g) E-link 11

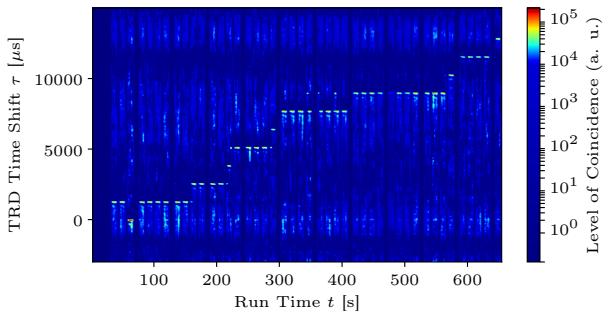

(h) E-link 12

Figure 4.6: Comparison of the temporal coincidence evolution for e-links 0-12.

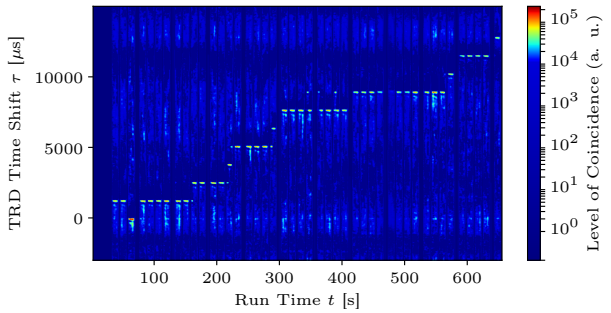

(a) E-link 13

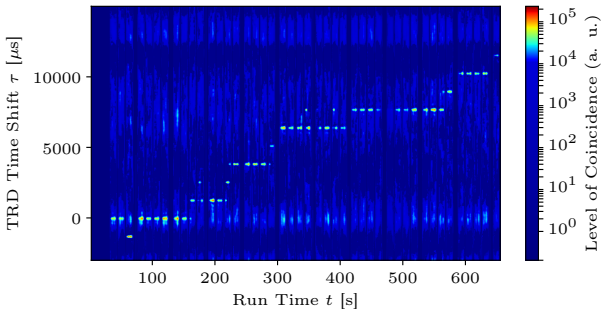

(b) E-link 14

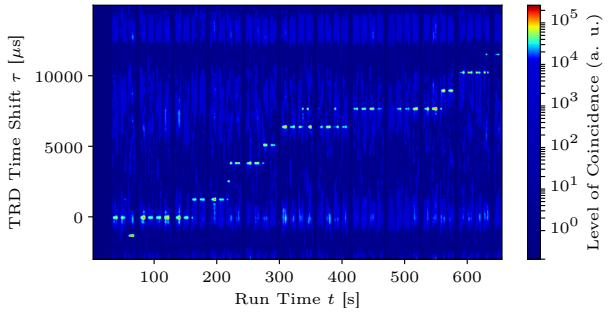

(c) E-link 15

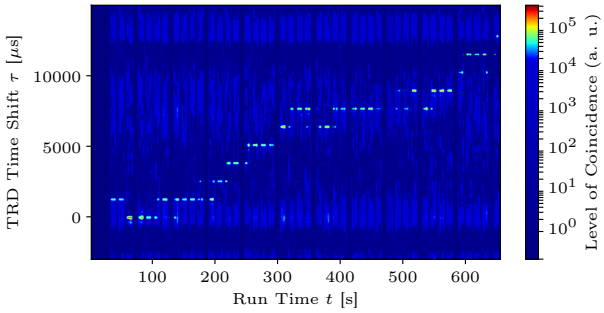

(d) E-link 16

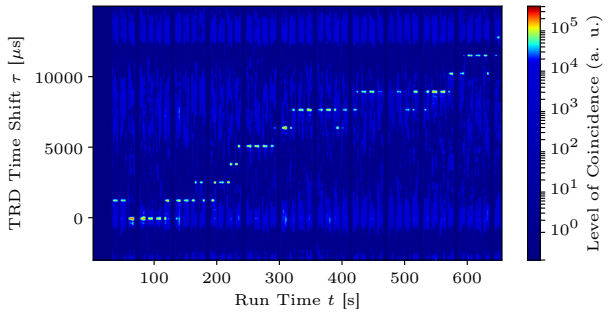

(e) E-link 17

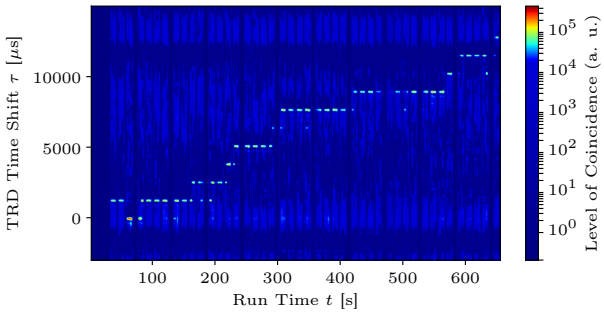

(f) E-link 18

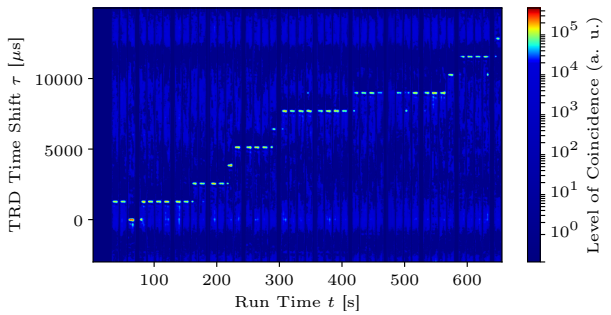

(g) E-link 19

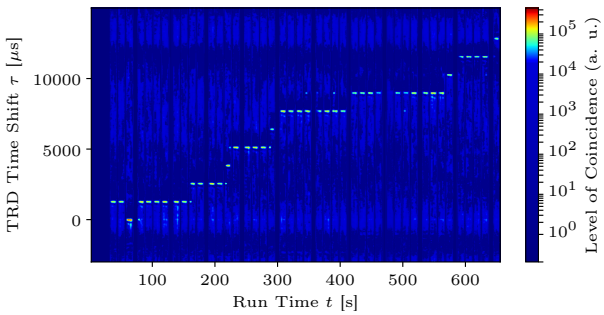

(h) E-link 20

Figure 4.7: Comparison of the temporal coincidence evolution for e-links 13-20.

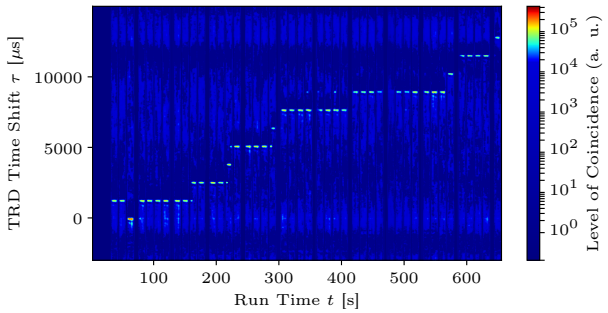

(a) E-link 21

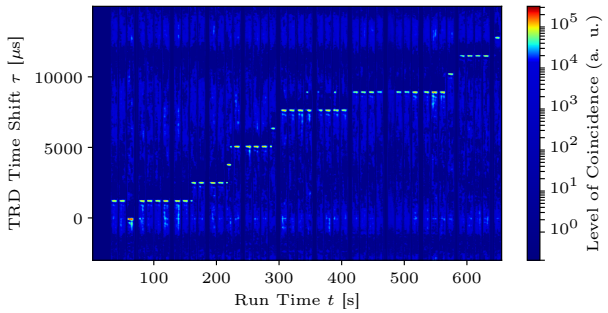

(b) E-link 22

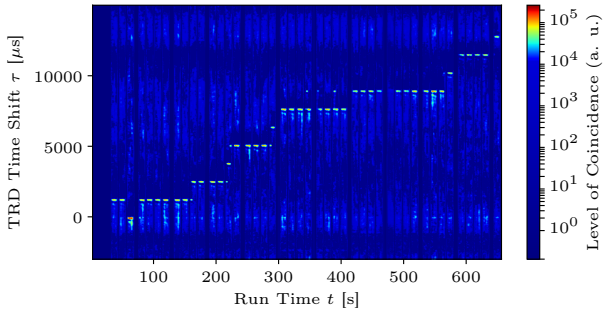

(c) E-link 23

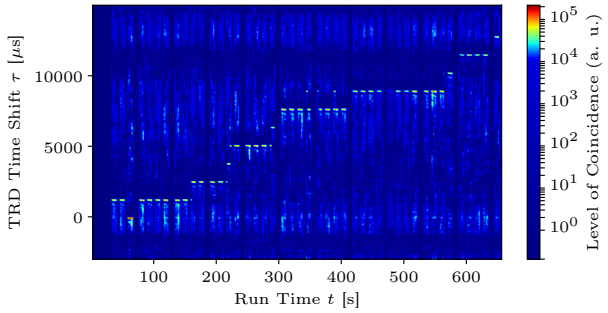

(d) E-link 24

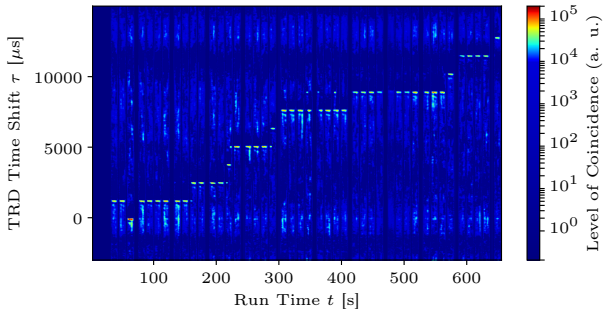

(e) E-link 25

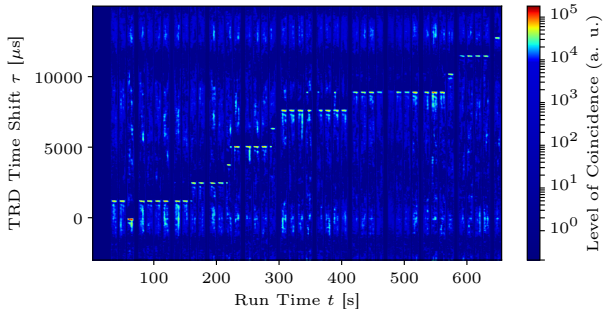

(f) E-link 26

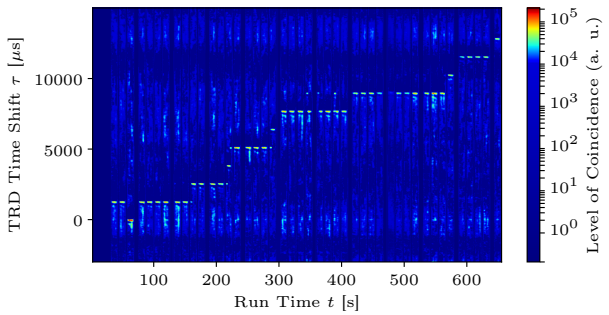

(g) E-link 27

Figure 4.8: Comparison of the temporal coincidence evolution for e-links 21-27.

4.2 Correction Procedure

In order to properly correlate the TRD data to data from other detectors, a correction procedure was developed. As each e-link exhibits these time shifts at different moments, the correction is implemented for each e-link separately. In each histogram covering a 3 second run interval, as it is exemplarily shown in Figure 4.2 for e-link 15, the height of each possible peak at $\tau = n \cdot 1280\,\mu s$ with $n \in \{-2, -1, ..., 10\}$ is measured. From the measured height the value of the baseline fit is subtracted, giving the final level of coincidence for the corresponding peak. The temporal evolution of these coincidences per peak is shown in Figure 4.9. The generation of timeslices by the DAQ was started at $t \approx 32\,s$, so in the beginning there are no peaks visible. The regular intervals in which all peak heights become zero are caused by the spill structure of SIS18. Inside a spill however, there is always one dominant peak at the discrete time shift value, for which the data need to be corrected. Due to the low statistics at the beginning and end of each spill, the peak heights fluctuate more in this region and differ only very slightly, necessitate the development of an algorithm which automatically detects the switches between discrete time shift values and is intrinsically stable against fluctuations. Thus, a procedure was implemented which works as follows:

1. Start at $t = 0$ with peak 0 as dominant peak.
2. Go to next correlation histogram and measure the heights of all peaks.
3. If another peak, which is no more than $5 \cdot 1280\,\mu s$ from the current dominant one, is at least 30 % higher as all other peaks and has at least 10 % of the maximum height of the dominant one (to be stable near offspill regions), the algorithm selects this peak as new dominant one.
4. Go to step 2.

The resulting time shifts of this algorithm are plotted for some exemplary e-links in Figure 4.10, Figure 4.11 and Figure 4.12. Figure 4.11 and Figure 4.12 both show the time shifts for e-links which follow `Pattern 1` and overlap very well besides some small artifacts. This is the expected result from the correlation plots, which shows that the algorithm described above sufficiently extracts the correct time shifts out of the data. In Figure 4.10, e-link 27, which exhibits `Pattern 1`, is compared to e-link 15, which shows the same `Pattern 1`, but τ-shifted by 1280 µs. Thus, both curves should be y-shifted by this value, as it is the case, besides some artifacts. For the other e-links the extracted time shifts also match with the expectations except for e-link 26. This e-link has lower statistics in its correlation plots than most others and the correction algorithm fails to find the correct peaks in the middle of the run, as the peak height differences seem not to reach the required significance. This can be seen in Figure 4.14. The resulting time shifts are plotted in Figure 4.13. Since the e-link, when inspecting the correlation plots by eye, matches `Pattern 1` (see Figure 4.8f), the correction time shifts from e-link 27, which also follow `Pattern 1`, are copied and used for e-link 26 as well. The time shifts defined in this overall procedure are now be used as offsets to correct the mCBM data in the following.
To do so, the TRD unpacker task was modified such that in the unpacking macro, correction intervals can be added, specified by an e-link id, a start time, an end time and the corresponding correction

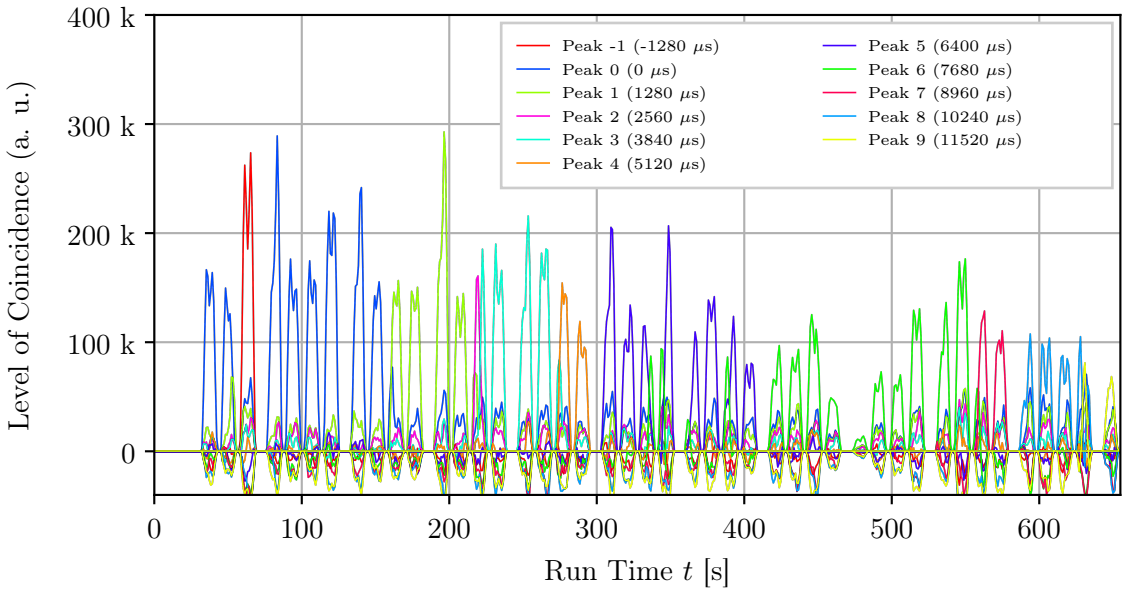

Figure 4.9: Evolution of peak heights in run 831 for e-link 15 (corresponding to Figure 4.7c). There is always one dominant peak, which results from the TRD time shift at this moment. Peaks -2 and 10 are excluded for sake of clarity as they are never dominant, but included in the correction process too.

offset. The latter is added to the raw messages with matching e-link id in the time interval. Therefore the correction offsets are the negative values of the time shifts plotted in Figure 4.10 to Figure 4.12. It is possible that the correction offset shifts the time of a raw message to a moment before or beyond the current timeslice. The unpacker processes the timeslices of the data one after the other and is in the process not able to access the data from the previous or next timeslices. Furthermore, during correlation analyses of the data, also from other subsystem teams who want to use the TRD data, it would be programmatically complex and in contrast to the analysis style usually used to access data from other timeslices. To get rid of this issue, a tool named `TimesliceDataResorter` was developed, which is available on CBMs GitLab[1]. It reads in the unpacked root file which comes out of the unpacker and resorts the TRD digis (and raw messages if present) into their correct timeslices. The output is then saved into a file which contains a new root tree, including the correctly sorted TRD data as well as the untouched data of all other subsystems and also all other present objects (directories, lists, file headers, etc.) of the input file, making it compatible with the reconstruction macro.

[1] `https://git.cbm.gsi.de/apuntke/timeslicedataresorter`

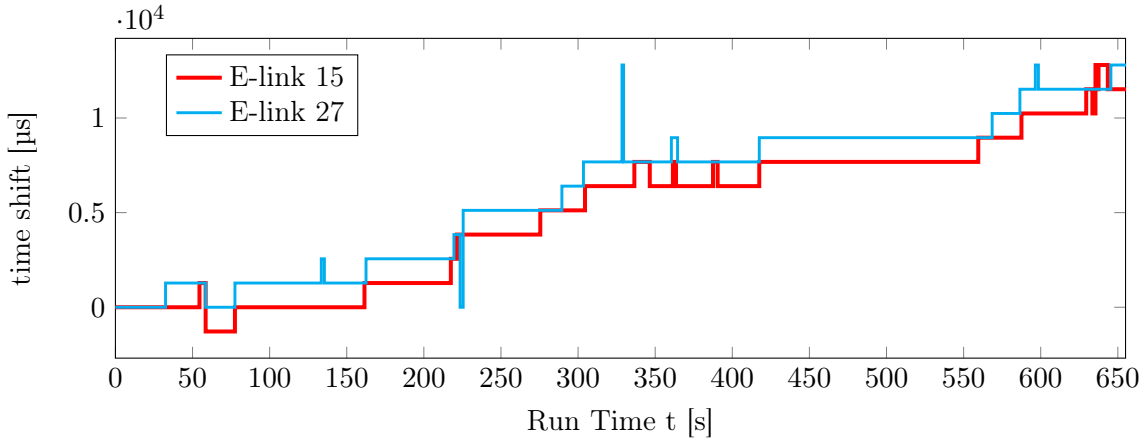

Figure 4.10: Resulting time shifts for two e-links within run 831. E-link 27 follows `Pattern 1`, while e-link 15 follows mostly the τ-shifted `Pattern 1`.

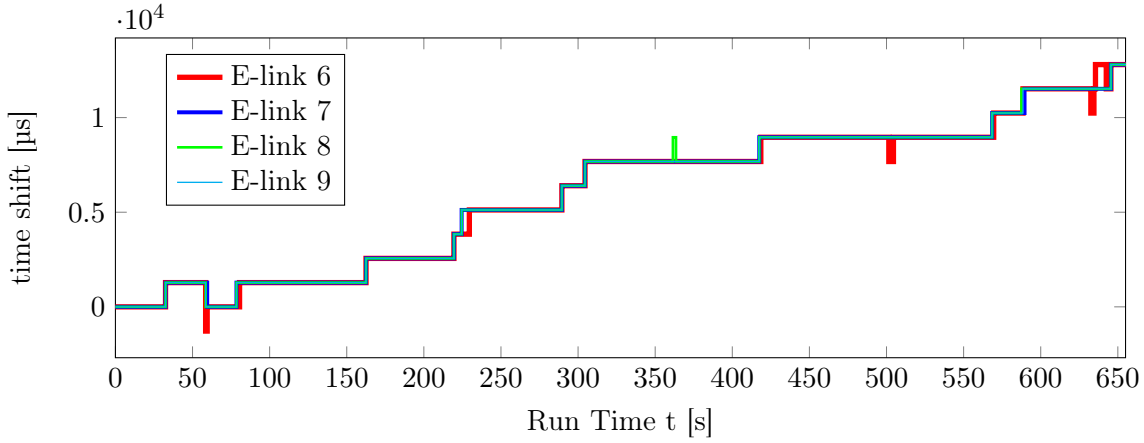

Figure 4.11: Resulting time shifts for four different e-links within run 831. They all follow `Pattern 1`, besides some artifacts.

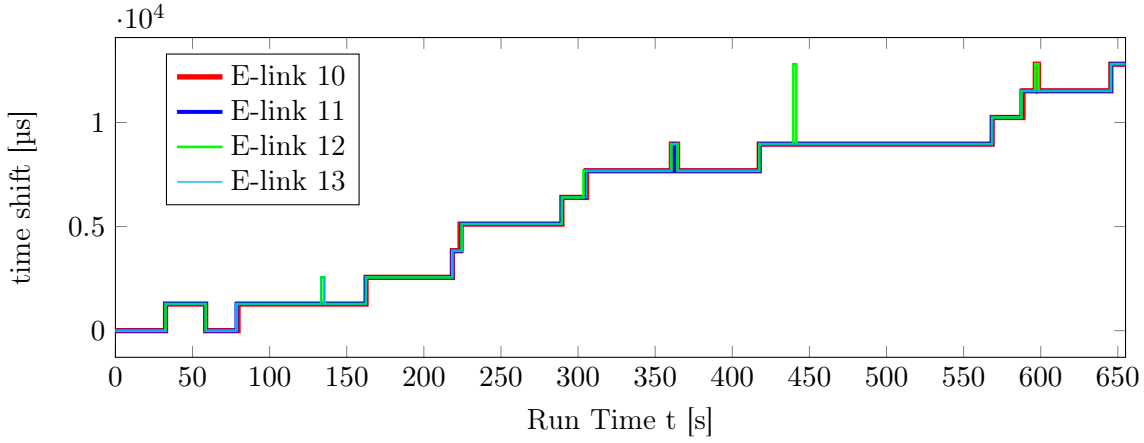

Figure 4.12: Resulting time shifts for four different e-links within run 831. They all follow `Pattern 1`, besides some artifacts.

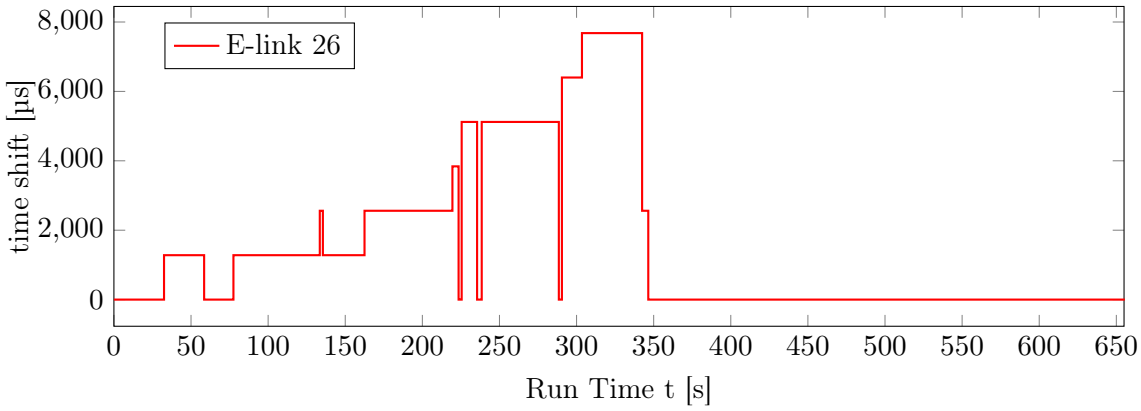

Figure 4.13: Resulting time shifts for e-link 26 within run 831, where the algorithm fails in the middle of the run. Those values are not used, but instead, the values found for e-link 27 are applied.

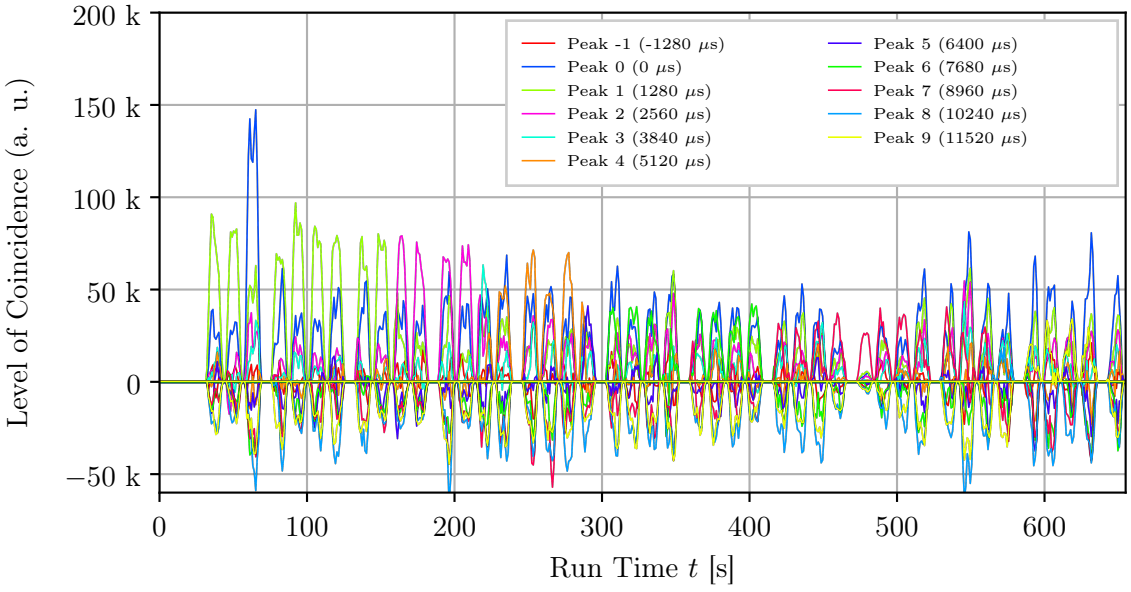

Figure 4.14: Evolution of peak heights in run 831 for e-link 26 (corresponding to Figure 4.8f). Although in the single correlation plots (covering time intervals of 3 s) by eye there are clear peaks visible, the peak heights differ only very lightly in the middle of the run at $t \approx 340\,\mathrm{s}$. Thus, the algorithm fails to find the correct peak there. Because of the limitation to switch only between peaks with a maximum time distance, it fails to find the correct time shifts for the late run too.

4.3 Resulting Corrected Data

After the correction was applied, the plots showing the level of coincidence were recomputed. For all e-links, the level of coincidence for different time shifts within run 831 is shown in Figure 4.15. In contrast to the uncorrected version of this plot (see Figure 4.5), the strongest coincidence is now always visible at zero time shift. For very short time periods, there are peaks visible at $\tau = \pm 1280\,\mu s$, which means that the correction is one microslice too small or too large at these times for some e-links. In this case, a higher statistic of the correlations or a more sophisticated algorithm to find the dominant peak would help to still improve the correction, but as the time intervals are very short, such errors are seen negligible here. In the non-logarithmically scaled peak height plot in Figure 4.16 it can also be seen that peak 0 is always the dominant one and peaks -1 and 1 only play a subordinate role. They are only visible for short time intervals where the correction is not perfect. The closest distance to peak 0 is reached at $t = 389.5\,s$ where peak 1 reaches approximately 55 % of the height of peak 0. At all other times peak -1 and 1 never reach 40 % of peak 0s height. All in all the result is satisfactory and the TRD data is now available to further analysis by this correction, in particular for correlation with other subsystems as one of the next QA steps on the recorded data, which is done in the next section.

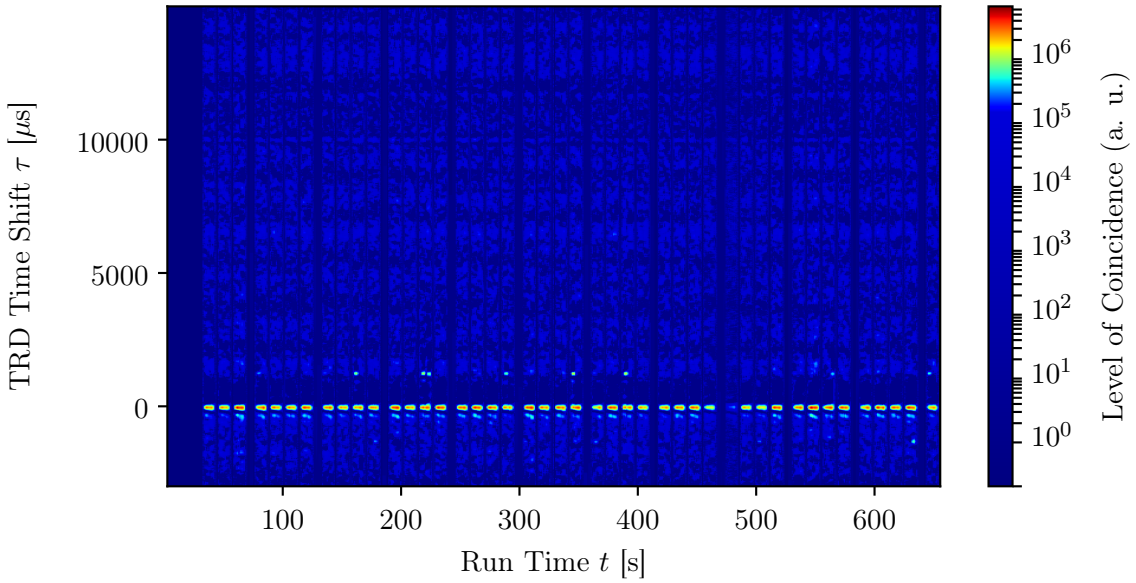

Figure 4.15: Level of coincidence within run 831 for different time shifts for the corrected data of all e-links. The strongest correlation is now seen on zero time shift, except some small deviations by a timeslice length for short parts. This is interpreted as confirmation for the correction procedure. The level of coincidence is the coincident hit count subtracted by the baseline fit (see section 4.1).

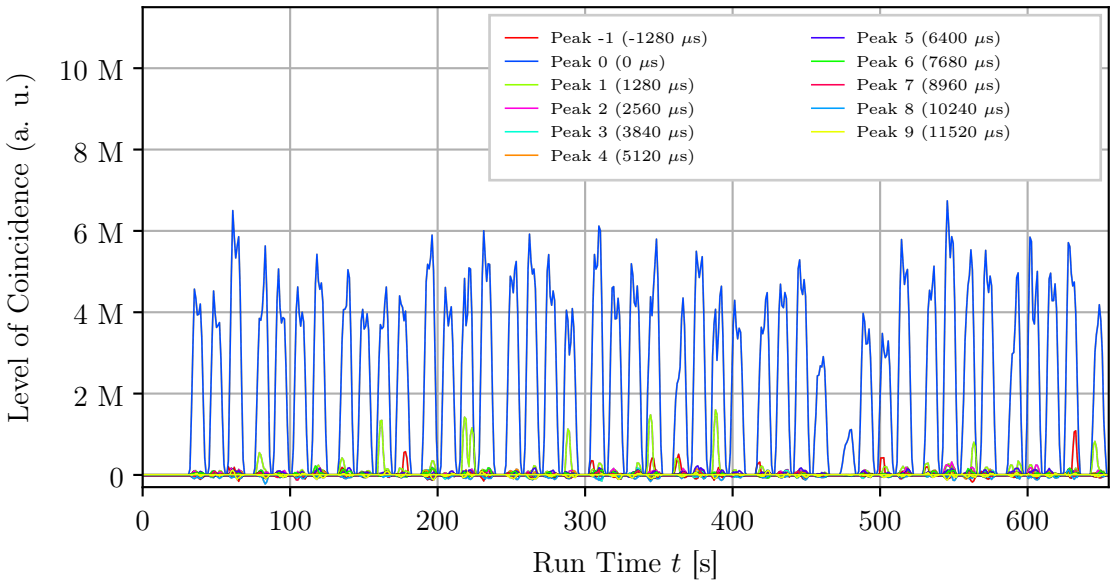

Figure 4.16: Evolution of peak heights in run 831 for all e-links after the time correction (corresponding to Figure 4.15). Peak 0 is now always the dominant one. The small peaks for -1 and 1 microslice lengths indicate smaller imprecisions of the correction, e.g. a slight shift of the proper moment of "time switching", but stays clearly on the negligible level.

5 Data Analysis and Results

The analysis presented in this chapter is based on data from mCBM 202 reference run 831. To verify temporal and spatial correlations of TRD to the other participating subsystems, the hits and tracks from the TOF detector are used as a reference. Therefore, it is given an overview about their spatial distributions first, to be able to later interpret the spatial correlation results and to identify common areas where a coincidence analysis is possible. In the end, a method to measure the coincidence between TRD and TOF in a reference area is presented and the results are shown.

5.1 Event Analysis

In Figure 5.1 the distribution of the lengths of the events is shown. Starting from 125 ns, at event lengths which are multiples of 62.5 ns – the SPADIC clock cycle – peaks in the distribution are visible. This can be explained by events which start and end with a TRD digi, yielding event lengths which are consequently a multiple of the SPADIC clock cycle. Figure 5.3 shows at which ratio each detector starts and closes the event for each event length. Here at the spiking positions the ratio of TRD is increased with respect to the neighboring bins, which supports the thesis of events beginning and ending with a TRD digi.
The distribution has a long tail towards higher event lengths, which is possible because the event-building algorithm has no limit for the event lengths and the maximum time gap parameter for the eventbuilding is set rather high, also due to the still only rough TRD time precision (full reconstruction to be implemented). An explanation could be too much noise, which artificially prolongs the events, or events which have shorter time distances than 100 ns, resulting in pile-up of multiple events. In a previous version of this analysis, an even higher maximum time gap of 250 ns was used, which led to a distribution which was even more smeared out towards higher event lengths and lower peaks. At high event lengths larger than 500 ns it can be seen in Figure 5.3b that most events end with a TRD or RICH digi and rarely with a TOF digi, which is an indicator that noise originating from RICH or TRD prolongs the events.
The peak at $l \approx 40$ ns is the highest peak and in Figure 5.2 it can be seen that those events mostly contain multiple TOF and RICH digis and in many cases zero TRD digis. This is also related to the event selection limits (an event has to contain at least 10 TOF- and 3 RICH-digis), but it can clearly be seen that there is an aggregation of entries reaching towards higher multiplicities for TOF and RICH. As for all events in general, most events in this peak start with a TOF digi. For the ending digi, TOF and RICH have approximately the same ratio. At an event length of $l \approx 200$ ns there is another peak visible which contains in contrast to the first peak much TRD digis. Figure 5.3b shows that the events in this peak tend to end with a TRD digi and in the correlation analysis from TRD and TOF (see below) it is visible, that the time difference between TOF (which

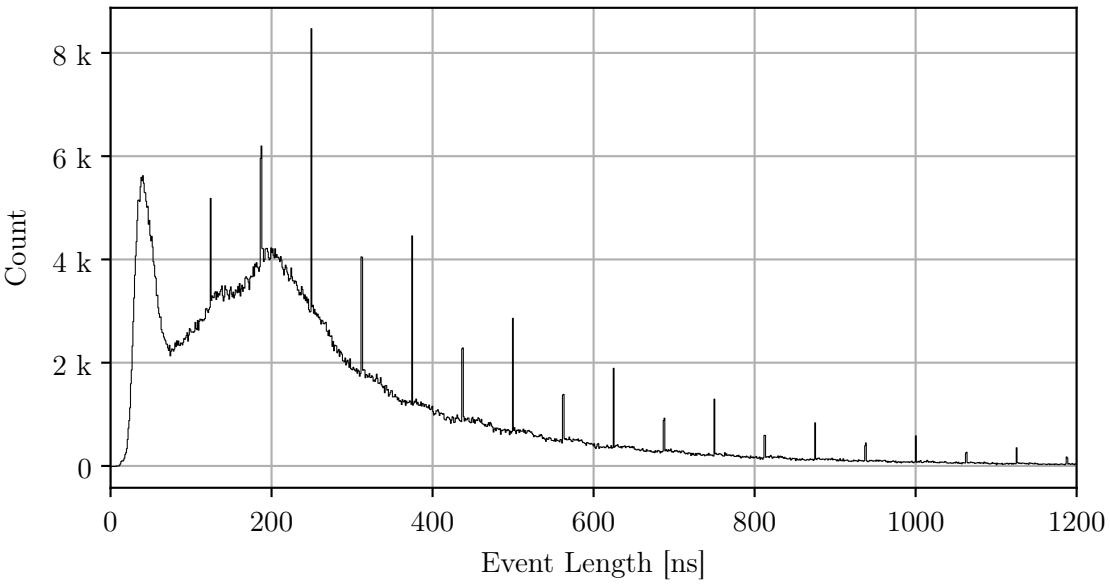

Figure 5.1: Distribution of the event lengths in run 831.

starts almost every event) and TRD is in this order of magnitude. The events produced with this length can be interpreted as more complete than the ones in the first peak, because they contain the TRD digis. The peak is smaller than the first one, but covers more events due to its width. These events are only produced if the time gap between TRD and the other detectors is filled with other digis (e.g. noise). The time reconstruction of TRD needs to be improved in the future to fix this issue, while in this analysis, the events mostly without TRD digis can be accepted, as assignment of TRD digis to events is not required in the further processing. Instead, correlations are inspected within independent correlation time windows. The eventbuilding is simply done because the TOF reconstruction requires it and it reduces noise for TOF, which is used as reference in the correlation process. It would also not be a good choice to extend the maximum time gap towards higher values, as the events are then artificially elongated and the noise reduction for TOF is worsened hereby.
Figure 5.4 shows the multiplicities of tracks and hits per event. While for TOF in every event at least one track can be found and in many cases even more tracks, for TRD in most cases no hit was found within the event time borders. This can be explained by the clearly larger acceptance of the TOF and also by the previously mentioned events which do not contain any TRD digis due to the small maximum time gap. Another factor is the event selection, which deletes events containing less than 10 TOF digis, while for TRD such a trigger is not set. This further biases the events to have more likely TOF tracks than TRD hits included.

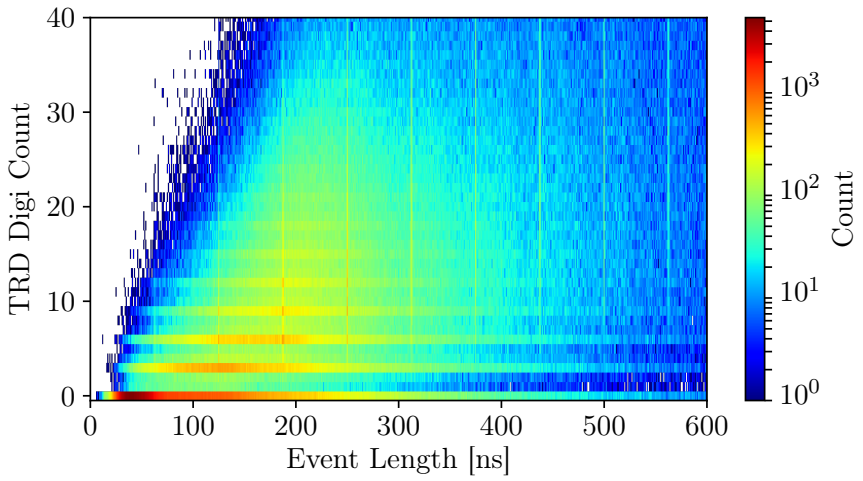

(a) for TRD

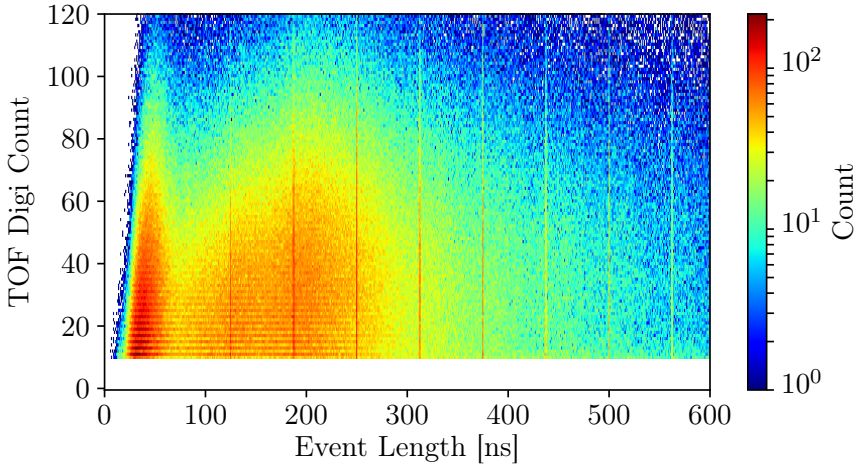

(b) for TOF

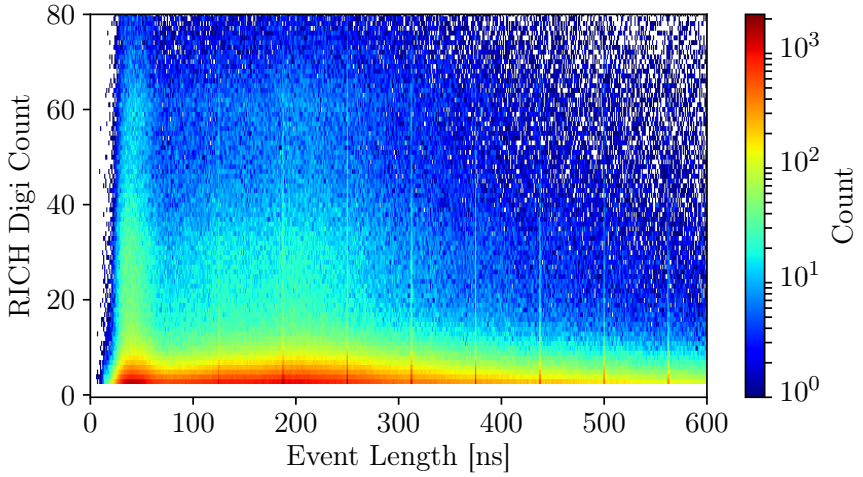

(c) for RICH

Figure 5.2: Digi multiplicity per event for different event lengths in run 831. The TRD digi multiplicity tends to be dividable by 3 because each triggered pad triggers its both neighbor pads.

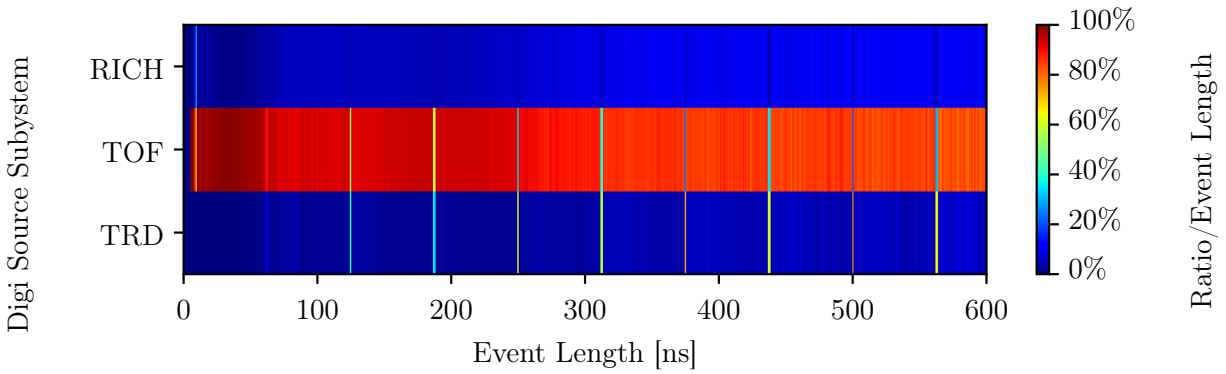

(a) Source detector of the first digi in an event

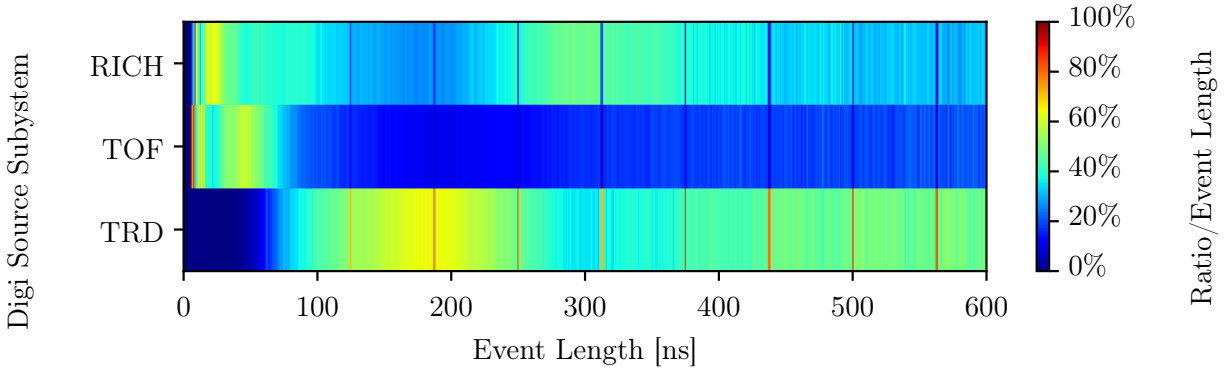

(b) Source detector of the last digi in an event

Figure 5.3: For events of different length, the ratio of the source system the first and last digi in an event originated from is plotted. A y-projection in this plots always sums to 100%, which impresses TRDs 62.5 ns pattern also to the other two subsystems. Most events start with a TOF digi.

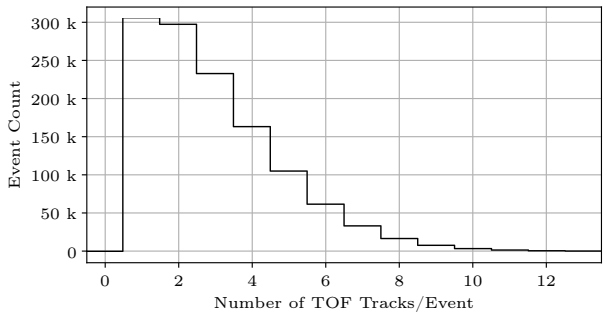

(a) Distribution of the number of TOF tracks per event in run 831.

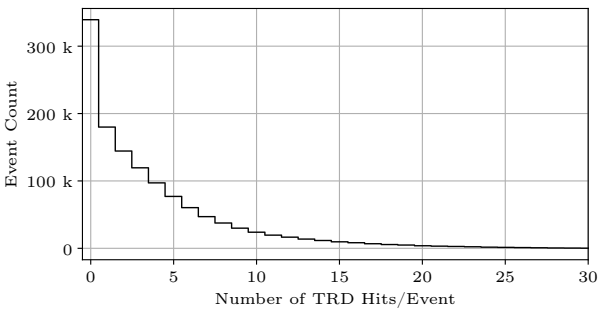

(b) Distribution of the number of TRD hits per event in run 831.

Figure 5.4: TOF track and TRD hit multiplicities per event in run 831.

5.2 TRD Cluster Sizes and Charge Spectrums for Selected Padplane Regions

The padplane segment shown in Figure 3.9, which is read out by one SPADIC with its 32 channels in total, can be divided in three regions according to the neighbor-trigger (NT) matrix configuration: The region of the green channels, where both neighbor-triggers were set correctly, the yellow regions, where only one NT was correctly set and the red ones, where no NT was correctly configured. To shed light on the impact of this problem on the clusters, three groups of clusters were selected out of all clusters recorded in run 831, and the distribution of their sizes and charges were plotted in Figure 5.5 and Figure 5.6. The groups are built by examining the amount of correctly configured NTs of all self-triggered and self-and-neighbor-triggered digis the cluster consists of. In the green group, each of those digis must be recorded on a green channel and therefore have two correctly set NTs. For the yellow and red ones those all digis must be recorded on a yellow resp. a red channel analogously. Therefore, the three groups indicate the quality of the NT configuration. The size distribution in Figure 5.5 shows clear peaks for each group which are at the expected positions: In the green region, 62 % of the clusters consist out of three digis, 12 % are even of size four. 20 % have a size of two digis, which can happen due to too much load and therefore by transmission loss from readout channels. In the yellow region, the most probable cluster size is two with 75 % probability, but also 3-pad (5 %) and 4-pad (9 %) clusters are found there, which can be created when the induced charge is high enough to trigger the physical neighbors on its own, not depending on the NT mechanism. But also cluster sizes of only one digi are found in this region due to rejection of hits in the SPADIC at high-load situations. The red distribution for zero correct NTs is only shifted by one to the left (except that there are of course no clusters of size zero) and has still a relatively high value of 10 % for cluster sizes of three. This is also a hint that there are sometimes charges induced into multiple adjacent pads which are high enough to self-trigger multiple channels.
The charge distributions in Figure 5.6 for the three groups all begin to rise at a value of 150 ADU (analog digital converter units), which is a characteristic value of the trigger thresholds used. The peaks at 450 ADU and 910 ADU are produced by situations when one or two pads in the cluster are clipping (produced in the analog part of the SPADIC), which shifts entries from clusters which have actually a higher charge to the left towards lower charges, as those high charges cannot be represented by the samples anymore. In a logarithmic y-scaling there would also be visible clipping peaks for higher amounts of clipping pads (up to 6) which are all equally distanced by 460 ADUs. Overall, the distribution is in line with expectations. The distribution for clusters belonging to the group with zero correct NTs peaks at the lowest ADU value, the one for two correct NT clusters at the highest value and the one for one correct NTs has its peak located between them.

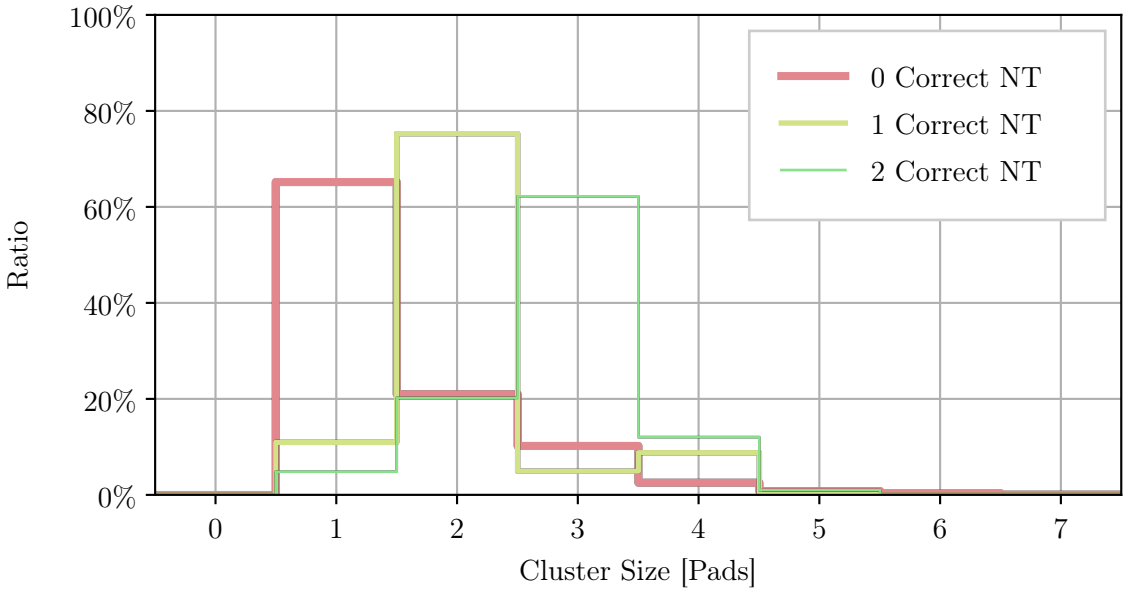

Figure 5.5: Normalized distribution of cluster sizes for three selected groups of clusters. In each group, all self-triggered (or self- and neighbor-triggered) digis the cluster consists of have to be recorded by channels which have 2, 1 or 0 correct neighbor triggers.

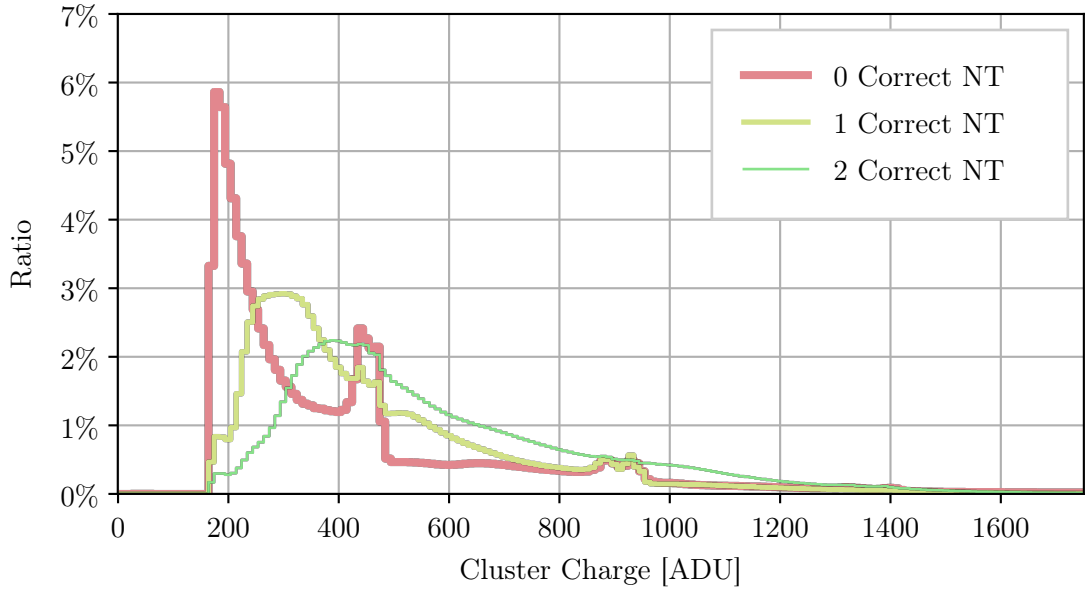

Figure 5.6: Normalized distribution of cluster charges for the three selected groups of clusters.

5.3 Spatial Distributions of Hits and Tracks

In this section, the spatial distributions of the TRD hits and TOF tracks are shown. As in the later correlation analysis these physical observables should be correlated, the knowledge of their properties is necessary for the interpretation of the correlation results.

5.3.1 TRD Hits

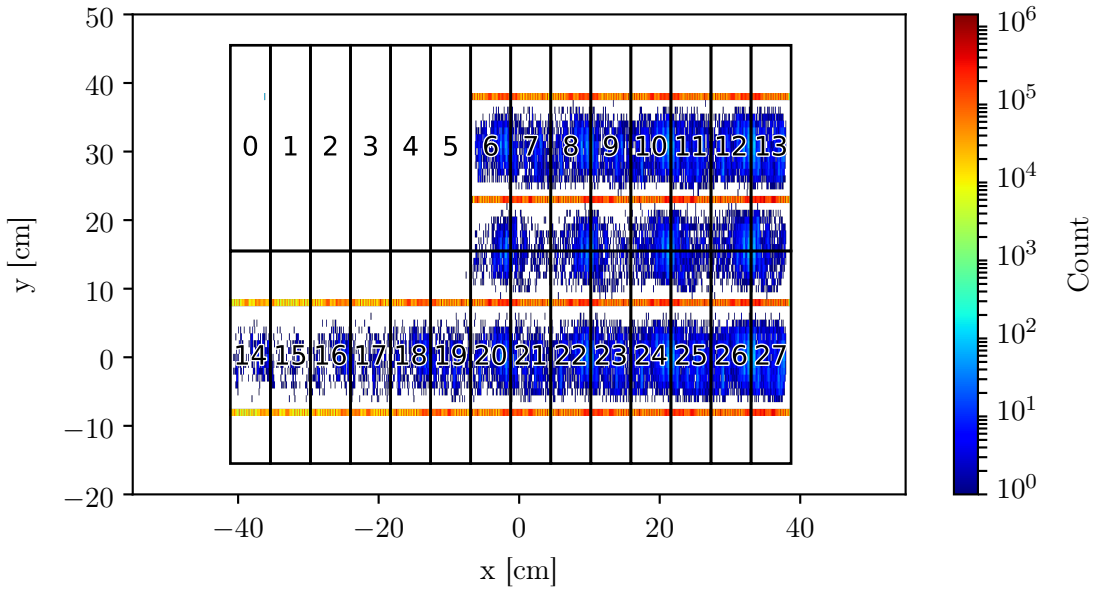

Figure 5.7: Distribution of TRD hits in run 831. For orientation, the TRD e-links are sketched, which each consist of two horizontal rows of channels. In total there were recorded approximately 371 million TRD hits.

The 2-dimensional spatial distribution of the TRD hits for the whole run 831 is plotted in Figure 5.7. For orientation, the geometrical borders and IDs of the e-links are sketched additionally. In run 831, the e-links 0 to 5 as well as the whole lower row (id 28 to 41) did not transmit data and therefore no hits were recorded in this area. Because of the high rates in this run, FEB0 and FEB1 were disabled. For the correctly working e-links there are always two parallel horizontal lines of hits visible, because the precise position reconstruction of a module works only in one direction – x in this case – while for the other direction there is in most cases the pad mid used as the y coordinate and in rare cases, when the cluster spans over two pads adjacent in y direction, a position between the two pad mids is calculated.

Figure 5.8 shows the TRD hit distribution only in x direction. In red, the ASIC borders are sketched (one ASIC for two e-links). For the three leftmost ASIC regions the hit count is reduced in comparison to the righter ASIC regions because of the 6 electrically unconnected e-links. The distribution reveals that the hit positions are biased towards specific positions which correspond to the pad mids, as the distribution has 16 equally distanced spikes in one ASIC region. Another observation is an increased hit count near the ASIC borders. To understand this, the hit distribution was plotted again for different cluster sizes (1 to 4 digis) in Figure 5.9. The 1-pad cluster distribution

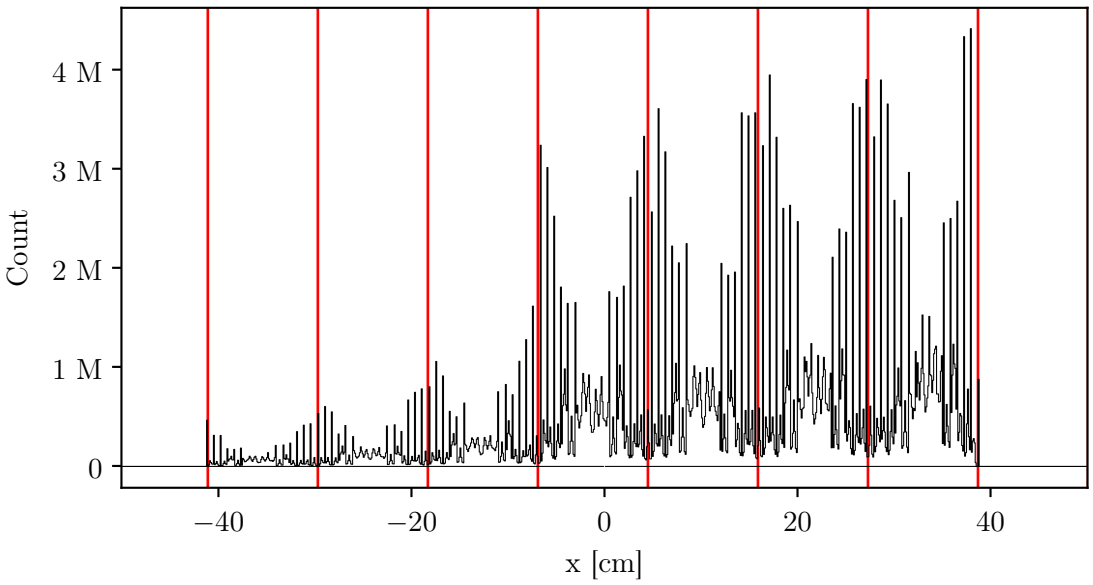

Figure 5.8: Distribution of x-positions of the TRD hits in run 831. Vertical red lines indicate the borders of the SPADICs.

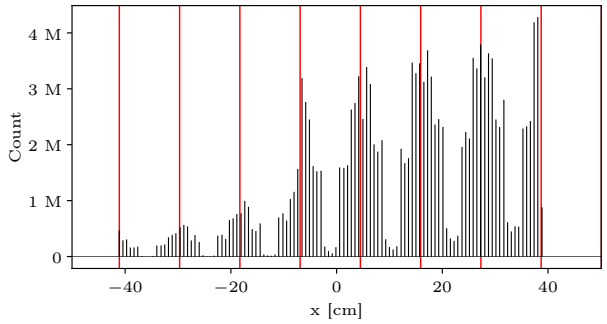

(a) 1-pad cluster

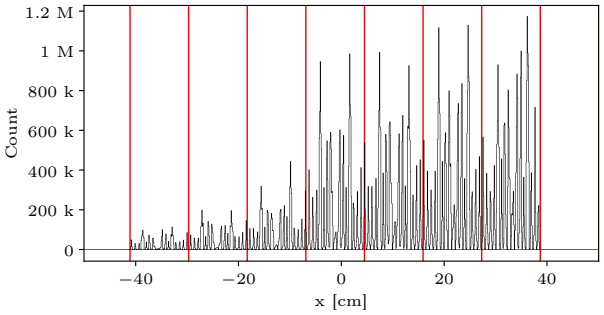

(b) 2-pad cluster

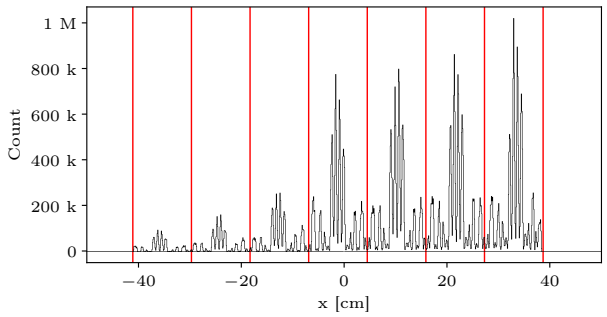

(c) 3-pad cluster

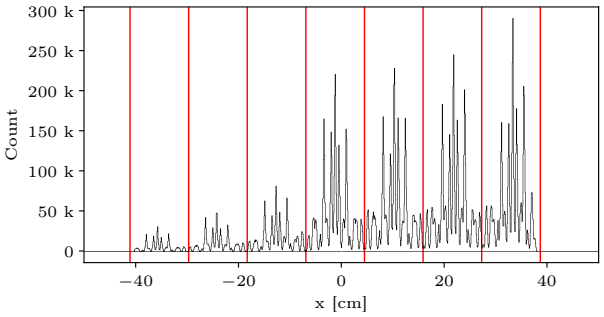

(d) 4-pad cluster

Figure 5.9: TRD hit distribution of hits consisting of clusters with different amount of pads. Vertical red lines indicate the borders of the SPADICs.

reaches the highest hit counts near the ASIC borders and has in general the highest peaks of all four plots. Thus, 1-pad clusters are mainly responsible for the high amount of reconstructed positions near the ASIC borders. This can be understood when looking at the neighbor-trigger configuration in Figure 3.9. On the ASIC borders each pad has zero correct neighbor triggers, and therefore there is a high chance to produce 1-pad clusters there. In contrast to that, for the center regions of the ASICS the distributions for 3-pad and 4-pad clusters have their highest peaks there while having less entries near the ASIC borders, as the neighbor-triggers are correctly configured in this region. Nevertheless, these 3- and 4-pad distributions still have a bias towards the pad mids. This is explained by a bias of the center-of-gravity (COG) algorithm towards the pad center [Fid20].
The distribution for the 2-pad clusters also fits in the scheme, as here the highest peaks occur around the centers of the ASICs where two correct neighbor-triggers were set.

5.3.2 TOF Hits

The spatial distribution of TOF hits is plotted in Figure 5.10 and the spot of highest intensity is visible at $x \approx 5\,\text{cm}$, $y \approx 0\,\text{cm}$. Because the TOF hits also contain the hits of the T0 diamond detector, they were filtered by requiring $z \geq 2\,\text{cm}$. The distribution shows horizontal stripes with higher hit intensity at positions where multiple TOF modules overlap. It shall be reminded here, that only TOF digis contained in valid events with sufficient TOF and RICH digis are merged into hits.

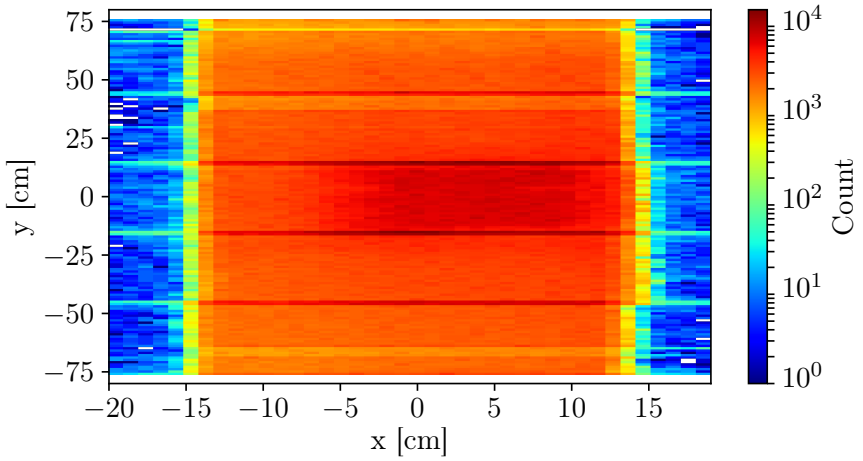

Figure 5.10: Distribution of TOF hits in run 831. In total there were recorded approximately 14.9 million TOF hits.

5.3.3 TOF Tracks

Figure 5.11 shows the spatial distribution of the TOF tracks at $z = 178.6\,\text{cm}$, the z-position of the TRD module, which were reconstructed out of the TOF hits. For orientation, also the geometric borders of the TRD e-links are sketched. Fortunately, the e-links 0 to 5 (electrically unconnected) do not cover a region with high track intensity. In the middle of the distribution at about $x \approx 5\,\text{cm}$, $y \approx 0\,\text{cm}$ there is a spot of high intensity visible, which region is fully covered by working TRD

e-links. In Figure 5.12, the distribution of TOF tracks is shown at $z = 0$, the height of the target. The origin of the mCBM coordinate system is defined by the targets position, and this position is also added as a tracking station for the TOF track reconstruction algorithm. This results in a high amount of tracks which originate from $x = y = z = 0$, as visible in the plot. It is also possible for the track finder to build tracks which do not cross the target point, but these tracks have an intensity multiple orders of magnitude below the tracks from the target spot.

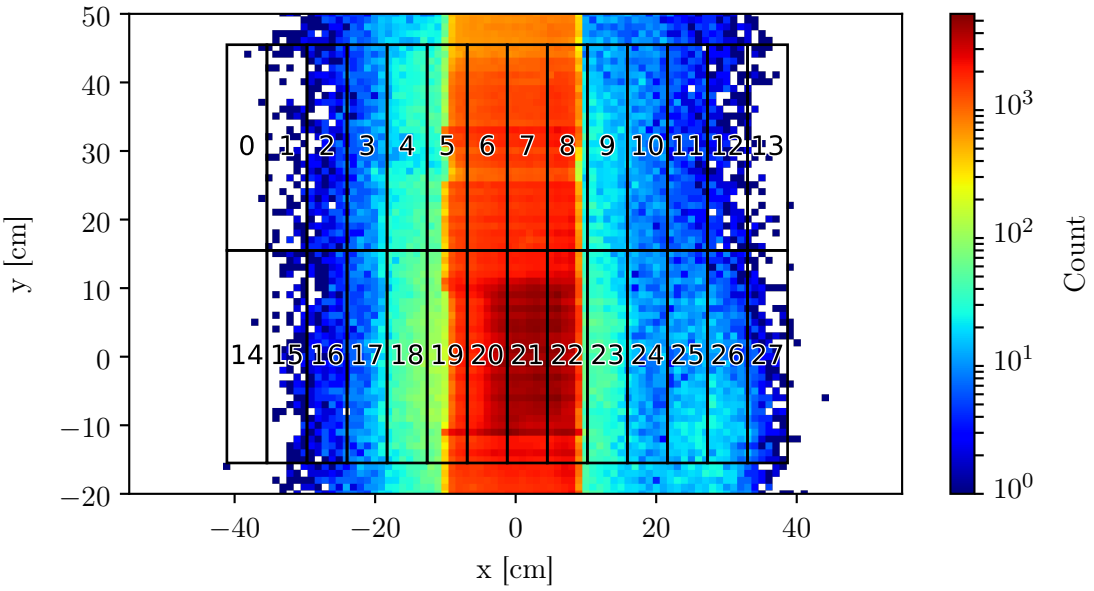

Figure 5.11: Distribution of TOF tracks in run 831 at the z-position of the TRD module ($z = 178.6\,\text{cm}$). The TRD e-links are also sketched for orientation.

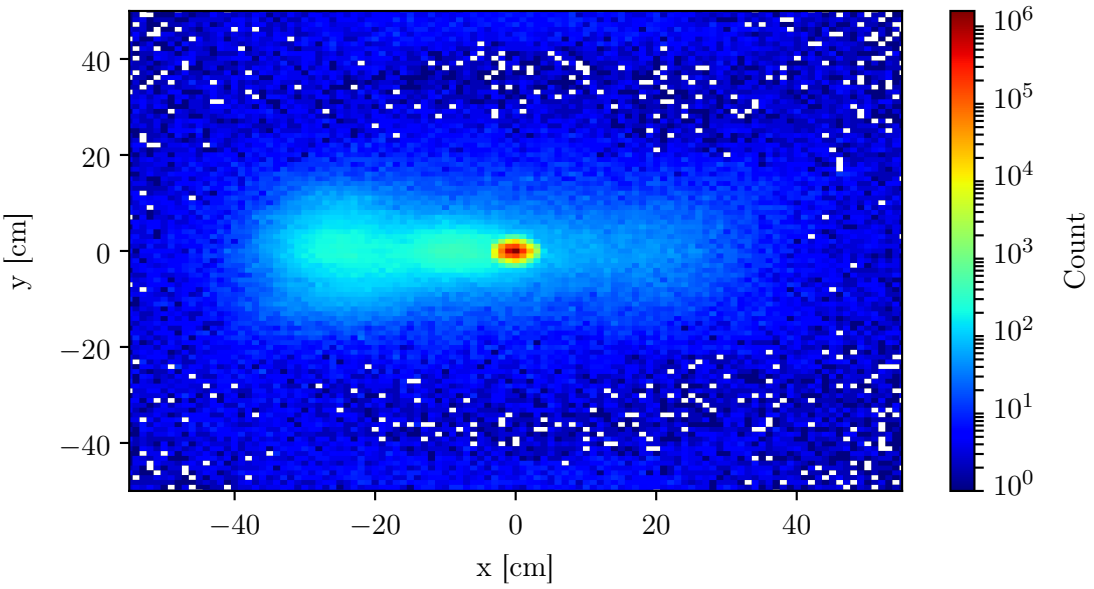

Figure 5.12: Distribution of TOF tracks in run 831 at $z = 0$ (height of the target). Because the target point is added as a tracking station for TOF, most tracks point to the target.

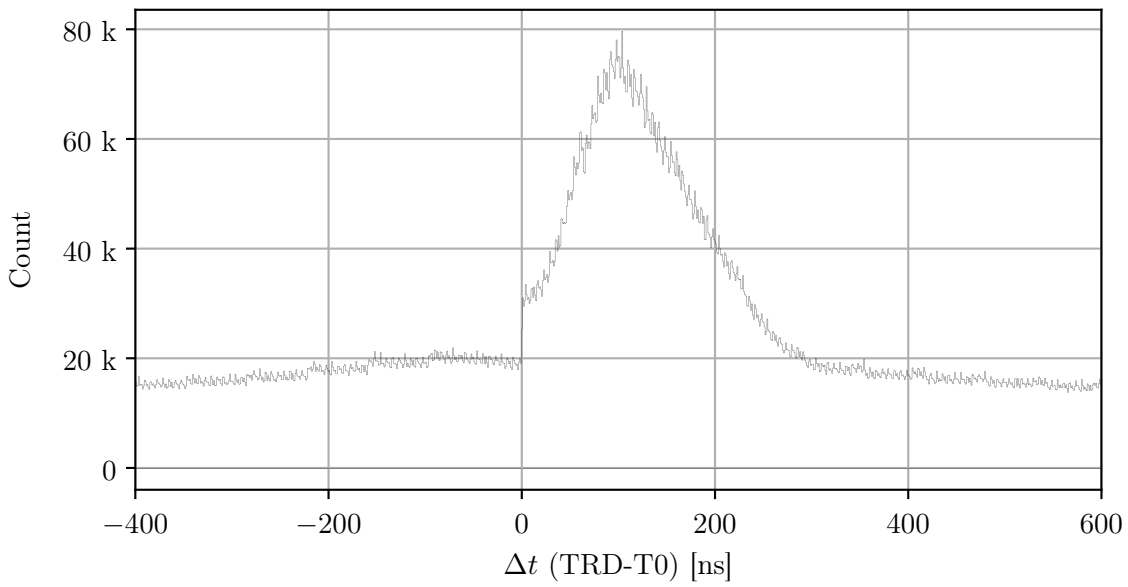

Figure 5.13: TRD hit time differences to the T0 detector.

5.4 Results on Hit Time Correlation

5.4.1 TRD-T0

To test the temporal correlation of TRD with TOF, the TRD hits were correlated in time with the T0 hits in Figure 5.13. T0 hits are again identified by requiring the z-coordinate of TOF hits being below 2 cm. For every T0 hit with time t_{T0}, there is searched in the TRD hit vector for TRD hits with approximately the same time t_{TRD} and when found, an entry in the bin

$$\Delta t = t_{\mathrm{TRD}} - t_{\mathrm{T0}} \tag{5.1}$$

is made. The distribution shows a peak at $\Delta t \approx 100$ ns, which is broadened by the TRD clock cycle of 62.5 ns, while the observed distribution exhibits a width of about 300 ns, which is still to be explained. The time resolution of the TRD digi reconstruction will be improved in the future, which would narrow this peak. The TRD has obviously still an offset towards TOF, as this peak would otherwise be located at $\Delta t = 0$. Another observation is a step at $\Delta t = 0$, which indicates that it is much more unlikely to find a a TRD hit before a T0 hit than the other way around. This can be explained by the eventbuilding, which discards events and the T0 hits inside them when the event is identified as noise, preferring T0 hits which belong to real (not noise) hits. For TRD hits, there is no check if they belong to an event. As the T0 detector with its 50 ps design time resolution is the fastest one and is nearer to the target, in real events it will trigger always faster than TRD. Therefore, it is unlikely to see a T0 hit before TRD, because such a T0 digi would originate from noise and the corresponding event would not fulfill the trigger conditions, leading to the rejection of the contained T0 hits. Therefore, a sharp edge at $\Delta t = 0$ is produced in the hit time correlation, whereas when producing a similar plot on digi level, hence before eventbuilding, this edge is not visible.

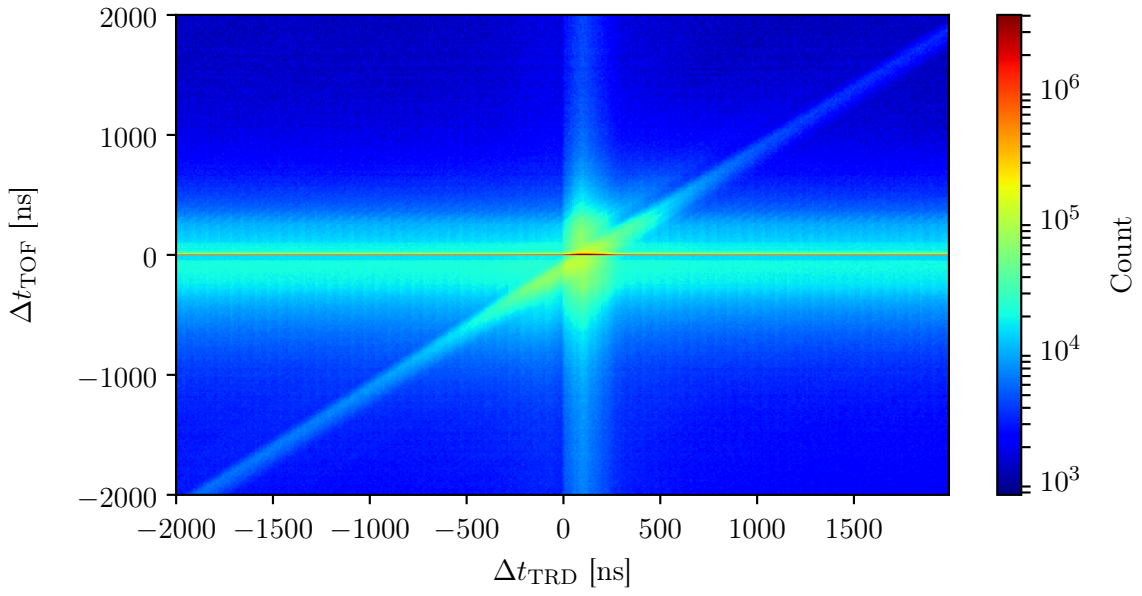

Figure 5.14: All possible combinations of pairs of TRD and TOF hit time differences to the T0 detector within 2000 ns.

5.4.2 TRD-TOF-T0

To also include the TOF stations behind the TRD into the temporal correlation, for each T0 hit, TRD hits which have a maximum time distance of 2000 ns to the T0 hit were taken, and their time distances Δt_{TRD} to the T0 hit were calculated (as in the previous 1-dimensional plot in Figure 5.13). Additionally all TOF hits in the same time window (±2000 ns from T0 hit) were processed and also their temporal distance to T0 Δt_{TOF} was calculated analogue. Then all combinations of values of Δt_{TRD} and Δt_{TOF} were filled in the 2-dimensional plot in Figure 5.14. In this plot, structures are clearly visible: On the one hand, a characteristic angle bisector, which indicates that when a TRD hit was found in a specific temporal distance to a T0 hit, in many cases there was also found a TOF hit in about the same temporal distance, and therefore TRD and TOF are time-correlated. On the other hand, there is also a vertical line with a width up to 300 ns visible, indicating that whenever a TRD hit was found with less than 300 ns temporal distance to T0 there is also randomly found a TOF-hit in the ±2000 ns timewindow in many cases. This represents the temporal resolution of TRD which was also observed in Figure 5.13. For the horizontal line the same explanation holds for TOF relative to T0, with the typical time resolution of TOF. Its intensity is also over one order of magnitude higher than for the vertical TRD-T0-correlation, not only because of the smaller time resolution of TOF, but also because TRD produces over 20 times more hits than TOF. The high multiplicity of TRD compared to TOF could be a result of the event selection applied in the TOF reconstruction, which could be checked by lowering the minimum required digis of TOF and RICH in the event builder at a later point. In conclusion, the three visible lines in the plot show that TRD, T0 and TOF are temporally correlated.

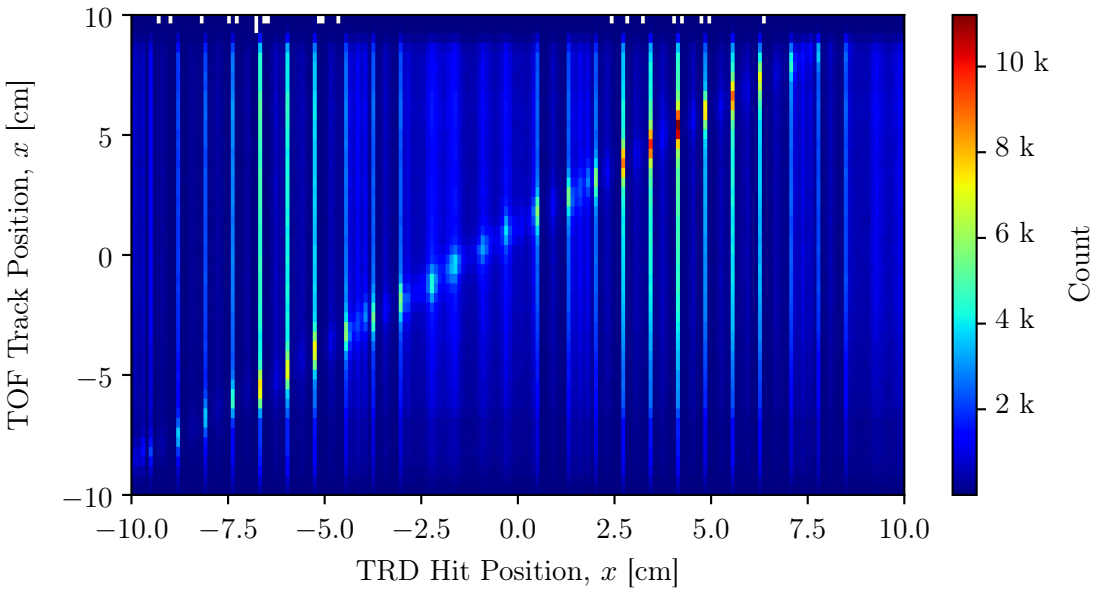

Figure 5.15: Spatial correlation of x-positions of TOF tracks within the TRD acceptance with all TRD hits within a time window of ±400 ns around them. Because of the inhomogenious distribution of the TRD hits, vertical stripes are visible due to the higher hit rate at the corresponding x-positions.

5.5 Results on Spatial Correlation of TRD Hits with TOF Tracks

To proof spatial correlations of TRD and TOF, for each TOF track within the TRD acceptance (e-links 6 to 17 as visible in Figure 5.7) all TRD hits within a time window of ±400 ns are examined and the two x-positions per pair are filled in the plot visible in Figure 5.15. The analysis is limited to the x-positions because one TRD module can only resolve a precise position in one direction. The axis ranges of the histogram from −10 cm to 10 cm are dictated by the distribution of TOF tracks, which are mainly located in this region (see Figure 5.11). An angle bisector is clearly visible, indicating that TRD and TOF are not only temporally but also spatially correlated. There are vertical lines visible which are caused by the inhomogenious distribution of the TRD hits, which was already investigated above. In general, the intensity of the angle bisector enlarges towards higher x-values because the spot of highest intensity is located in this area.

For investigation of the spatial offset between the two detectors, the correlation pairs were also displayed differently in Figure 5.16, which shows the temporal and spatial distances Δt and Δx of the hits and tracks to each other. An accumulation which is slightly displaced to a negative Δx is visible, and for Δt follows the distribution already observed in the temporal correlation of TRD and TOF hits. The displacement in Δx indicates that there is also a spatial offset in this direction, which needs to be corrected. This is done in section 5.6.

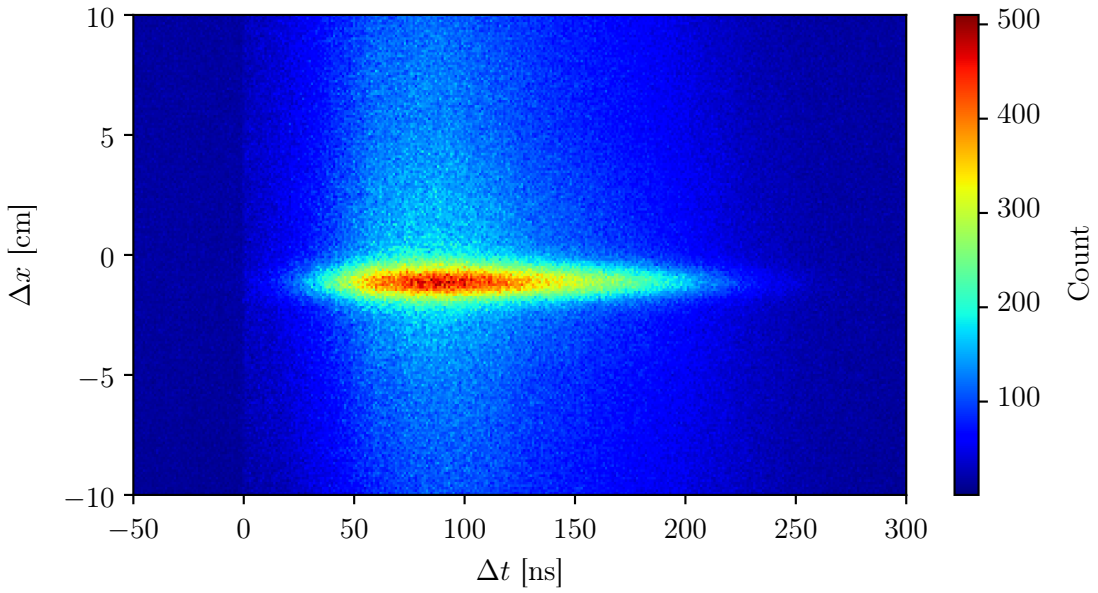

Figure 5.16: Differences in position Δx and time Δt for the TOF tracks and TRD hits within the TRD acceptance.

5.6 Coincidence Analysis

In this chapter, it shall be quantized which fraction of incident particles recognized by TOF is also registered by TRD, and and in particular, the time dependency of this ratio is inspected. Also the spatial distribution of the assignment ratio is of interest. To calculate this ratio, each TOF track has to be matched to a TRD hit which is close in space and time to the track. Thus, a track matching algorithm was developed, which is described in this chapter and whose optimal parameters are estimated here. As the x-coordinate of the TRD hits is of high importance in deciding which hit belongs to which track, an offset correction of the TRD hits is calculated first. In the end, a temporally finer analysis of the assignment ratio over single detector spills is performed and compared to the rate of lost hit messages due to SPADIC buffer overflows.

5.6.1 Offset Correction of TRD Hits

By doing a y-projection of the plot in Figure 5.16 from 0 ns to 250 ns and fitting the resulting peak in Figure 5.17 with a gaussian fit

$$\text{Count}(\Delta x) = a_0 \cdot \exp\left(\frac{(x-\mu)^2}{2\sigma^2}\right) \tag{5.2}$$

in the range ± 0.8 cm around the maximum bin, the x-offset of the TRD hits is found to be $\mu = -1.132$ cm and the track matching resolution is found as $\sigma = 0.774$ cm. The track matching resolution is of the order of a pad width, which is 7.1875 mm, and is higher than the expected space point resolution (around 300 µm) [TDR18]. This can be explained by the low energy resolution of the single digis, resulting from significant fluctuations of the ADC samples recorded by the analogue frontend of SPADIC 2.2 [Coo20]. As the charge of a digi, which is later used as input for the

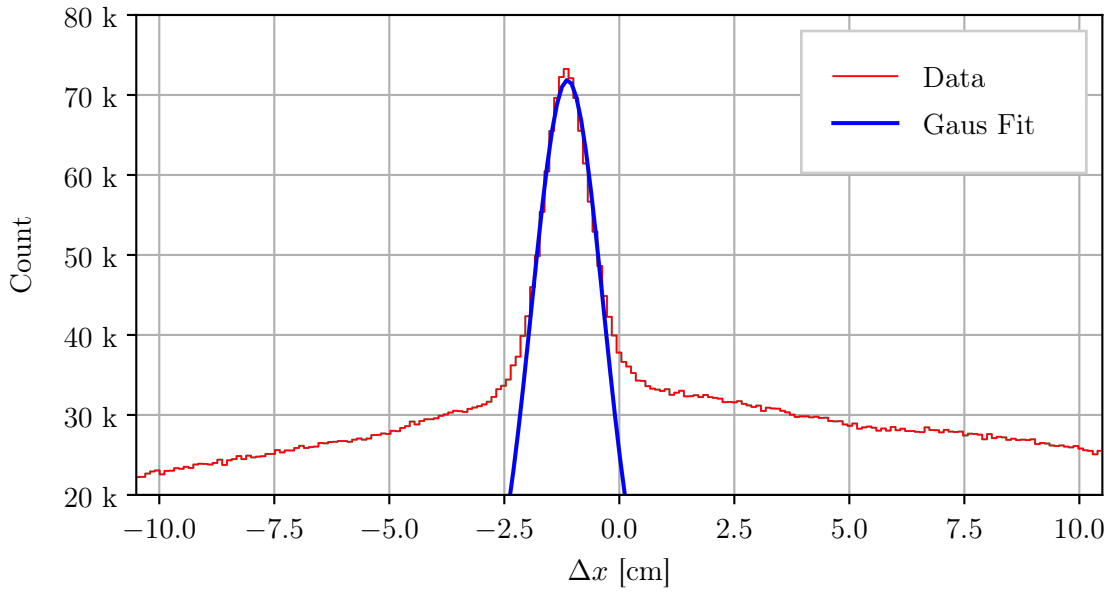

Figure 5.17: Y-projection of Figure 5.16 from 0 ns to 250 ns fitted with a Gaussian function ($\mu = -1.132\,\text{cm}, \sigma = 0.774\,\text{cm}$). σ can be seen as the effective track matching resolution.

COG position reconstruction, is currently determined directly from the maximum ADC value of the incoming signal (raw message), these fluctuations directly affect the quality of the reconstructed position.[1] Additionally, the detector was operated at high gain to compensate against high noise level, which can deteriorate the energy resolution for large charge values by exceeding the linear range. On the overall scale, another explanation is the still missing spatial detector alignment procedure and therefore a geometry information file used in hit reconstruction which has only a rough accuracy. The development of such an alignment process is planned and it is expected that the track matching resolution will improve after implementing this. From physics side, it would be necessary to check the influence from small-angle scattering of the trajectories as well as from the spatial extension of the beam spot on the target.
In the following hit matching process, the offset μ is added to the x-position of the TRD hits.

5.6.2 Matching of TOF Tracks with TRD Hits

To find the best matches of TOF tracks to TRD hits, an algorithm was developed which finds pairs of tracks and hits within a maximum time distance Δt_{max} and a maximum spatial distance Δx_{max}, Δy_{max} at a given z-distance. The procedure works as follows:

1. Calculate x, y and t of the TOF track at the TRD modules z-position.
2. For each TRD hit:
   a) Calculate Δx, Δy and Δt of the TOF track to the TRD hit.
   b) If the condition $\Delta t \leq \Delta t_{\text{max}} \wedge \Delta x \leq \Delta x_{\text{max}} \wedge \Delta y \leq \Delta y_{\text{max}}$ is not met, skip the hit, to ensure a minimum casual relationship.

[1] A new development version of the readout chip, i.e. SPADIC 2.3, has been launched and is currently under investigation. Its aim is to cure the mentioned signal quality issues of the previous chip version.

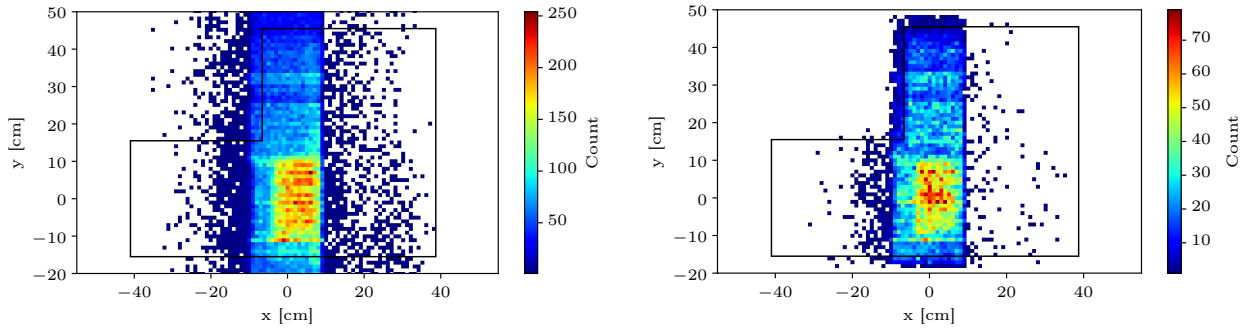

(a) for all TOF tracks

(b) for successfully matched TOF tracks

Figure 5.18: Example spatial distribution of all TOF tracks at the TRD z-position in run 831 (interval 80 s to 100 s). The TRD acceptance is also sketched for orientation.

c) Check if the TRD hit was not already matched to another TOF track by a lookup vector.

d) Calculate $d = \sqrt{\Delta x^2 + \Delta t^2}$, and if no other hit was determined as matching candidate yet or d for the current matching candidate is larger, use this hit as the (new) matching candidate.

3. The hit which remains as the matching candidate (if one exists) is now matched to the TOF track and gets saved in the lookup vector as already matched.

For the parameters of the algorithm a parameter variation was done to find the best assignment ratio (see subsection 5.6.6) of TRD hits to TOF tracks. The resulting final values are $\Delta t_{\max} = 250\,\text{ns}$, $\Delta x_{\max} = 4\,\text{cm}$ and $\Delta y_{\max} = 10\,\text{cm}$. The algorithm is applied to all TOF tracks and TRD hits within a timeslice and for each 20 s interval of the run the spatial distribution of TOF tracks for which a matching TRD hit was found is plotted. An example and also a comparison to the total amount of TOF tracks in the same 20 s interval is shown in Figure 5.18. By dividing the histogram for the matched amount of TOF tracks Figure 5.18b binwise through the histogram for the total amount of TOF tracks Figure 5.18a, the spatial ratio of TOF tracks which were also recognized in TRD can be calculated, which is shown exemplarily in Figure 5.19. For the other 20 s intervals the distribution looks similar and shows that especially in the high intensity area the assignment ratio is decreased in comparison to the outer regions, in which the intensity is lower and the assignment ratio reaches 50 %. In regions where only few TOF tracks are present but which lie inside the TRD acceptance, the assignment ratio increases artificially to 100 %, because the probability to find a TRD hit for a TOF track is very high due to the very different multiplicities.
Another aspect to mention is that for points outside but near the TRD acceptance border the assignment ratio is not always zero. This is possible because of the liberally selected parameters $\Delta x_{\max}$ and $\Delta y_{\max}$ for the track matching algorithm, thereby by random coincidences.

5.6.3 Reference Area

To measure and display the assignment ratio over the whole run time, a reference area is defined for which the average assignment ratio is calculated. The area lies within the common TRD and

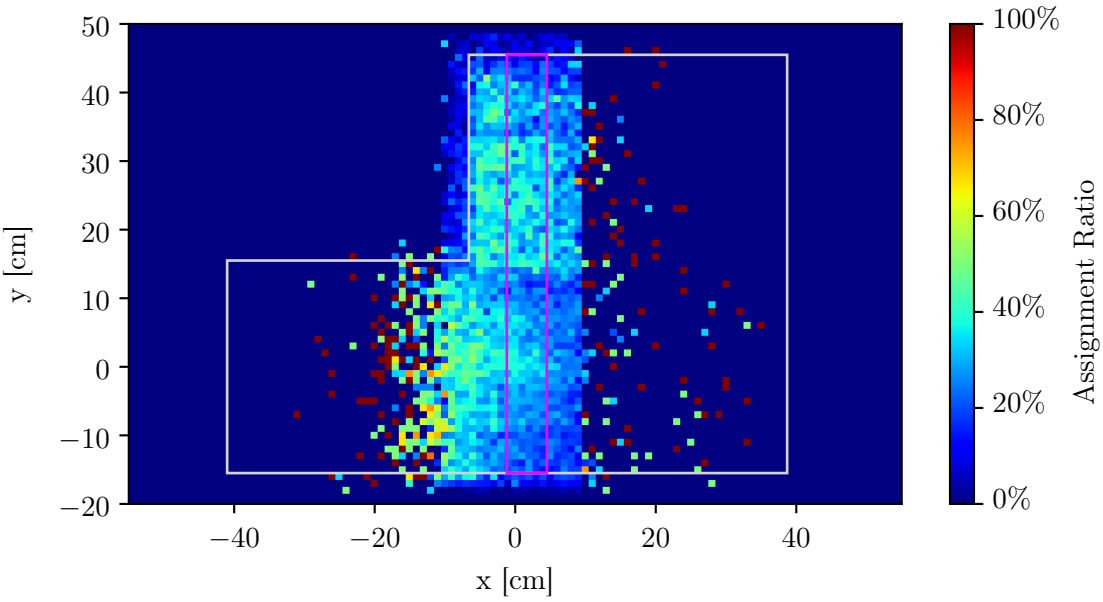

Figure 5.19: Assignment ratio for TOF tracks in TRD in run 831 (interval 80 s to 100 s). In light gray, the TRD acceptance is also sketched for orientation. In magenta, the reference area, which covers exactly the e-links 7 and 27, is marked.

TOF acceptance and covers exactly the areas of the TRD e-links 7 and 21. In Figure 5.19 the area is marked in purple. For a position which is recognized to be inside the reference area, the following conditions must be met:

$$-1.2\,\text{cm} \leq x \leq 4.5\,\text{cm} \wedge -15.5\,\text{cm} \leq y \leq 45.5\,\text{cm} \tag{5.3}$$

By integrating over this area and dividing it by the surface area of the rectangle, a single number – the so-called reference assignment ratio – describing the TRD performance in the specific 20 s interval is produced.

5.6.4 Reference Assignment Ratio Evolution over Run Time

The evolution of the reference assignment ratio over the whole run 831 is plotted in Figure 5.20. The reference assignment ratio fluctuates between 24.8 % and 37.6 % and is on average on a level of (29 ± 5) %. From 460 s to 500 s the assignment ratio is with more than 35 % on the highest level. When compared to the TRD hit rate in the reference area in Figure 5.21, it is visible that in these two 20 s intervals a SIS18 spill is located which has extraordinary low intensity. This indicates a rate dependency of the assignment ratio, with a better efficiency for the lower rate.
Additionally it was tested to only use the areas inside the TRD acceptance which are covered by channels which neightbor triggers are correctly configured according to Figure 3.9 instead of using the full reference area, but this did not lead to significant changes in the plot. This is no surprise, as the TRD hit producer does not require a minimum cluster size to produce hits out of them and therefore the incorrectly configured pads still produce hits, although out of mostly one-pad clusters they are expected to exhibit a lower position resolution. In the configured large spatial correlation

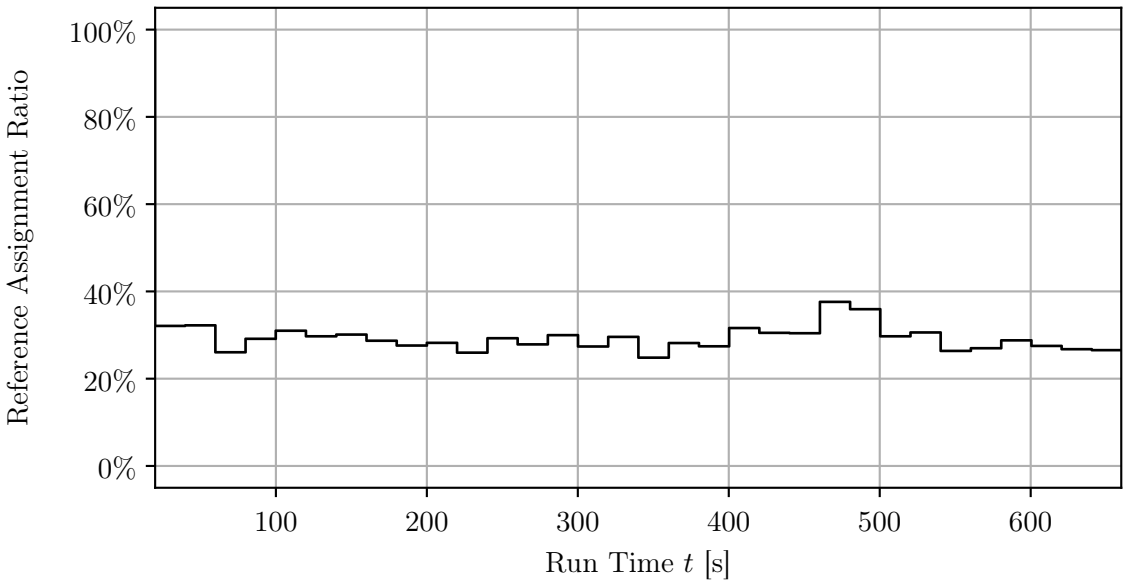

Figure 5.20: Evolution of the average assignment ratio in the reference area over the whole run 831.

window of a track and hit in the algorithm, the matching is also possible in this regions.

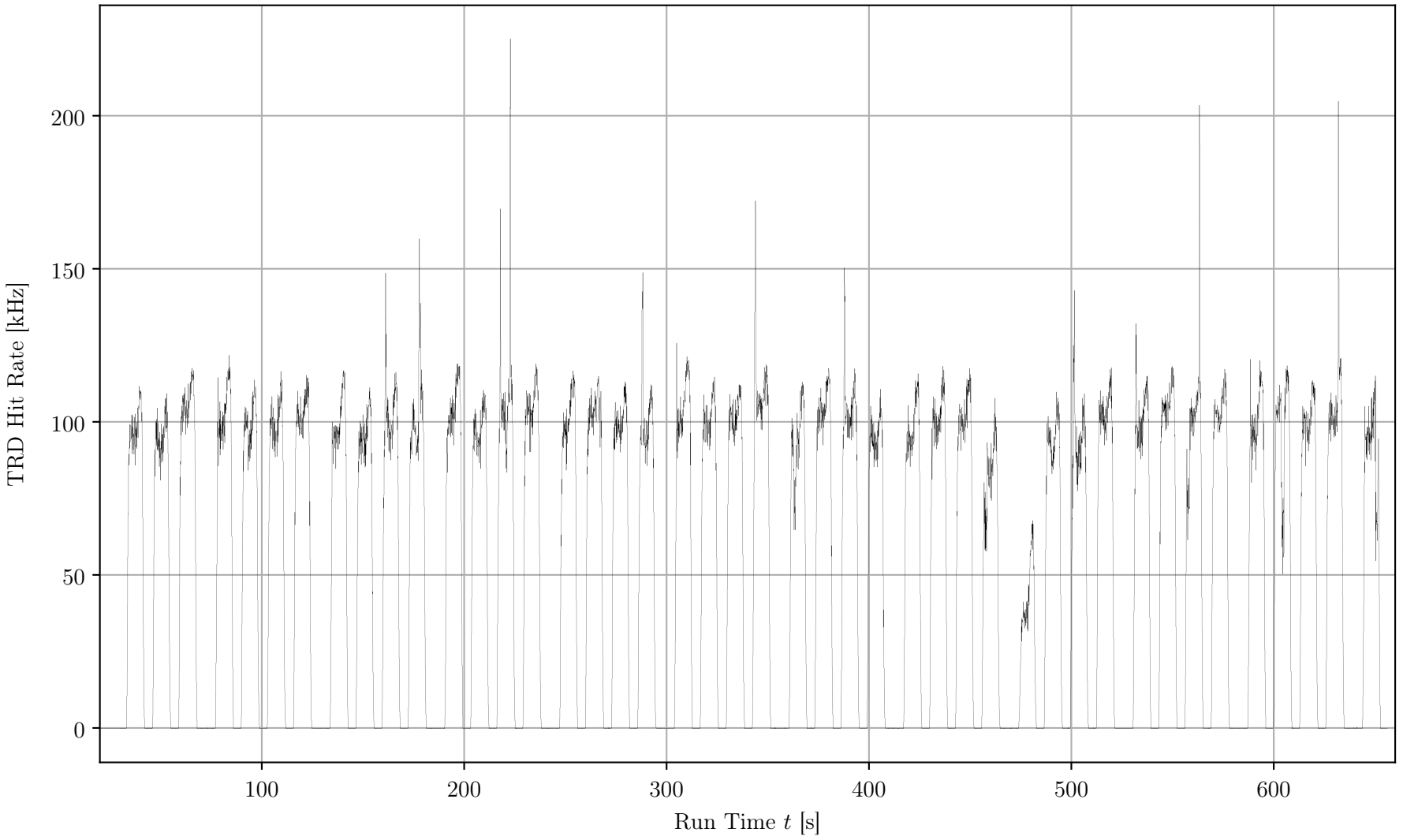

Figure 5.21: Hit rate for TRD in the reference area over run 831. The spill length and structure of the SIS18 is complicated and different for every spill.

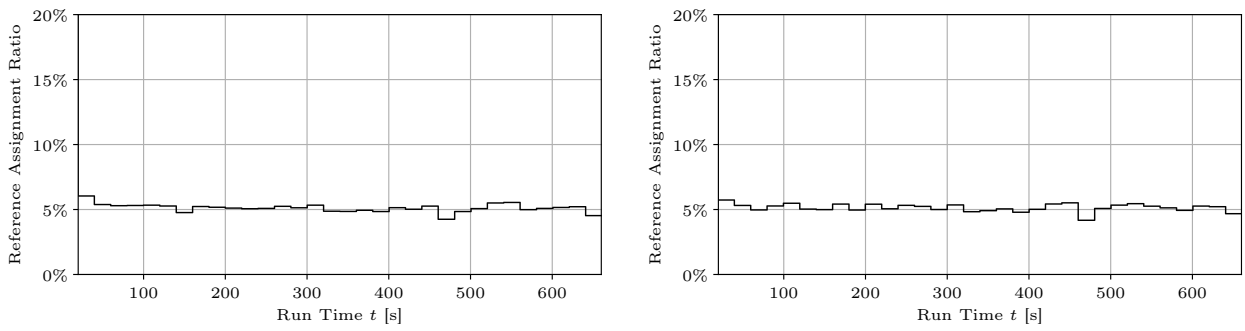

(a) for 1000 ns shift

(b) for 1500 ns shift

Figure 5.22: Reference assignment ratio over run 831 with the TRD hits shifted to test the random coincidences.

5.6.5 Random Coincidences

To proof that the track and hit matching process is not dominated by chance or noise, and thereby to identify the real coincidences better, the same analysis was done with all TRD hits shifted into the future by 1000 ns and 1500 ns. Those values are clearly above the maximum time distance of $\Delta t_{\max} = 250\,\text{ns}$ allowed in the matching algorithm but still magnitudes below the timeslice length of 12 800 µs, so it is still sufficient to only correlate hits and tracks saved within the same timeslice container. The results show a similar constant value which does not exceed a reference assignment ratio of 6.1 %. This assignment ratios are identified here with random coincidences. This shows that in Figure 5.20 there is always a significant amount of real coincidences of tracks and hits, because here the average assignment ratio is four to five times as high (29 %).

5.6.6 Parameter Variation of Maximum Distances used in the Matching Algorithm

To investigate the influence of the maximum x-, y- and t-distance in the track and hit matching on the assignment ratio, parameter variations were performed for each of the three parameters. When one parameter is varied, the other two are fixed to the values used in the final analysis ($\Delta t_{\max} = 250\,\text{ns}$, $\Delta x_{\max} = 4\,\text{cm}$, $\Delta y_{\max} = 10\,\text{cm}$). For each set of parameters, the full assignment analysis described above (except the check for random coincidences) is executed again and the time average of the reference assignment ratio over the whole run 831 is plotted against the varied parameter value. For the maximum time distances $\Delta t_{\max}$ between matched hits and tracks the variation is performed in steps of 30 ns and the result is shown in Figure 5.23. The reference assignment ratio rises with linear behavior, while the slope changes at about $\Delta t_{\max} = 220\,\text{ns}$, as it gets more likely to find a match to a track when the search time interval is larger and additional hits are added. It is assumed that the first slope results from real coincidences, as in this area also the most entries in the temporal and spatial correlation are located in Figure 5.16, while for the second slope noise is suspected to be the origin. As this is only a maximum time distance in the algorithm and the x-t-distance is still minimized, a final value of $\Delta t_{\max} = 250\,\text{ns}$ was selected for the algorithm parameter. With this liberal value, a large assignment ratio is expected.

For the maximum y-distances $\Delta y_{\max}$ the variation is done the same way in steps of 1 cm and

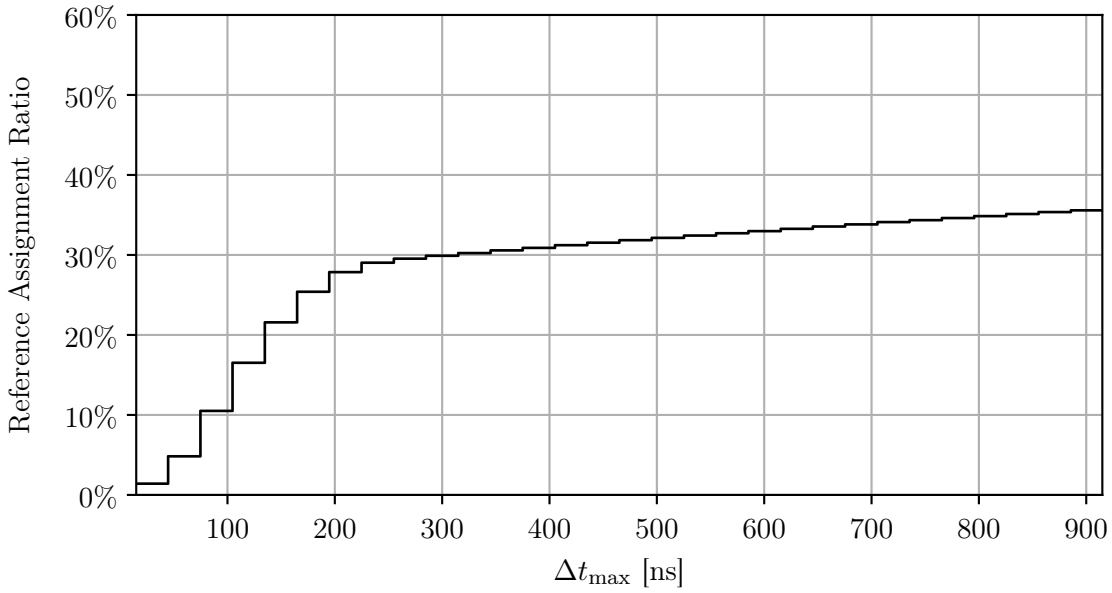

Figure 5.23: Assignment ratio in the reference area for different maximum time distances $\Delta t_{\max}$ between matched hits and tracks, while the other two parameters are fixed to their final values ($\Delta x_{\max} = 4\,\text{cm}$, $\Delta y_{\max} = 10\,\text{cm}$).

the result is shown in Figure 5.24. A similar pattern as in the variation for the maximum time distance is visible there. The assignment ratio rises with increasing maximum distance, and again two different slopes can be identified. The slope changes at $\Delta y_{\max} \approx 9\,\text{cm}$, and again it is assumed that beyond this value any further increase of the assignment ratio is originated by noise. The height of one pad is 15 cm, which is in a similar order of magnitude. Assumed that the TOF tracks have zero measurement uncertainty and the geometry used for reconstructing the positions is perfectly determined, it would be possible to have a y-displacement of half a TRD pad height (7.5 cm) between a TOF track and TRD hit originating from the same particle, while the real displacement is assumed to be larger. To cover all real coincidences, the final value for the maximum y-distance was set to $\Delta y_{\max} = 10\,\text{cm}$.
Also for the maximum x-distance the variation was done and the result it shown in Figure 5.25. In comparison to the other two variations, the change in the linear slope is less strict. At least until $\Delta x_{\max} \approx 3\,\text{cm}$, a linear increase is visible. The track matching resolution was previously found to $\sigma = 0.774\,\text{cm}$ (see Figure 5.17), which makes the still strong increase in hit assignment beyond this value surprising, and the mechanism behind this is not explained here. For the algorithm, a maximum distance of $\Delta x_{\max} = 4\,\text{cm}$ was finally selected.

5.6.7 Finer Resolution of Assignment Ratio over Single Spills

As the temporal investigation of the assignment ratio was done in intervals of 20 s to ensure sufficient statistics for the spatial distribution of the assignment ratio within one interval, additionally a plot which lacks of any spatial differentiation but has a finer time resolution of 100 ms was produced. In Figure 5.26, the resulting assignment ratio in the reference area is plotted. The diagram reveals strong fluctuations inside the SIS18 spills, and for short regions at the spill borders the assignment

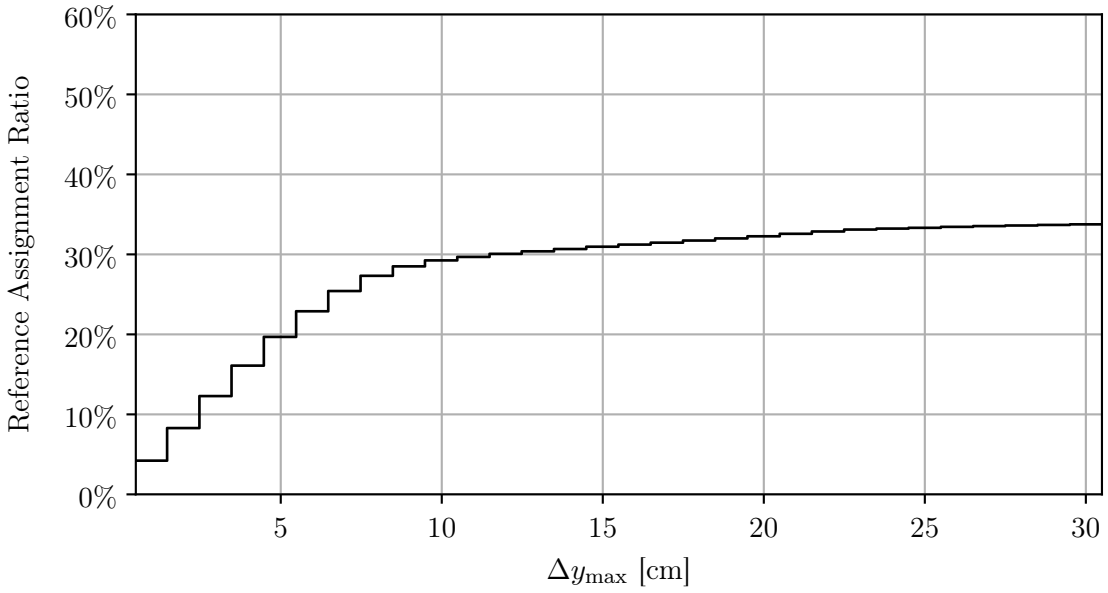

Figure 5.24: Assignment ratio in the reference area for different maximum y-distances $\Delta y_{\max}$ between matched hits and tracks, while the other two parameters are fixed to their final values ($\Delta x_{\max} = 4\,\text{cm}$, $\Delta t_{\max} = 250\,\text{ns}$).

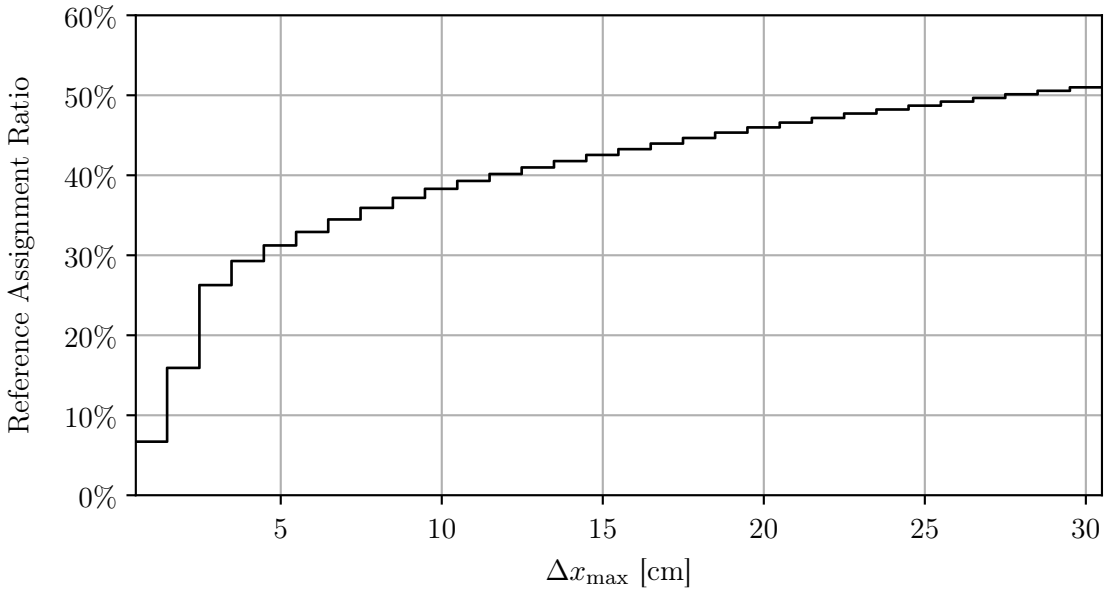

Figure 5.25: Assignment ratio in the reference area for different maximum x-distances $\Delta x_{\max}$ between matched hits and tracks, while the other two parameters are fixed to their final values ($\Delta y_{\max} = 10\,\text{cm}$, $\Delta t_{\max} = 250\,\text{ns}$).

ratio reaches 100 %. The spill at 480 s with lower intensity (see Figure 5.21) stands out with an overall higher assignment ratio again. A closer look at single spills is taken in Figure 5.27. Here the assignment ratio is also compared with the rates of TOF tracks and TRD hits which occurred in the reference area. It is visible that there are much more TRD hits than TOF tracks recognized. The SIS18 spills have a slightly lowered intensity in the middle, which increases the reference assignment ratio. This connection is interpreted as rate dependency again. This is also supported by the observation that the assignment ratio is significantly higher at the beginning and end of each spill, where the track and hit rate start to rise respectively fall and are lower than in the rest of the spill. Because the TRD was operated at very high rates in this beamtime, partially exceeding design rates of the readout electronics, this behavior is no surprise.
At $t = 98.8\,\mathrm{s}$, the assignment ratio drops to zero and increases afterwards again for the rest of the spill. This could be a time jump in the TRD data which was too short to be registered and therefore remained uncorrected. Such artifacts are also visible in other spills not shown here. In the time regions where time jumps were registered and corrected, there are also drops in the assignment ratio visible, although not to zero, because the accuracy of the time jump point is in the order of the correlation window (3 s), but the resolution of this plot is much higher.

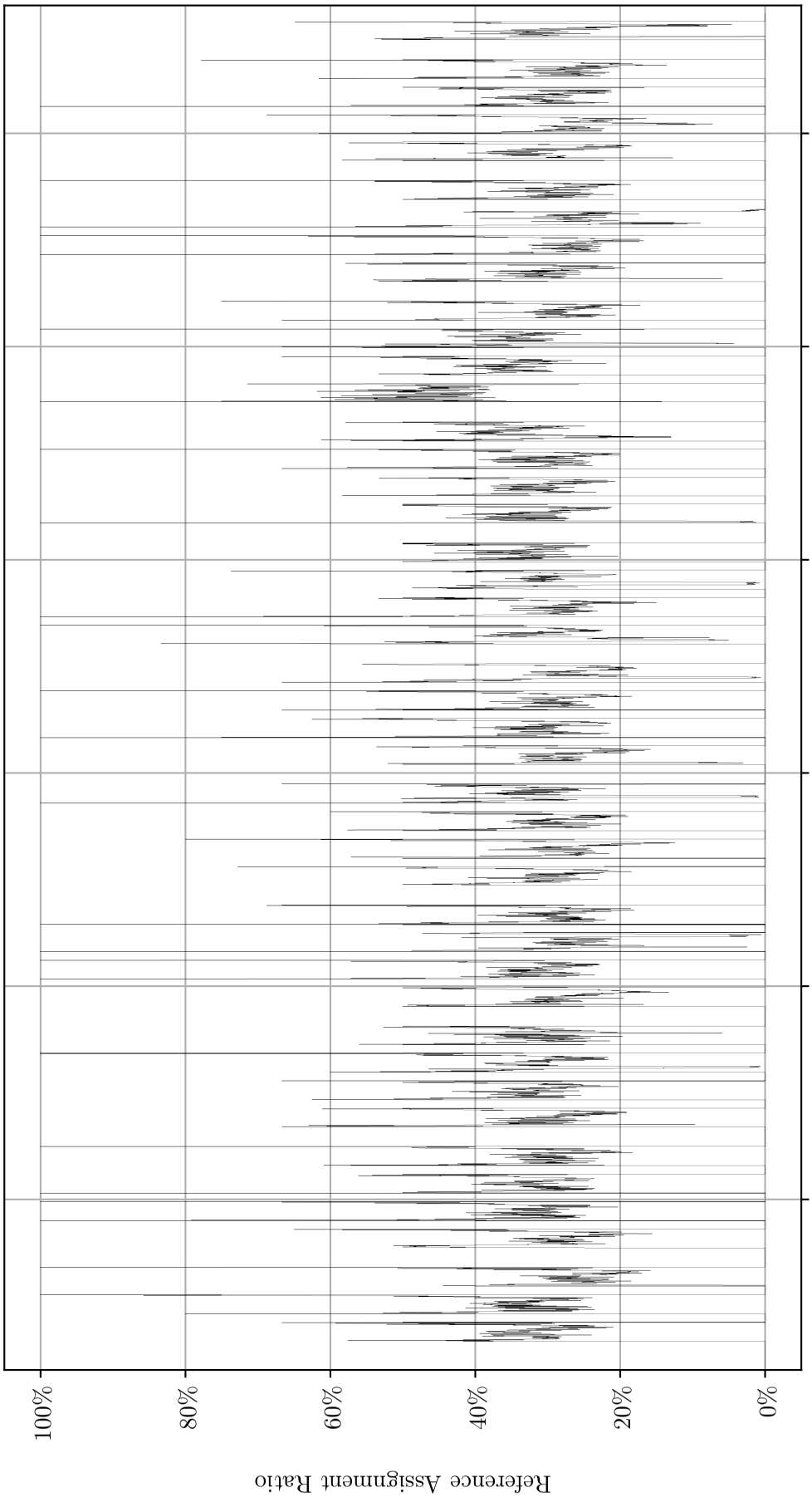

Figure 5.26: Evolution of the reference assignment ratio over run 831 with higher time resolution.

5.6.8 Lost TRD Messages due to Buffer Overflows

If a SPADIC channel gets triggered but its buffers (channel buffer or the ordering FIFO buffer of its group) are already full due to too much load, an internal counter in the chip for this channel is incremented. When the buffers are transmitted to the DAQ and the channel can send data again, a buffer overflow message (BOM) is generated, which contains the group ID, channel ID, a timestamp carrying the time of the last trigger and the 14 bit value of the lost message counter h_l for this channel [Spa]. In Figure 5.28, the rate of those messages within the reference area is displayed together with the reference assignment ratio. As the incrementation counter values were not reliable (see below) the BOM rate is not weighted with the lost message counter value. Also the BOM timestamp is not used, as the timejump correction was not applied to the SPADIC info messages which contain the BOM messages. Instead the start time of the timeslice the message is stored in is used here, as the time slice length of 12.8 ms still complies with the bin width of this histogram, which is 100 ms.
In the plot it is visible that the BOM rate is anticorrelated to the reference assignment ratio. When the BOM rate rises, the reference assignment ratio drops and vice versa. At the beginnings and ends of the spills there is a short time where no BOM messages are received. Simultaneously the reference assignment ratio is at its highest level. This is another hint that the assignment ratio of TRD depends on the hit rate on the padplane. It is reminded here, that the pad size of the TRD chamber was originally designed for the outermost TRD region, i.e. for very low rates. By this, the hit rate per readout channel is increased.
A problem which occured while looking at the buffer overflow messages was that the lost hits counter was unexpectedly high. Some messages have lost hits counters of over 1000, while in simulations at the chip designing facility ZITI Heidelberg at rates of 1.7 MHz per channel the maximum amount the counter reached was 11. Looking at the lost hit values of single BOMs revealed that messages on the same channel often have a difference which is an integral multiple of 16. In Figure 5.29 for each channels consecutive BOMs the difference of their lost hit counters is calculated and plotted. There is a clear pattern visible which has strong accumulations at Δl_h being integral multiples of 16. There are no sharply peaking bins but the likelihood to find a consecutive message pair with a specific Δl_h continuously increases near integral multiples of 16. If there would be only a single bin which stands out it would be a good explanation that the last 4 bits representing the lost hit counter are for example always set to zero, which would always give numbers which are a multiple of 16, but this would not explain the continuous rise around those numbers. It was also cross-checked with the ZITI that the code to extract the lost hit counts bitwise from the BOM is correct. This behavior thereby remains unexplained here.

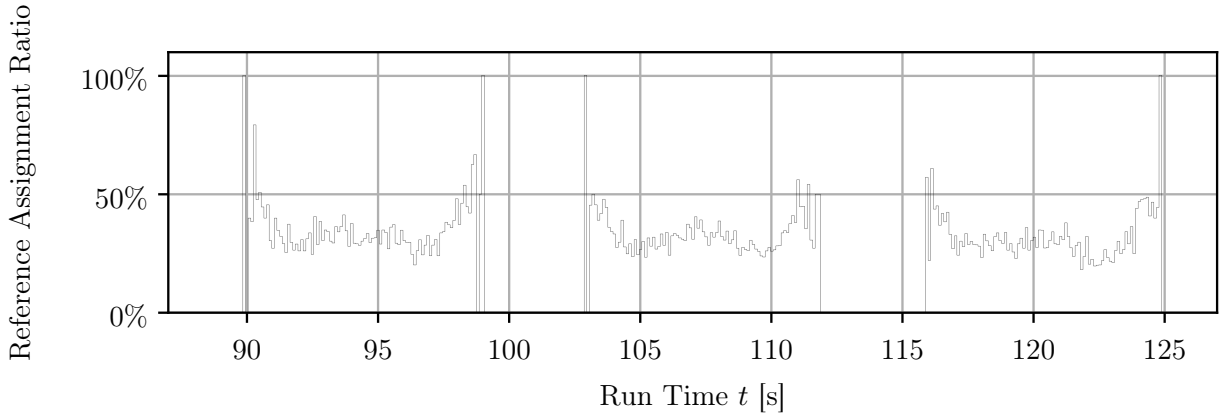

(a) Evolution of the reference assignment ratio over three single spills.

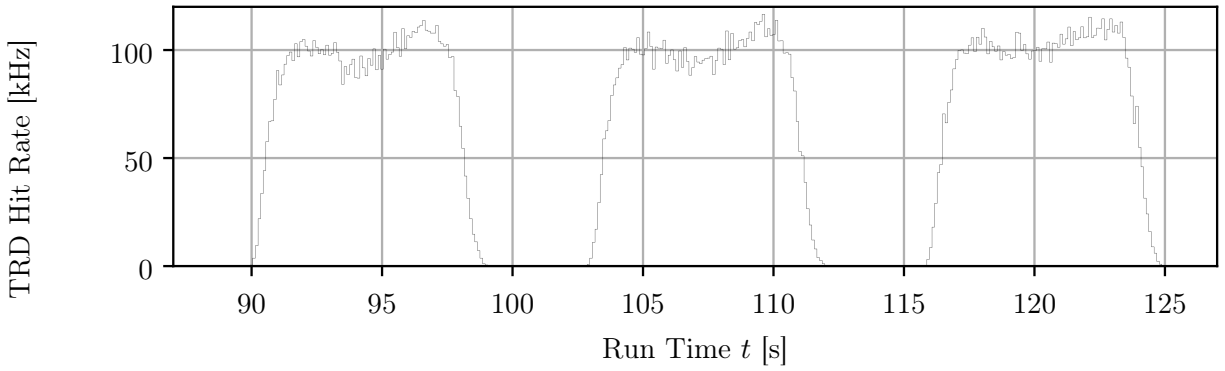

(b) Evolution of the TRD hit rate in the reference area over three single spills.

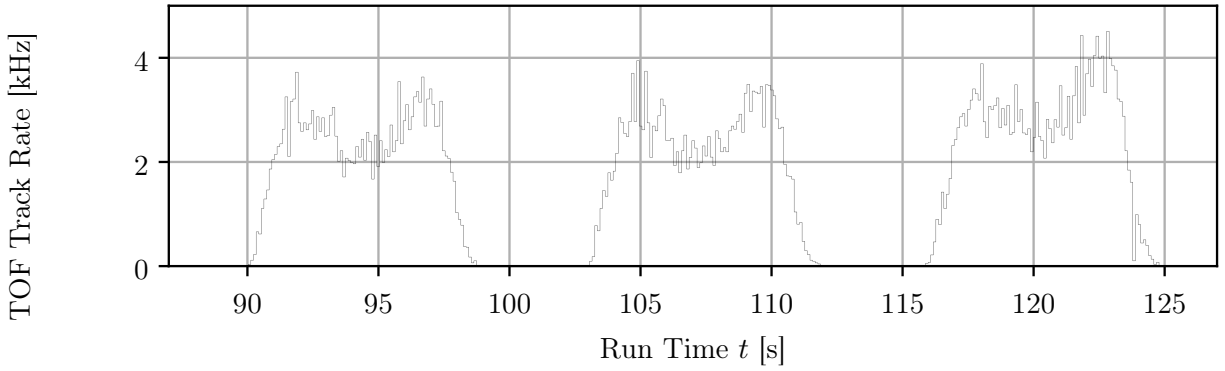

(c) Evolution of the TOF track rate in the reference area over three single spills.

Figure 5.27: Comparison of the reference assignment ratio over three single spills with the corresponding rates of TOF tracks and TRD hits in the same area.

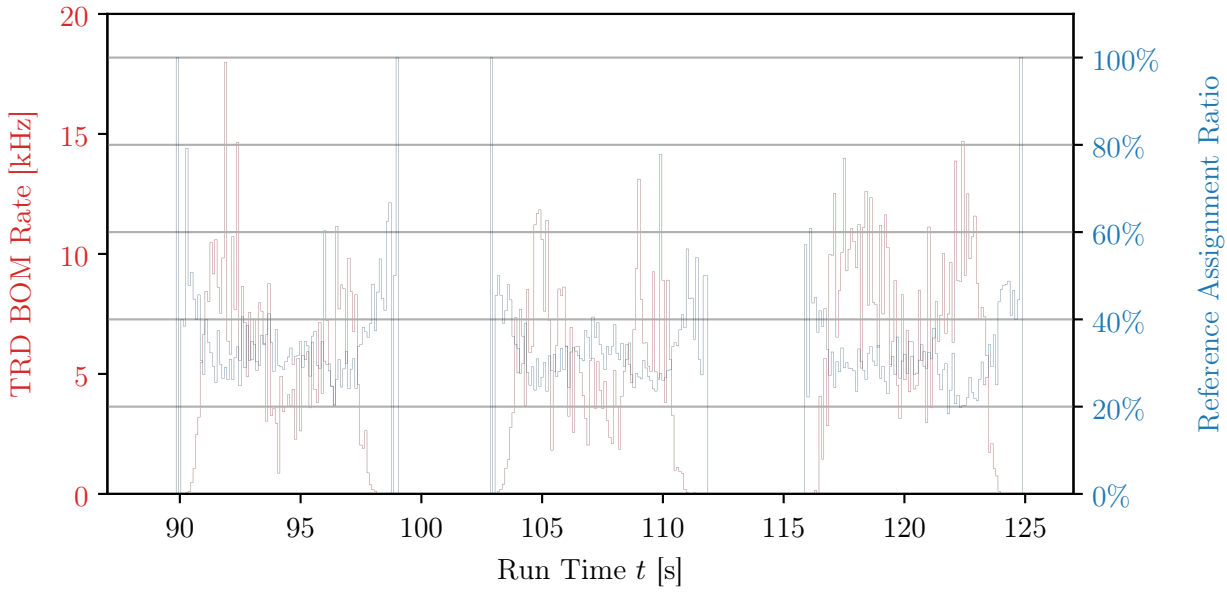

Figure 5.28: Rate of TRD Buffer Overflow Messages (BOM) over three spills.

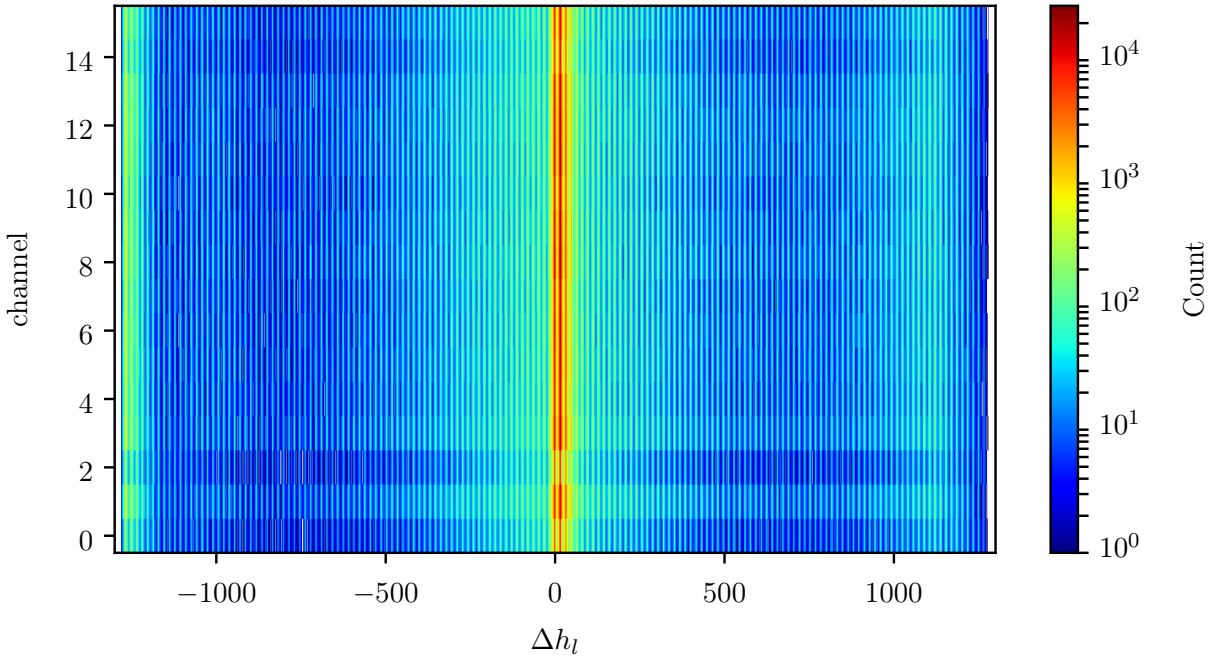

(a) The pattern spans over the whole distribution.

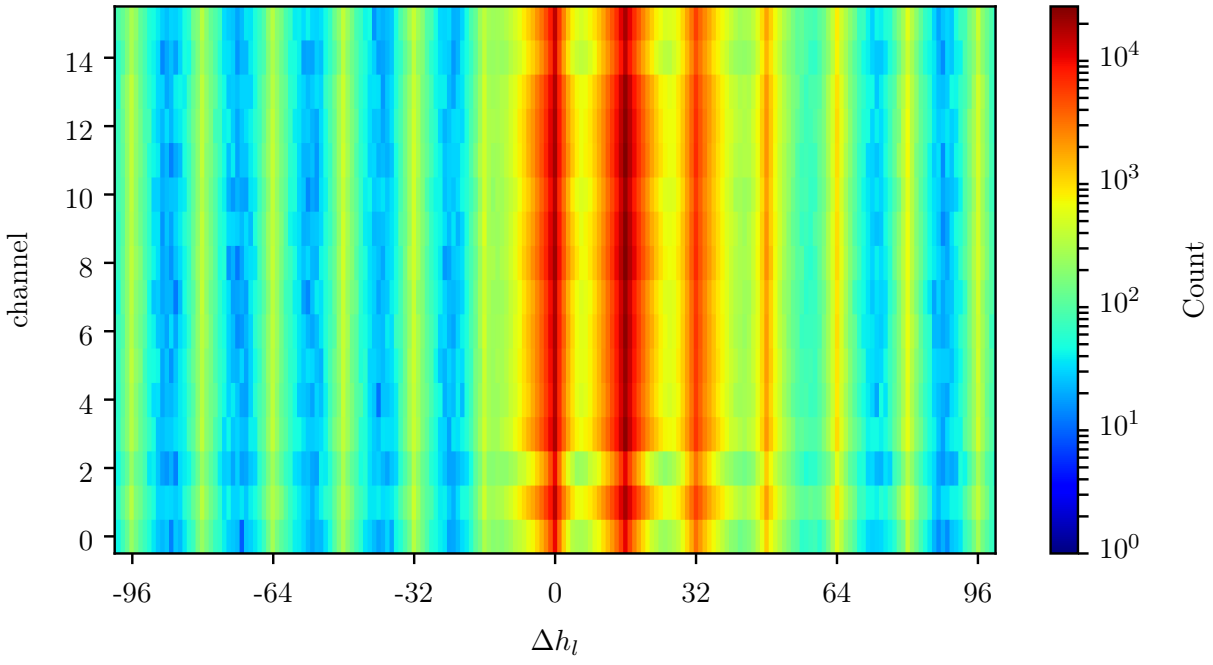

(b) The accumulations always occur on Δl_h which are multiples of 16.

Figure 5.29: For each channel of e-link 10, the difference of the lost hit counters Δh_l of consecutive buffer overflow messages is calculated and inserted into a histogram, which reveals a pattern.

6 Conclusion and Outlook

As part of this master thesis, correlations of the Transition Radiation Detector in the FAIR Phase-0 program both temporally and spatially to another subsystem, i.e. the TOF detector, were successfully demonstrated for the first time. On the way to this result, the characteristics of the data set from the mCBM 2020 campaign were worked out in detail. Specifically, the effects of an incomplete trigger propagation to neighbored detector pads on the charge cluster analysis of TRD hits were traced in section 5.2. Furthermore, the effects of the event building process on the distribution of event lengths, the number of digis of the various subsystems within the events and the effects of the event selection on the temporal correlation of TRD and TOF were discussed on the basis of the results in section 5.1 and section 5.4. During the first analysis attempts it was found that the TRD raw data stream exhibits discrete jumps of the timing relative to the general experiment clock, occurring individually for the readout links ("e-links") of the subdetector. Their properties were characterized in chapter 4 and a correction procedure was developed within the scope of this work and has been proven to work with a good efficiency. Recognition and description of this error led to stabilization of the readout in later firmware versions of the TRD readout chain.
In addition, a spatial correlation analysis was developed in section 5.6, in which matching TRD hits are assigned to given TOF tracks at a defined maximum temporal and spatial distance. A parameter variation of the matching algorithm was performed to find appropriate parameters for the algorithm. The matching was spatially visualized and examined for its assignment ratio within the common detector acceptance. In addition, the development of the assignment ratio within a selected reference area over time was tested for two different time granularities. Indications of a rate dependence of this value were found. For individual SIS18 spills, the high-granularity reference assignment ratio was also compared to the TRD hit rate. A rate dependency was again found here. In this course, also output of the rate overflow mechanisms of the readout chip have been investigated. Currently not understood behavior was reported to the chip development and chip simulations by the involved developers were triggered by this reporting. Suggested for further investigation can be high-rate readout tests with a pulse generator in the laboratory, in particular with irregular timing intervals between the signals.
During the analysis of the events and the temporal correlations it became apparent that the temporal resolution of the TRD digi times is still roughly compared to other subsystems. This behavior is expected, as the currently implemented algorithm is based on time stamps of the TRD readout only, while a more advanced hit reconstruction derives a finer timing from the recorded raw signal. A more precise time resolution would also be advantageous for the track hit matching algorithm and make the assignment much easier. Such algorithms are already available and used in tests with simulated data, while the test on real data is pending. Implementing this in the unpacker and testing it with real data would be a further step to significantly increase the quality and value of the data.

Furthermore, a track matching resolution clearly above the TRD design space point resolution was found, which is discussed in detail in subsection 5.6.1. As a further step, besides the improvement of the SPADICs sample-to-sample fluctuations, the development of a sophisticated alignment method within the entire mCBM experiment for all subsystems is required here. For this purpose, an improved time resolution of the TRD hit reconstruction algorithm would also be beneficial. With an improved geometry, the spatial resolution of the TRD should then be better able to be examined. In addition, it would then be possible to define stricter maximum distances between TRD hits matched to a TOF track, and thus to increase the quality and value of the coincidence analysis.
Another interesting question is to which level the assignment ratio can be increased in runs where the beam intensity is lower and less to none buffer overflows in the SPADIC occur.

Bibliography

[Arm13] Tim Armbruster. "SPADIC - a Self-Triggered Detector Readout ASIC with Multi-Channel Amplification and Digitization." dissertation. Ruperto-Carola University of Heidelberg, 2013. URL: http://archiv.ub.uni-heidelberg.de/volltextserver/14981/1/Thesis_Armbruster.pdf.

[AW11] A. Andronic and J. P. Wessels. *Transition Radiation Detectors*. 2011. arXiv: 1111.4188.

[Bay+18] Gordon Baym et al. "From hadrons to quarks in neutron stars: a review." In: *Reports on Progress in Physics* 81.5 (2018), p. 056902. DOI: 10.1088/1361-6633/aaae14.

[Ca16] CBM Collaboration and T. Ablyazimov et al. *Challenges in QCD matter physics - The Compressed Baryonic Matter experiment at FAIR*. 2016. arXiv: 1607.01487.

[Cbm] *Sketch of the CBM cave*. URL: https://www.cbm.gsi.de/sites/default/files/inline-images/CBMcave_picture_0.png.

[Col13] The CBM Collaboration. *Technical Design Report for the CBM Silicon Tracking System (STS)*. Tech. rep. Facility for Antiproton and Ion Research in Europe GmbH Darmstadt, Oct. 2013.

[Col14] The CBM Collaboration. *Technical Design Report for the CBM Muon Chambers (MuCh)*. Tech. rep. Facility for Antiproton and Ion Research in Europe GmbH Darmstadt, Nov. 2014.

[Col17] The CBM Collaboration. *Beamtime Application CBM@SIS18. A CBM full system test-setup for high-rate nucleus-nucleus collisions at GSI / FAIR*. June 2017. URL: https://fair-center.de/fileadmin/fair/experiments/CBM/documents/mcbm-proposal2GPAC-WebVersion0619-SVN7729.pdf.

[Coo20] CBM-TRD Technical Coordination. *Status: signal quality (internal report)*. 2020.

[ESS05] Volker Eckardt, Norbert Schmitz, and Peter Seyboth. "Auf der Spur des künstlichen Urknalls: Anzeichen für Quark-Gluon-Materie im Labor." In: *Physik in unserer Zeit* 36.3 (Apr. 2005), pp. 126–134. DOI: 10.1002/piuz.200501071.

[FAI17] FAIR_GSI_de. *Twitter post*. 2017. URL: https://twitter.com/fair_gsi_de/status/886125178496835585 (visited on 04/23/2021).

[Fid20] Felix Fidorra. "Construction of a Gas System for the CBM-TRD Prototypes and Analysis of CBM-TRD Test Beam Data Towards Position Reconstruction." MA thesis. Westfälische Wilhelms-Universität Münster, Aug. 2020. URL: https://www.uni-muenster.de/imperia/md/content/physik_kp/fidorra2020.pdf.

[Fri+11] B. Friman et al. *The CBM Physics Book*. Compressed Baryonic Matter in Laboratory Experiments. Springer, 2011. ISBN: 978-3-642-13293-3.

[Gut+06] H. H. Gutbrod et al. *FAIR Baseline Technical Report. Executive Summary*. Tech. rep. Sept. 2006.

[HCL17] Dirk Hutter, Jan de Cuveland, and Volker Lindenstruth. "CBM First-level Event Selector Input Interface Demonstrator." In: *Journal of Physics: Conference Series* 898 (Oct. 2017), p. 032047. DOI: 10.1088/1742-6596/898/3/032047.

[KB09] Melanie Klein-Bösing. "Development of a Transition Radiation Detector and Reconstruction of Photon Conversions in the CBM Experiment." dissertation. Westfälische Wilhelms-Universität Münster, 2009. URL: https://www.uni-muenster.de/imperia/md/content/physik_kp/agwessels/thesis_db/ag_wessels/klein-boesing_m_2009_dissertation.pdf.

[KM14] K. Kawagoe and M. Mulders. "Proceedings of the 1st Asia-Europe-Pacific School of High-Energy Physics (AEPSHEP 12), Fukuoka, Japan, 14 - 27 Oct 2012." In: (2014). DOI: 10.5170/CERN-2014-001.

[KMA20] Philipp Kähler and Adrian Meyer-Ahrens. private communication. 2020.

[Koc97] Volker Koch. "Aspects of Chiral Symmetry." In: *International Journal of Modern Physics E* 06.02 (June 1997), pp. 203–249. arXiv: nucl-th/9706075.

[KW16] Hermann Kolanoski and Norbert Wermes. *Teilchendetektoren: Grundlagen und Anwendungen*. Springer, 2016. ISBN: 978-3-662-45349-0. DOI: 10.1007/978-3-662-45350-6.

[Kä20] Philipp Kähler. private communication. 2020.

[Leo87] W.R. Leo. *Techniques for nuclear and particle Physics experiments*. Berlin and Heidelberg: Springer, 1987. ISBN: 3-540-17386-2. DOI: 10.1016/0168-583X(88)90756-2.

[PDG18] M. Tanabashi et al. (Particle Data Group). "Review of Particle Physics." In: *Physical Review D* 98 (Aug. 2018). DOI: 10.1103/PhysRevD.98.030001.

[Sen20] Peter Senger. "Astrophysics in the Laboratory—The CBM Experiment at FAIR." In: *Particles* 3.2 (2020), pp. 320–335. ISSN: 2571-712X. DOI: 10.3390/particles3020024.

[Spa] *SPADIC 1.0 Data Sheet*. Version 0.30. Institut für Technische Informatik Universität Heidelberg. May 2014. URL: http://spadic.uni-hd.de/spadic10/data/spadic10spec.pdf.

[SS11] C. Sturm and H. Stöcker. "The facility for antiproton and ion research FAIR." In: *Physics of Particles and Nuclei Letters* 8.8 (Dec. 2011), pp. 865–868. DOI: 10.1134/s1547477111080140.

[TDR18] The CBM Collaboration. *The Transition Radiation Detector of the CBM Experiment at FAIR: Technical Design Report for the CBM Transition Radiation Detector (TRD)*. Tech. rep. Facility for Antiproton and Ion Research in Europe GmbH Darmstadt, Oct. 2018. DOI: http://dx.doi.org/10.15120/GSI-2018-01091.

Plagiatserklärung

Hiermit versichere ich, dass die vorliegende Arbeit *First mTRD Performance Studies in the mCBM 2020 Campaign* selbstständig verfasst worden ist, dass keine anderen Quellen und Hilfsmittel als die angegebenen benutzt worden sind und dass die Stellen der Arbeit, die anderen Werken – auch elektronischen Medien – dem Wortlaut oder Sinn nach entnommen wurden, auf jeden Fall unter Angabe der Quelle als Entlehnung kenntlich gemacht worden sind.

Ich erkläre mich mit einem Abgleich der Arbeit mit anderen Texten zwecks Auffindung von Übereinstimmungen sowie mit einer zu diesem Zweck vorzunehmenden Speicherung der Arbeit in eine Datenbank einverstanden.